

Nonlinear waves in lattices and metamaterials

by

Henry Duran

B.S. in Mathematics and Physics, University of Minnesota - Twin Cities, 2015

Submitted to the Graduate Faculty of
the Dietrich School of Arts and Sciences in partial fulfillment
of the requirements for the degree of
Doctor of Philosophy

University of Pittsburgh

2022

UNIVERSITY OF PITTSBURGH
DIETRICH SCHOOL OF ARTS AND SCIENCES

This dissertation was presented

by

Henry Duran

It was defended on

June 23, 2022

and approved by

Professor Anna Vainchtein, Department of Mathematics, University of Pittsburgh

Professor Dehua Wang, Department of Mathematics, University of Pittsburgh

Professor Ming Chen, Department of Mathematics, University of Pittsburgh

Professor Panayotis G. Kevrekidis, Department of Mathematics and Statistics, University of

Massachusetts at Amherst

Copyright © by Henry Duran
2022

Nonlinear waves in lattices and metamaterials

Henry Duran, PhD

University of Pittsburgh, 2022

The combination of dispersion and nonlinearity often leads to the formation of nonlinear waves with complex bifurcation structure. This thesis focuses on the existence, stability and dynamic evolution of several different types of these waveforms in spatially discrete nonlinear systems.

In the first part of the thesis, we consider traveling solitary waves in a lattice where the competition between nonlinear short-range interactions and all-to-all harmonic long-range interactions yields two parameter regimes. We compute exact traveling waves for both cases and investigate their stability. Perturbing the unstable solution along the corresponding eigenvector, we identify two scenarios of the dynamics of their transition to stable branches. In the first case, the perturbed wave slows down after expelling a dispersive shock wave, and in the second case, it speeds up and is accompanied by the formation of a slower small-amplitude traveling solitary wave.

In the second part, we explore the existence, stability and dynamical properties of moving discrete breathers in a nonlinear lattice. We propose a numerical procedure that allows us to systematically construct breathers traveling more than one lattice site per period. We explore their stability spectrum and connect it to the energy-frequency bifurcation diagrams. We illustrate in this context examples of the energy being a multivalued function of the frequency. Finally, we probe the moving breather dynamics and observe how the associated instabilities change their speed, typically slowing them down over long-time simulations.

In the third part, we turn to stationary discrete breathers. We seek such solutions in a discrete model that describes an engineered structure consisting of a chain of pairs of rigid cross-like units connected by flexible hinges. Upon analyzing the linear band structure of the model, we identify parameter regimes in which this system may possess discrete breather solutions. We then compute numerically exact solutions and investigate their properties and stability. Our findings demonstrate that the system exhibits a plethora of discrete breathers, with multiple branches of solutions that feature period-doubling, symmetry-breaking and other types of bifurcations. The relevant stability analysis is corroborated by direct numerical computations examining the dynamical properties of the system.

Keywords: solitary traveling waves, discrete breathers, Fermi-Pasta-Ulam lattice, long-range interactions, metamaterials, Floquet spectrum, instability, nonlinear resonances, bifurcations.

Table of Contents

Preface	xix
1.0 Introduction	1
1.1 Stability and dynamics of lattice solitary traveling waves	1
1.2 Moving discrete breathers	3
1.3 Discrete breathers in a mechanical metamaterial	5
2.0 Unstable dynamics of solitary traveling waves in a lattice with long-range interactions	9
2.1 Problem formulation and prior results	9
2.2 Numerical methods	13
2.3 Unstable dynamics in the N -region	15
2.4 Results for the Z -region	20
2.5 Concluding remarks	24
3.0 Moving discrete breathers in a β-FPU lattice	25
3.1 Problem formulation	25
3.2 Numerical Methods	27
3.3 Frequency dependence, resonances and stability	30
3.4 Dynamical consequences of exponential instabilities	36
3.5 Conclusions	39
4.0 Discrete breathers in a mechanical metamaterial	41
4.1 Problem formulation	41
4.2 Dispersion Relation	43
4.3 Period-doubling bifurcation	48
4.4 Snake-like solution branches	56
4.4.1 Branches associated with the $k = \pi$ mode	57
4.4.2 Zero-mode optical and π -mode acoustic branches	65
4.5 Concluding remarks	68
Appendix A.	71
A.1 Weighted spaces, skew symmetry and essential spectrum	71

A.2 Multiplicity of the zero eigenvalue	76
A.3 Numerical implementations and Hamiltonian symmetry	78
Appendix B.	80
B.1 Additional traveling breather solutions	80
B.2 Effect of the lattice size	83
Bibliography	87

List of Tables

1	Comparison of numerical and approximate resonance values ω_m for $V_1 = 1/3$ and $N = 60$. The approximate values were computed using (29). The numerical values were computed by using the wing energy plots, such as Fig. 15(b), and estimating the frequency at the center of the gap that separates branches corresponding to each resonance.	34
2	Comparison of approximate and numerical resonance values ω_m for $V_1 = 2/5$ and $N = 60$. The approximate values were computed using (29).	36

List of Figures

1	Top panel: discrete chain of cross-shaped rigid units. Bottom panel: kinematic variables and parameters. Adapted from Supplementary Figure 6 in [96].	7
2	The M , Z and N -regions in the (α, J) plane together with the boundary curves $J_1(\alpha)$ (right) and $J_2(\alpha)$ (left) defined in (10). Circles mark the parameter values for the examples discussed in Sec. 2.3 and Sec. 2.4.	12
3	(a) Energy H and (b) maximal real Floquet multiplier μ as functions of velocity c of the STWs at $(\alpha, J) = (0.165, 0.1)$. Unstable waves where $\mu > 1$ correspond to the decreasing dashed portion of the energy curve ($H'(c) < 0$). Points A , B , C , and D correspond to the velocities of the tested unstable waves, and points A_1 , A_2 , B_1 , B_2 , C_1 , C_2 , D_1 , and D_2 mark the corresponding final velocities of the stable waves that the perturbed unstable STWs have evolved into, depending on the sign of the perturbation. Inset in (b) shows the enlarged view around the maximum.	16
4	Eigenmode of an unstable STW with $c = 3.458$, $(\alpha, J) = (0.165, 0.1)$ corresponding to the Floquet multiplier $\mu = 1.0048$ that leads to the speeding up of the perturbed wave. Here y_n corresponds to strain and z_n to its time derivative. Reversing the sign of the perturbation results in slowing down of the perturbed wave. The red curve connecting the discrete points is included as a guide to the eye.	17
5	(a) Time evolution of the velocity of wave resulting from initial perturbation with $\epsilon = -0.25$ of the unstable STW with velocity 3.459 (point B in Fig. 3) at $(\alpha, J) = (0.165, 0.1)$. The velocity evolution is non-monotone: it initially decreases, then increases over a small time interval and then decreases again to the value 3.3932 (point B_1 in Fig. 3) towards the end of the simulation. (b) Time evolution of the energy of the STW. (c) Time evolution of the momentum of the STW. The red dashed lines show the evolution with small-amplitude random noise added to the initial perturbation, while the solid blue lines correspond to the simulations without the additional noise.	18

- 6 (a) Space-time and (b) time evolution of $w_n(t)$ at fixed n during the transition from B to B_1 shown in Fig. 5. A primarily tensile dispersive shock wave is expelled by the main waveform as it slows down. Here $n_0 = 701$, and the selected values of n are spaced 300 units apart in (b). In (a) and other space-time plots shown below, we plot $\sinh^{-1}(70w_n)$ instead of w_n so that the structure of the expelled secondary waves is more pronounced. 18
- 7 (a) Time evolution of the velocity of wave resulting from initial perturbation with $\epsilon = 0.25$ of the unstable STW with velocity 3.458 (point A in Fig. 3) at $(\alpha, J) = (0.165, 0.1)$. The velocity increases, approaching the value 3.6462 (point A_2 in Fig. 3) towards the end of the simulation. (b) Time evolution of the energy of the STW. (c) Time evolution of the momentum of the STW. The red dashed lines show the evolution with small-amplitude random noise added to the initial perturbation, while the solid blue lines correspond to the simulations without the additional noise. 19
- 8 (a) Space-time and (b) time evolution of $w_n(t)$ at fixed n during the transition from A to A_2 shown in Fig. 7. A compressive small-amplitude STW, trailed by small amplitude oscillations, forms behind the main nonlinear waveform and eventually separates from it as the main wave increases its velocity. Here $n_0 = 701$, and the selected values of n are spaced 300 units apart in (b). 19
- 9 (a) Energy H versus velocity c of STWs at $(\alpha, J) = (0.1, 0.012)$. Points A and B correspond to the energy and velocity of the tested waves, and points A_1 , A_2 , B_1 , and B_2 mark the corresponding final velocities and energies of the stable waves the perturbed unstable STWs have evolved into. The dashed line corresponds to the portion of the curve where $H'(s) < 0$, and insets zoom in around the points where $H'(s) = 0$. (b) Maximal real Floquet multiplier μ as a function of the parameter s . The solid vertical lines indicate the values of s where $H'(s) = 0$. The dashed horizontal line marks the value $\mu = 1.0042$. In both figures, point A corresponds to the STW with velocity 2.0984 and point B corresponds to the STW with velocity 2.0785. 20
- 10 Squared rescaled near-zero eigenvalues $\nu(s) = \lambda(s)/c(s) = \ln(\mu(s))$ near (a) the maximum and (b) the minimum of $H(s)$ at $(\alpha, J) = (0.1, 0.012)$. The straight lines show the best linear fit in each case. The black horizontal lines mark $\nu = 0$ 21

11	(a) Time evolution of the velocity of wave resulting from initial perturbation with $\epsilon = -0.25$ of the unstable STW with velocity 2.0785 (point B in Fig. 9(a)) at $(\alpha, J) = (0.1, 0.012)$. The final velocity is 2.0439 (point B_1 in Fig. 9(a)). (b) Time evolution of the energy of the STW.	22
12	(a) Space-time and (b) time evolution of $w_n(t)$ at fixed n during the transition from B to B_1 shown in Fig. 11. A dispersive shock wave is expelled by the main waveform as it slows down. Here $n_0 = 901$, and the selected values of n are spaced 1000 units apart in (b).	23
13	An enlarged view of the space-time plot Fig. 12(a). The arrows mark the points corresponding to the minimal and maximal values of the wave's velocity in Fig. 11(a). . . .	23
14	(a) Verification of the relation described in (17) for the moving breather with period-wise velocity $V_1 = 14/23$ and internal frequency $\omega = 2.5$. The blue circles are the displacements at time $t = 23T$, while the solid red line is the displacement at time $t = 0$ shifted to the right by 14 lattice sites. The inset shows the absolute difference between the two sets of displacements. (b) Space-time evolution of the site energy $e_n(t)$. (c) Floquet multipliers μ associated with the linearization around the solution of panels (a)-(b). The absence of multipliers lying off of the unit circle suggests the spectral stability of the relevant waveform.	29
15	(a) Energy H , (b) the normalized average site energy e_{wing}/e_{max} of the wings and (c) the maximum moduli of the Floquet multipliers μ along different branches as functions of ω at $V_1 = 1/3$ and $N = 60$ near the resonance $\omega = 2.237$. The Floquet multiplier with the maximum modulus has nonzero real and imaginary parts along dashed portions the curve and is real along the solid one. Insets illustrate that this transition occurs due to the collision of a pair of real Floquet multipliers and subsequent emergence of a quadruplet of complex-valued multipliers symmetric about the unit circle (only the pair of such multipliers outside the unit circle is shown in the second inset). Different colors correspond to different branches in (a). The numbers in (b) are the values of m for the corresponding resonances (see the text for detail).	31
16	The top panel shows a zoomed-in view of the resonance near $\omega = 2.126$. The black vertical line marks $\omega = 2.126$ at which three different moving breathers coexist. These breathers are shown in the three bottom panels, where colors match the respective branches depicted in the top panel. Here $V_1 = 1/3$ and $N = 60$	32

17	(a) Energy H , (b) the normalized average site energy e_{wing}/e_{max} of the wings and (c) maximum moduli of the Floquet multipliers μ along different branches as functions of ω at $V_1 = 2/5$ and $N = 60$ near the resonance $\omega = 2.337$. The Floquet multiplier with the maximum modulus has nonzero real and imaginary parts along the dashed portions of the curve and is real along the solid one. Insets illustrate that transitions between these regimes occur due to the collisions of pairs of real and complex Floquet multipliers. Different colors correspond to different branches in (a). The numbers in (b) are the values of m for the corresponding resonances (see the text for details).	35
18	(a) Displacement profiles q_n of the unperturbed moving breather with $V_1 = 1/3$, $\omega = 2.424$, and $N = 60$. (b) Floquet multipliers μ . The largest real multiplier is $\mu = 1.0989$	37
19	Time evolution of the translational velocity V_2 for the moving breather with largest real Floquet multiplier $\mu = 1.0989$ at (a) $\epsilon = -0.01$; (b) $\epsilon = 0.01$. Here $V_1 = 1/3$, $\omega = 2.424$ and $N = 60$. After an initial transient resulting from the instability manifestation, the breather can be seen to incur a very slow velocity decrease over the long time evolution.	38
20	(a) Space-time evolution of the site energy $e_n(t)$ and (b) time evolution of the velocity V_2 near the start of the simulation with $\epsilon = 0.01$. The arrows pointing left and right in (a) correspond to the arrows pointing up and down, respectively, in (b). Here $V_1 = 1/3$, $\omega = 2.424$ and $N = 60$	38
21	Optical branch of the dispersion relation at different values of ϕ_0 . For each panel the corresponding value of ϕ_0 is given; see also the discussion in the text. Here $\alpha = 1.8$, $K_s = 0.02$, $K_\theta = 1.5 \times 10^{-4}$	45
22	Optical (blue) and acoustic (orange) branches for (a) $\phi_0 = 26\pi/180 \approx 0.4538$, $\alpha = 1.8$, $K_s = 0.02$, $K_\theta = 1.5 \times 10^{-4}$; (b) $\phi_0 = 8\pi/180 \approx 0.1396$, $\alpha = 5$, $K_s = 0.02$, $K_\theta = 0.01$; (c) $\phi_0 = 10\pi/180 \approx 0.1745$, $\alpha = 5$, $K_s = 0.02$, $K_\theta = 0.01$. The horizontal lines indicate the maximum $\omega_-(\pi)$ of the acoustic branch and $\omega_+(k_{max})/2$, half of the maximum of the optical branch. When the optical branch is above $\omega_-(\pi)$, (41) holds, and when it is above $\omega_+(k_{max})/2$, (42) holds.	46
23	(a) G defined in (41) as a function of ϕ_0 . The horizontal line is $G = 0$, and the two vertical lines indicate $\phi_0 = \phi_0^* = 0.1400$ and $\phi_0 = \phi_0'' = 0.5888$. (b) S defined in (42) as a function of ϕ_0 . The horizontal line is $S = 0$ and the two vertical lines indicate $\phi_0 = \phi_0^{**} = 0.2811$ and $\phi_0 = \phi_0'' = 0.5888$. Here $\alpha = 1.8$, $K_s = 0.02$, $K_\theta = 1.5 \times 10^{-4}$	47

- 24 (a) G defined in (41) as a function of ϕ_0 . The horizontal line is $G = 0$ and the two vertical lines indicate $\phi_0 = \phi_0^* = 0.0992$ and $\phi_0 = \phi_0'' = 0.1588$. (b) S defined in (42) as a function of ϕ_0 . The horizontal line is $S = 0$ and the two vertical lines indicate $\phi_0 = \phi_0'' = 0.1588$ and $\phi_0 = \phi_0^{***} = 0.3906$. Here $\alpha = 5$, $K_s = 0.02$, $K_\theta = 0.01$ 48
- 25 (a) Energy H as a function of frequency ω . The two insets show the strain (33) and angle variables at the points A , B , and C along the solution curve. (b) $H(\omega)$ for the single-period (blue curve) and double-period (red and green curves) solution branches at twice their frequency. The bifurcation points are marked by d and e . The two insets show the strain and angle variables at the points D and E along the double-period solution curves. (c) Maximum modulus $|\mu|$ of Floquet multipliers versus frequency ω along the single-period (blue) and double-period (red and green) solution branches. The insets show the corresponding Floquet multipliers near the unit circle. While the double-period solution along the red curve coincides with the single period solution (blue curve) at the bifurcation point e , the Floquet multipliers for the double-period solution are squares of those for the single-period one, resulting in the gap between the blue and red curves. (d) Upper panel: largest modulus $|\mu|$ of the real Floquet multipliers as a function of frequency ω along the blue single-period and green double-period solution curves near the bifurcation point d . Lower panel: second largest modulus $|\mu|$ of the real Floquet multipliers as a function of ω along the blue single-period and red double-period solution curves near the bifurcation point e . Note that these real Floquet multipliers are negative for the blue curve and positive for the red and green curves. (e) Enlarged view of $H(\omega)$ along the green double-period solution curve. The dashed vertical lines indicate the local minimum (left) and maximum (right). The points x_1, \dots, x_9 correspond to the Floquet multiplier panels shown in (f). The inset shows an enlarged view around the cluster of points. (f) The Floquet multipliers near $\mu = 1$ for the points marked in the panel (e). The arrows indicate the motion of the Floquet multipliers. Here and in the remainder of this section we have $\alpha = 1.8$, $K_s = 0.02$, $K_\theta = 1.5 \times 10^{-4}$, $N = 200$, and $\phi_0 = 26\pi/180$. . 51

26	Panels (a) and (b) show Floquet multipliers μ at the start ($\omega = 1.57$, panel (a)) and the end ($\omega = 0.9972$, panel (b)) of the continuation. Panel (c) shows an enlarged view of Fig. 25(b). The vertical line indicates the frequency $\omega = 1.229$, at which the top optical and bottom acoustic arcs shown in Fig. 27 below first intersect (see the text for details). Here $ \mu > 1$ corresponds to oscillatory instabilities, as shown in the insets, where the red curve is part of the unit circle.	53
27	Numerically computed Floquet multipliers (dark blue crosses) and arcs of Floquet multipliers (47) corresponding to top optical ($\omega_+(k)$, red arc) and bottom acoustic ($-\omega_-(k)$, light blue arc) dispersion bands at (a) $\omega = 1.57$; (b) $\omega = 1.4$; (c) $\omega = 1.201$	54
28	The angle and strain variables near the right end of the chain for the phantom breather with frequency $\omega = 0.9972$ (solid red) and the regular (localized) discrete breather with frequency $\omega = 1.02$ (dashed blue).	55
29	The amplitude spectrum $P(\omega)$ obtained using the FFT for different values of the prescribed breather frequency $\tilde{\omega}$: (a) $\tilde{\omega} = 1.1$; (b) $\tilde{\omega} = 1.02$. The left and right shaded stripes in each of the bottom panels indicate the acoustic and optical dispersion bands, respectively. The dashed vertical lines indicate $\tilde{\omega}$ and $2\tilde{\omega}$ in both panels and $\tilde{\omega}/2$ in panel (b). It is clear that the frequencies associated with the breather do not resonate with the linear spectral bands in the cases shown.	56
30	Initial guess for (a) displacement $u_n = \varepsilon_u \tanh(\delta(n - N/2))$; (b) angle θ_n obtained from the π -mode eigenvector (see the text for details). Here $\varepsilon_u = 0.05$ and $\delta = 0.15$	57
31	Energy H of the computed DB solutions as a function frequency ω . Blue, red and green curves are branches of solutions that have even symmetry, while the asymmetric solution curves are shown in black. Thin dashed portions of the curves indicate the presence of the real multiplier pairs $(1/\mu, \mu)$ with $\mu > 1$. Along the thick dashed segments there are also real multipliers $(1/\mu, \mu)$ with $\mu < -1$. Parts of the curve where there are only oscillatory instabilities with the maximum modulus of the Floquet multipliers exceeding 1.009 are indicated by thin dotted segments. Solutions that also have real multiplier pairs $(1/\mu, \mu)$ with $\mu < -1$ are along the thick dotted parts. Solid curves indicate the portions where there are no exponential instabilities, and the maximum modulus of the Floquet multipliers is below 1.009. Here and in the remainder of this subsection we have $\alpha = 5$, $K_s = 0.02$, $K_\theta = 0.01$, $N = 200$, and $\phi_0 = 10\pi/180$	59

- 32 (a) Energy H as a function of frequency ω along the blue symmetric solution branch. The insets provide a enlarged view of the turning points. (b) Strain and angle variables for the solutions at the points A , B , and C in (a). (c) $H(\omega)$ along the red symmetric solution branch. The inset showing Floquet multipliers illustrates the emergence of an exponential instability. A pair of complex Floquet multipliers (blue crosses) associated with a solution before the transition collides to form two positive real multipliers (red crosses) associated with the solution after the collision. The corresponding symmetric multipliers inside the unit circle are not shown. (d) Strain and angle variables for the solutions at the points A , B , and C in (c). (e) Left panel: the unstable asymmetric branch connecting the red and blue symmetric branches (left panel). Right panel: maximum real Floquet multiplier as a function of energy for the three branches. All solution profiles are shown at the time instances of maximal amplitude. 60
- 33 (a) Energy H as a function of frequency ω along the blue and green symmetric solution branches and bifurcating branches of asymmetric solutions, with a , b , c , and d marking the bifurcation points. The insets show the solutions of the asymmetric and symmetric branches at the points A , B , and C . (b) The stability exchange between the symmetric (blue) and the asymmetric (black) branch. Both the associated portion of the bifurcation diagram and the dominant multiplier of each branch associated with the instability growth rate are shown. (c) Energy H versus frequency ω for the green symmetric solution branch with d and e marking the bifurcation points (see Fig. 34 for the asymmetric branch bifurcating from e). (d) The enlarged view of the region inside the rectangle in (c). The insets show the transition from exponential to oscillatory instabilities and vice versa that take place over the green symmetric curve. The red and blue crosses indicate Floquet multipliers μ outside the unit circle that correspond to solutions before and after the transition point, respectively. 62

- 34 (a) Energy H as a function of frequency ω along the green symmetric solution branch and a branch of asymmetric solutions (different from the ones discussed earlier) bifurcating at the point e . The insets include profiles of the angle variable at the points A , B , and C . (b) The insets pointing toward points D and E show the emergence of a third pair of real Floquet multipliers. In both insets, an additional pair of real multipliers is present but not shown due to its larger magnitude. The inset pointing toward the point F illustrates the collision of two pairs of real multipliers to form two complex pairs. The red and blue crosses indicate Floquet multipliers outside the unit circle that correspond to solutions before and after the transition point, respectively. 64
- 35 (a) Energy H as a function of frequency ω along an asymmetric solution branch that exists near the $k = \pi$ edge of the optical branch. The insets include profiles of the angle variable at the points A , B , C , and D . (b) The same branch, with the inset showing the collision of two pairs of complex Floquet multipliers to form two real pairs. Blue and red crosses show the pairs outside the unit circle that correspond to solutions before and after the transition, respectively. 65
- 36 (a) Energy H as a function of frequency ω along the red and blue symmetric solution curves. The points A - L indicate the perturbed unstable solutions, while the points A^* - L^* mark the corresponding final states. The inset zooms in on the region including the end points. (b) Space-time plot of the displacement $u_n(t)$ for the solution corresponding to point E . Here $\epsilon = 10^{-5}$ is the strength of the perturbation, and $\mu = 1.3596$ is the largest real Floquet multiplier. (c) Space-time plot of the angle $\theta_n(t)$. (d) Enlarged view of (c). Both (c) and (d) are shown in a logarithmic plot to facilitate the visualization of the small scales involving dispersive wave radiation as a result of the instability. 66

- 37 Energy H of the computed DB solutions as a function frequency ω . Blue and red curves bifurcate from the optical band at $k = 0$, while the green curve is associated with the acoustic π -mode. All of the branches shown contain solutions with even symmetry. Thin dashed portions of the curves indicate the presence of the real multiplier pairs $(1/\mu, \mu)$ with $\mu > 1$. Along the thick dashed segments there are also real multipliers $(1/\mu, \mu)$ with $\mu < -1$. Parts of the curve where there are only oscillatory instabilities with the maximum modulus of the Floquet multipliers exceeding 1.009 are indicated by thin dotted segments. Solutions that also have real multiplier pairs $(1/\mu, \mu)$ with $\mu < -1$ are along the thick dotted parts. Solid curves indicate the portions where there are no exponential instabilities, and the maximum modulus of the Floquet multipliers is below 1.009. Here and in the remainder of this subsection we have $\alpha = 5$, $K_s = 0.02$, $K_\theta = 0.01$, $N = 200$, and $\phi_0 = 8\pi/180$ 67
- 38 (a) Energy H as a function of frequency ω along the blue symmetric solution branch. (b) Strain and angle variables for the solutions at the points A , B , and C in panel (a). (c) $H(\omega)$ along the red symmetric solution branch. The inset showing Floquet multipliers illustrates the emergence of an exponential instability. A pair of complex Floquet multipliers (red crosses) associated with a solution before the transition collides to form two positive real multipliers (blue crosses) associated with the solution after the collision. The corresponding symmetric multipliers inside the unit circle are not shown. (d) Strain and angle variables for the solutions at the points A , B , and C in panel (c). (e) $H(\omega)$ along the green symmetric solution branch. The inset shows the enlarged view near the end of the computed branch. (f) Strain and angle variables for the solutions at the points A , B , and C in panel (e). All solution profiles are shown at the time instances of maximal amplitude. 70
- 39 Coexisting solutions. Panels (a), (d) and (g) show the energy H versus frequency ω along two coexisting solution branches, red and blue, near the resonance at $\omega = 2.352$. The horizontal black line marks the energy of the two solutions whose displacements q_n are compared in panels (b), (e) and (h), respectively. Panels (c), (f) and (i) show the corresponding Floquet multipliers, with insets zooming in on the multipliers near $\mu = 1$. In each case, a pair of Floquet multipliers is separating from $\mu = 1$. Here $V_1 = 1/3$ and $N = 60$ 81

40	(a) Energy H versus frequency ω and (b) the maximum real Floquet multipliers μ along the two solutions near the resonance at $\omega = 2.352$. The colors correspond to those used in Fig. 39. Here $V_1 = 1/3$ and $N = 60$. In the left panel the blue and red branches cannot be distinguished over the scale of the figure (see also the magnified pictures in the left panels of Fig. 39).	82
41	Time evolution of the absolute difference between the computed speed c and the initial initial translational velocity $V_2 = 1/(3T)$ for the moving breather with the largest real Floquet multiplier $\mu = 1.0023$ perturbed along the corresponding unstable eigenmode. Panels (a) and (c) show the early and late stages of the evolution, while panel(b) depicts over the entire time span. The maximum modulus of the Floquet multipliers is $ \mu = 1.0104$. In panels (a) and (c), the red lines correspond to the best linear fit measuring the growth rate of the wave. The line in panel (a) measures the initial growth due to the exponential instability, and the second line measures the growth due to the oscillatory instability. In panel (b), the darker region corresponds to the emergence of the oscillatory instability as the main factor in the growth of the perturbed moving breather. Here $N = 60$, $\omega = 2.355$, $V_1 = 1/3$, and the strength of the perturbation is $\epsilon = 10^{-7}$	82
42	Profiles of (a) displacement q_n and (b) energy density e_n of a moving breather with $N = 60$ (solid blue) and $N = 180$ (dash-dotted red) of the central 60 sites. Here $\omega = 2.19$ and $V_1 = 1/2$. The inset in each panel shows a segment of the wings of the two solutions. . .	85
43	Profiles of (a) displacement q_n and (b) energy density e_n of a moving breather with lattice size $N = 60$ (solid blue) and $N = 180$ (dash-dotted red) of the central 60 sites. Here $\omega = 2.37$ and $V_1 = 1/2$. The inset in each panel shows a segment of the wings of the two solutions.	85
44	Profiles of (a) displacement q_n and (b) energy density e_n of a moving breather with $N = 60$ (solid blue) and $N = 180$ (dash-dotted red) of the central 60 sites. Here $\omega = 2.49$ and $V_1 = 1/2$. The inset in each panel shows a zoomed in view of the wings of the two solutions.	86

Preface

It is a strange experience to finally be writing this part after spending what felt like so much of my life on obtaining my Ph.D. degree, but so it goes. I want to give credit to the various people in my life who helped me to reach this moment.

I would first like to thank my family for supporting me in my moments of doubt and encouraging me to continue. It certainly has not always been a smooth ride, but knowing that I have them to rely on helped to make it possible for me.

I would also like to thank the friends that I have made during my time at graduate school. In particular, I am very glad to have met Hiruni Pallage and Astrid Berge. I will always remember the discussions I had with both of you. A special mention as well to Abby Pekoske Fulton, Marcello Codianni and Michael Lindsey for introducing me to how fun board games can be! I was quite pleasantly surprised to find out that they can exist at a level beyond Monopoly.

I wish to also thank my dissertation committee members Dehua Wang and Ming Chen for donating their time and for their helpful comments. I would especially like to thank my research collaborators Panayotis G. Kevrekidis and Jesús Cuevas–Maraver for their guidance and insight on the multiple projects we worked on together. I am going to miss our weekly meetings. I have really come to enjoy doing research with all of you.

Lastly, I of course would like to thank my advisor Anna Vainchtein for all of her help and support over these past few years. I do not think I could have had a better advisor. I really appreciate the level of encouragement that she offered to me during my time here. She has always given me incredibly useful critiques on how to improve, and it has been very helpful for me to have that. As I have come to realize, many things only work through iterations!

1.0 Introduction

Solitary traveling waves and discrete breathers are coherent structures that describe fundamental mechanisms of signal transmission and energy transport in many nonlinear dispersive systems. This dissertation investigates existence, stability and dynamical properties of these waveforms in the context of spatially discrete settings that include lattices and mechanical metamaterials.

This chapter provides background information and an overview of the main results of the thesis, which consists of three parts. In the first part, introduced in Sec. 1.1, we discuss stability and dynamics of solitary traveling waves in a nonlinear lattice with long-range harmonic interactions. Sec. 1.2 introduces the second part, which focuses on moving discrete breathers. The overview of the last part of the thesis, devoted to discrete breathers in a mechanical metamaterial, can be found in Sec. 1.3.

1.1 Stability and dynamics of lattice solitary traveling waves

Since the groundbreaking work [1, 2] on nonlinear Fermi-Pasta-Ulam (FPU) lattices, among the principal objects of investigation have been the solitary traveling waves (STWs), spatially localized nontopological excitations that emerge in such systems and propagate with amplitude-dependent constant velocity, and their connection to soliton solutions of the Korteweg-de Vries (KdV) equation. Consequently, many studies have been devoted to understanding the properties of these waves in discrete systems [3–7], including experimental investigations in electrical networks [8, 9], granular chains [10–12] and mechanical metamaterials [13]. Significant theoretical developments include the discovery of the integrable Toda lattice and the study of its STWs [14], existence proofs for non-integrable systems [15–18] and rigorous investigations of the low-energy [19–25] and high-energy [26–28] limits.

Despite all this progress, stability of lattice STWs remains an issue that is far from being fully understood, with rigorous results only known for some special cases such as the integrable Toda lattice [29, 30], near-integrable sonic limit [19–22] and the hard-sphere high-energy limit [28]. A sufficient condition for change in the spectral stability of a STW was established in [21] for the FPU problem. In the recent work [31, 32] this result was extended to a general class of Hamiltonian

systems and connected to stability criteria in the realm of discrete breathers [33]. This energy-based criterion involves the monotonicity of the Hamiltonian H as a function of the wave's velocity c . The corresponding criterion for breathers, time-periodic localized solutions, concerns the monotonicity of H with respect to the frequency ω of the breather. The intimate connection between the criteria stems from the fact that traveling waves are periodic modulo lattice shifts, resulting in the direct proportionality of ω and c . The relevant stability criterion states that as c is varied, passing through a critical point of $H(c)$ is sufficient (but not necessary) for a change in stability. As shown in [31, 32], a pair of eigenvalues associated with the STW collides at zero at the critical velocity value and reemerges on the real axis when the wave becomes unstable.

The combination of the criterion stated in [31, 32] and the fact that STWs in the FPU problem are stable near the sonic limit, where $H'(c) > 0$ [22], suggests that waves become unstable when $H'(c) < 0$. Interestingly, in most known cases $H(c)$ is a monotonically increasing function and numerical (or, in the case of Toda lattice, analytical [29, 30]) results indicate stability of STWs. Examples of lattices with nonmonotone $H(c)$ include systems with piecewise quadratic interaction potentials [34–37] and their smooth approximations [32]. Another remarkable example was revealed in a series of papers [38–41] that investigated a lattice with nonlinear nearest-neighbor interactions and harmonic Kac-Baker [42, 43] longer-range interactions. Accounting for such effects is important in modeling real physical systems, such as chains of uncharged molecular units with non-negligible dipole-dipole interactions. The exponential decay of the Kac-Baker interactions has been used to obtain closed-form expressions for various thermodynamic quantities in Ising [42, 43], Potts [44] and Klein-Gordon [45] models. In [38–41], the authors showed that depending on the parameters of the long-range interactions and due to an interplay of two different length scales, $H(c)$ can be monotonically increasing, nonmonotone or fold on itself (Z -shaped), becoming multivalued in a certain velocity interval, where three STWs with the same velocity coexist [41]. Numerical simulations in [41] suggest stability of the low-energy and high-energy solutions where $H'(c) > 0$ and instability of the solutions with the intermediate energy values. For the nonmonotone single-valued case, this conjecture is supported by the stability analysis of the associated quasicontinuum model in [40] and linear stability analysis of the discrete system in [31, 32] which reveals the above mentioned instability picture associated with real eigenvalues at the spectral analysis level.

In Chapter 2, which is based on the recent work [46] in collaboration with Panayotis G. Kevrekidis, Haitao Xu and Anna Vainchtein, we revisit this problem and extend the analysis in [31, 32] to the case

when $H(c)$ is no longer single-valued. Specifically, we consider a chain of particles with nearest-neighbor interactions governed by the α -FPU potential $V(w) = w^2/2 - w^3/3$ and harmonic Kac-Baker all-to-all long-range interactions with exponentially decaying moduli $\Lambda(m)$. The dimensionless equations of motion are given by

$$\ddot{w}_n + 2V'(w_n) - V'(w_{n+1}) - V'(w_{n-1}) + \sum_{m=1}^{\infty} \Lambda(m)(2w_n - w_{n+m} - w_{n-m}) = 0,$$

where w_n is the strain variable measuring the relative displacement between $(n+1)$ th and n th particles. We seek STW solutions of this system that propagate with velocity c . Such solutions have the form $w_n(t) = \phi(\xi)$, $\xi = n - ct$, where $\phi(\xi) \rightarrow 0$ as $\xi \rightarrow \pm\infty$. To compute the STWs with velocities above the sound speed c_s of the lattice, we use the collocation method developed in [31, 32] combined with the pseudo-arclength parameter continuation [47]. To study the linear stability of these waveforms, we take advantage of the fact that STWs are periodic modulo a shift by one lattice spacing [21, 31, 32], $w_{n+1}(t+T) = w_n(t)$, with period $T = 1/c$, and employ the Floquet analysis of the problem linearized about a STW solution. Our analysis shows that the change of stability is now associated with the change of the sign of $H'(s)$, where s is the parameter that c and H depend on. More precisely, in the parameter regime where $H(c)$ is Z -shaped the instability is associated with $H'(s) < 0$. In the case of a nonmonotone single-valued $H(c)$ function this reduces to $H'(c) < 0$.

We then proceed to investigate in detail the dynamical consequences of instability in both of these regimes. This is done by perturbing the unstable waves along the eigenmode corresponding to a real Floquet multiplier associated with the instability and tracking the velocity and energy of the evolving wave. Our results show that depending on the sign of perturbation, there are two generic scenarios. In the first case, the wave slows down after expelling a dispersive shock wave. In the second scenario, the wave's velocity increases following the formation and expulsion of a small-amplitude STW. In both cases, the waves stabilize when their velocity reaches a value along the energy-velocity curve where $H'(c) > 0$.

1.2 Moving discrete breathers

Discrete breathers are time-periodic nonlinear modes that arise in lattices due to the interplay of dispersion and nonlinearity [48–50]. The most common form of such excitations are stationary

bright breathers, originally called intrinsic localized modes [51–53] due to their spatial localization. Breathers were found to exist in Hamiltonian and damped-driven lattices and were experimentally observed in a variety of nonlinear discrete systems, including Josephson junction arrays [54, 55], forced-damped arrays of coupled pendula [56], electrical lattices [57–59], micromechanical systems [60–62], the denaturation of the DNA double strand [63] and granular chains [64–67].

In the years since breathers were first discovered [68], there has been much progress in understanding their existence, spectral stability and dynamical properties [5, 49, 50]. For instance, explicit criteria for linear [69] and nonlinear [70] stability of stationary breathers have been put forth. Additionally, it was observed that instability of stationary (in the laboratory frame, i.e., immobile) breathers sets them in motion, and long-lived traveling breathers have been found numerically in various nonlinear lattices [53, 71–74]. Breather mobility is of considerable interest because it is associated with energy transport in the lattice; indeed, such coherent structures have been proposed as a prototypical means for achieving targeted energy transfer in discrete nonlinear systems [75]. An exact moving breather is time-periodic modulo a shift by one or more lattice spaces. The period is an integer multiple of the period of internal vibrations. Such solutions have been constructed using the Newton iterative method, e.g., for Klein-Gordon [74, 76, 77] and β -FPU [74, 78] lattices. For generic interaction potentials that do not possess a certain symmetry [79, 80], moving breathers are no longer spatially localized: instead, they possess oscillatory wings whose amplitude depends on the internal breather frequency and its propagation velocity.

The first detailed analysis of this dependence for a β -FPU lattice was performed in [78]. The authors constructed numerically exact moving breathers for several different rational values of the *period-wise* velocity $V_1 = r/s$, where r is the number of lattice sites the breather travels over s periods of the internal vibration. Performing a continuation in internal frequency ω at fixed V_1 , they investigated how the wing energy (or, equivalently, amplitude) of these breathers depends on their internal frequency. In particular, they studied the mechanism for resonances in the wing amplitude and derived an approximate formula for the resonant frequencies. They also briefly summarized the results of their linear stability investigation (without providing a systematic analysis thereof) for the computed solutions.

Motivated by these earlier studies, we revisit the problem in Chapter 3, based on the recent work [81] in collaboration with Jesús Cuevas–Maraver, Panayotis G. Kevrekidis, and Anna Vainchtein, and conduct a more detailed investigation of the breather existence, stability, dynamics and resonance

features. A scaling argument shows that for a β -FPU problem with the interaction potential $V(w) = w^2/2 + \beta w^4/4$ and $\beta > 0$, it suffices to consider the governing equations

$$\ddot{q}_n = q_{n+1} + q_{n-1} - 2q_n + (q_{n+1} - q_n)^3 - (q_n - q_{n-1})^3,$$

where q_n is the displacement of the n th particle. To compute the moving breathers, we use the Newton iterative method in conjunction with a symplectic and fourth-order Runge-Kutta-Nyström integration algorithm [82] and parameter continuation. As in Chapter 2, linear stability of the obtained solutions is investigated via the computation of Floquet multipliers.

Our analysis extends the results of the earlier work in several ways. Importantly, we consider moving breathers propagating by more than one lattice spacing ($r > 1$) over its period, extending the earlier work that had focused chiefly on the $r = 1$ case. To compute such solutions, we developed a numerical procedure based on a continuation along a sequence of rational values of V_1 . We show that the total breather energy (the Hamiltonian) and the wing energy are in fact *multivalued* functions of the internal frequency ω , so that there are several moving breathers with the same ω and different energies. Moreover, our results reveal the truly nonlinear form of the resonances: a rapid increase in wing energy is followed by a more gradual one. Subsequently, we provide a detailed analysis of the linear stability of the obtained solutions and consider the consequences of the instability associated with real Floquet multipliers $\mu > 1$. In particular, we investigate the dynamics of the breathers perturbed along the corresponding unstable eigenmodes and show that after repeated interactions with the wing oscillations due to the periodic boundary conditions the breather gradually decelerates and eventually becomes nearly stationary, with its velocity oscillating around zero.

1.3 Discrete breathers in a mechanical metamaterial

Mechanical metamaterials are engineered structures [83–88] whose macroscopic properties are primarily controlled by their geometry and may differ considerably from those of their building blocks [89–93]. In recent years, there has been a lot of interest in nonlinear dynamic response of flexible mechanical metamaterials, a new class of engineered materials that exploit large deformation and mechanical instabilities of their components to yield a desired collective response [83, 94]. Examples include metamaterials consisting of rotating rigid elements that are connected by flexible

hinges [95,96], multistable kirigami sheets [97], chains of bistable shells [98] and beams [99], as well as origami-inspired [13,100] and linkage-based [101] deployable structures. These metamaterials can be designed to enable potential applications that include morphing surfaces, soft robotics, reconfigurable devices, mechanical logic and controlled energy absorption [102–108]. Recent studies have demonstrated that metamaterials of this type can be designed to control propagation of a variety of nonlinear waves [94,96,99–101,109,110].

In Chapter 4, based on the work [111] in collaboration with Jesús Cuevas–Maraver, Panayotis G. Kevrekidis, and Anna Vainchtein, we consider the flexible mechanical metamaterial that was recently studied experimentally and theoretically in [94,96,112]. The experimentally realized system, schematically shown in Fig. 1, consists of a chain of pairs of cross-type rigid units made of LEGO bricks and connected by thin flexible polyester or plastic hinges [96,112]. Under certain assumptions, the system can be described by a discrete model that assigns two degrees of freedom to each pair of rigid units: horizontal displacement and rotation. The dimensionless equations of motion for this system are given by

$$\begin{aligned}\ddot{u}_n &= u_{n+1} - 2u_n + u_{n-1} - \frac{\cos(\theta_{n+1} + \phi_0) - \cos(\theta_{n-1} + \phi_0)}{2 \cos(\phi_0)} \\ \frac{1}{\alpha^2} \ddot{\theta}_n &= -K_\theta(\theta_{n+1} + 4\theta_n + \theta_{n-1}) + K_s \cos(\theta_n + \phi_0) \left(\sin(\theta_{n+1} + \phi_0) + \sin(\theta_{n-1} + \phi_0) \right. \\ &\quad \left. - 2 \sin(\theta_n + \phi_0) \right) - \sin(\theta_n + \phi_0) \left(2 \cos(\phi_0)(u_{n+1} - u_{n-1}) + 4 \cos(\phi_0) - \cos(\theta_{n+1} + \phi_0) \right. \\ &\quad \left. - 2 \cos(\theta_n + \phi_0) - \cos(\theta_{n-1} + \phi_0) \right),\end{aligned}$$

where u_n is the displacement component of the n th cross unit, θ_n is the angular component of the n th cross unit, α is a dimensionless inertia parameter, ϕ_0 measures the vertical offset between the neighboring horizontal hinges, and K_s and K_θ are dimensionless parameters modeling the vertical and horizontal hinges. This system, in turn, can be approximated at the continuum level by a Klein-Gordon equation with cubic nonlinearity, a nonlinear wave-bearing system that possesses both soliton and cnoidal wave solutions [94]. In [96], the authors use a combination of experiments, direct numerical simulations of the discrete system and analysis of the continuum model to investigate traveling waves in this system that correspond to elastic vector solitons on the continuum level. They demonstrate that the metamaterial lattice may be designed to exhibit amplitude gaps where soliton propagation is forbidden, which, in turn, enables the design of soliton splitters and diodes. In [112] the anomalous

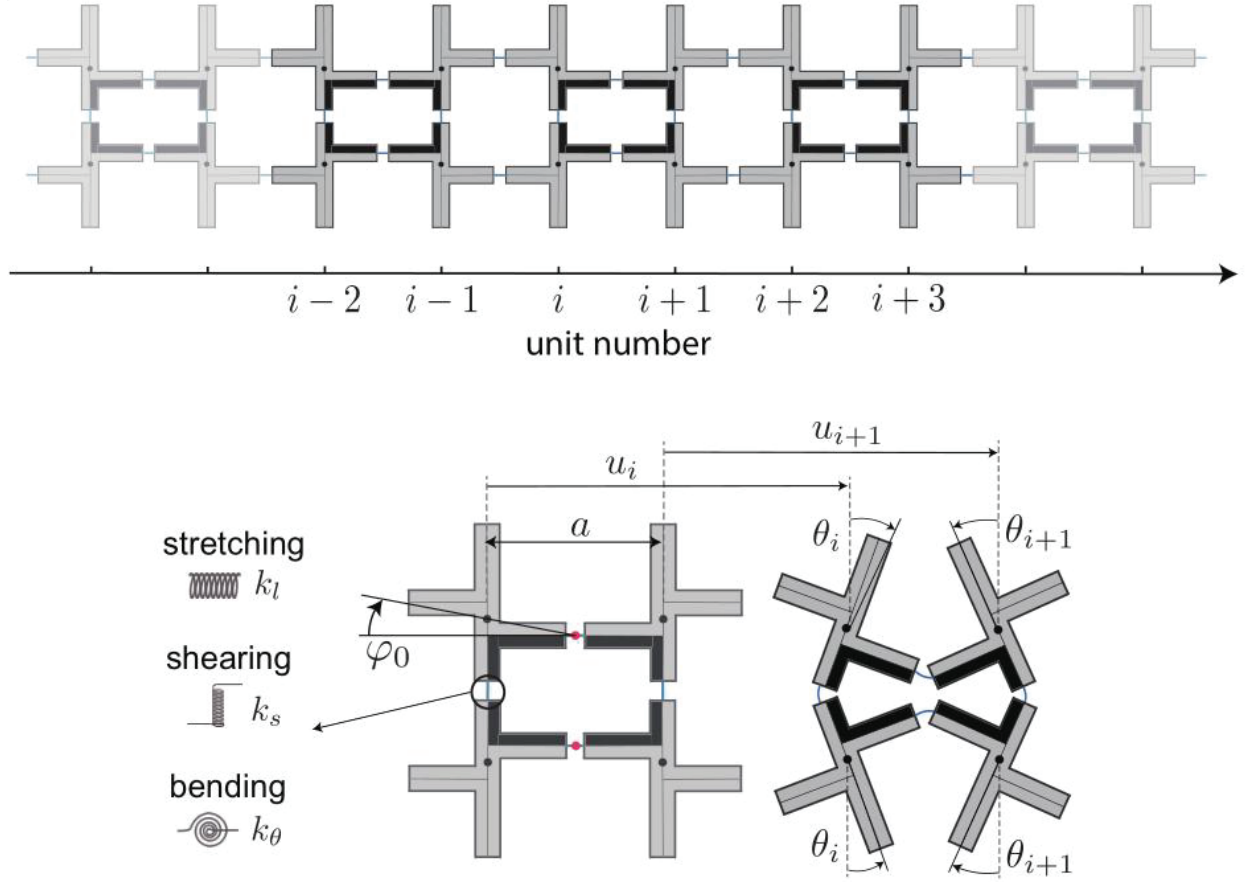


Figure 1: Top panel: discrete chain of cross-shaped rigid units. Bottom panel: kinematic variables and parameters. Adapted from Supplementary Figure 6 in [96].

nature of the soliton collisions in this system is explored. These developments clearly illustrate the promise of this type of nonlinear lattice in regards to the wave dynamics and interactions.

In Chapter 4 we demonstrate that in certain parameter regimes the discrete system derived in [96] also exhibits a plethora of spatially localized, time-periodic patterns in the form of discrete breathers. These structures arise in terms of the angle and strain (relative displacement) variables and appear to be generic in the gaps of the linear excitation spectrum. To construct such solutions for the meta-material system, we start by analyzing the dispersion relation, which features optical and acoustic branches. We show that when the angle ϕ_0 takes values in certain parameter-dependent intervals,

there is a frequency gap between the optical and acoustic branches that enables existence of discrete breathers. We then use the iterations of Newton’s method with a suitable initial guess and (once converged to a member of a solution family) parameter continuation to compute branches of discrete breather solutions that have frequency inside the gap. Stability of the obtained solutions is investigated using the Floquet analysis.

As our first example, we consider the system parameters from [96] and show that in this case a branch of discrete breather solutions bifurcates from the edge of the optical band provided that the offset angle ϕ_0 is above a certain threshold. Floquet analysis reveals that this branch eventually undergoes period-doubling bifurcations, and we compute the corresponding double-period solutions and investigate their stability.

As a second example, we consider a different set of parameters that enables existence of breathers for small offset angles ϕ_0 in a certain interval. Choosing two different values in this interval, we compute branches of solutions bifurcating from the edges of optical and acoustic bands as well as some additional branches that bifurcate from the primary ones. Here, our computation reveals a complex bifurcation diagram in the energy-frequency plane involving branches of symmetric and asymmetric discrete breather solutions and emergence of instability modes associated with real and complex Floquet multipliers. In particular, we find that the onset of real instability can take place via collisions of complex multipliers, as well as symmetry-breaking and period-doubling bifurcations. Another mechanism involves critical points of the breather’s energy as a function of its frequency (effectively, a saddle-center bifurcation), in line with the stability criterion established in [113] for discrete breathers in Fermi-Pasta-Ulam and Klein-Gordon lattices. We investigate the fate of some of the unstable solutions by perturbing them along the corresponding eigenmodes and show that in each case the ensuing dynamic evolution leads to a discrete breather that is effectively stable if one neglects the presence of small-magnitude complex eigenvalues. The computed primary branches have a snake-like form with multiple turning points, and the solution profiles often evolve in a nontrivial way along a branch, e.g., via the emergence of additional peaks or troughs in the strain and angle variables describing a discrete breather with even symmetry. Some features of the obtained bifurcation diagrams are reminiscent of the “snake-and-ladder” patterns observed in other nonlinear systems [114–116], although a detailed exploration of such a phenomenology is outside the scope of this thesis.

2.0 Unstable dynamics of solitary traveling waves in a lattice with long-range interactions

In this chapter, we investigate stability of STW solutions in an α -FPU lattice with harmonic all-to-all long-range interactions of Kac-Baker type and explore the dynamic consequences of the instability. As described in Sec. 1.1, the system features two parameter regimes where the dependence of the energy H of the traveling waves on their velocity c is nonmonotone and multivalued, respectively. We compute STWs for representative parameter values in both regimes and investigate the stability of the obtained solutions using the Floquet analysis. Extending the earlier results in [31,32] to the more general multivalued case, we show that the waves are unstable when $H'(s) < 0$, where s is the parameter along the energy-velocity curve. Perturbing the unstable solutions along the corresponding eigenmodes, we identify two different scenarios of the ensuing dynamic transition to a stable waveform. In the first case, the perturbed wave slows down following an expulsion of a dispersive shock wave. In the second case, the wave speeds up in a process involving the formation of a slower small-amplitude STW.

The chapter is organized as follows. In Sec. 2.1 we formulate the problem and review prior results. In Sec. 2.2 we describe the numerical methods we used. Results for the single-valued nonmonotone $H(c)$ are presented in Sec. 2.3, while Sec. 2.4 is devoted to the multivalued case. Concluding remarks can be found in Sec. 2.5. A more technical stability analysis for multivalued $H(c)$ is presented in Appendix A.

2.1 Problem formulation and prior results

We consider Hamiltonian dynamics of a one-dimensional lattice with nonlinear nearest-neighbor interactions and all-to-all harmonic longer-range interactions, with moduli that decay exponentially with distance. The Hamiltonian of this system is given by

$$H = \sum_{n=-\infty}^{\infty} \left\{ \frac{1}{2} \dot{u}_n^2 + V(u_{n+1} - u_n) + \frac{1}{4} \sum_{m=-\infty}^{\infty} \Lambda(m) (u_n - u_{n+m})^2 \right\}, \quad (1)$$

where $u_n(t)$ denotes the displacement of n th particle at time t , $\dot{u}_n = u'_n(t)$, and $V(w) = w^2/2 - w^3/3$ is the potential governing the nonlinear nearest-neighbor interactions. The last term represents Kac-Baker interactions that have moduli $\Lambda(m) = J(e^\alpha - 1)e^{-\alpha|m|}(1 - \delta_{m,0})$. Here $J > 0$ measures the intensity of the longer-range interactions, and $\alpha > 0$ determines their inverse radius. In terms of the strain (relative displacement) variable $w_n = u_{n+1} - u_n$, the equations of motion are

$$\ddot{w}_n + 2V'(w_n) - V'(w_{n+1}) - V'(w_{n-1}) + \sum_{m=1}^{\infty} \Lambda(m)(2w_n - w_{n+m} - w_{n-m}) = 0. \quad (2)$$

The energy H and the total momentum

$$P = \sum_{n=-\infty}^{\infty} \dot{u}_n \quad (3)$$

of the system are conserved in time.

Previous work [31, 32, 38–41] on this model has focused on *solitary traveling wave* (STW) solutions of (2), which have the form

$$w_n(t) = \phi(\xi), \quad \xi = n - ct, \quad (4)$$

where c is the wave's velocity, and vanish at infinity. These solutions satisfy the advance-delay differential equation

$$c^2 \phi''(\xi) + 2V'(\phi(\xi)) - V'(\phi(\xi+1)) - V'(\phi(\xi-1)) + \sum_{m=1}^{\infty} \Lambda(m)(2\phi(\xi) - \phi(\xi+m) - \phi(\xi-m)) = 0. \quad (5)$$

Numerical computations in [31, 32, 40, 41] suggest the existence of even ($\phi(-\xi) = \phi(\xi)$), compressive ($\phi(\xi) < 0$) solutions of this type with $c > c_s$, where

$$c_s = \sqrt{1 + J \frac{1 + e^{-\alpha}}{(1 - e^{-\alpha})^2}} \quad (6)$$

is the sound speed [41]. Due to the translational invariance of (5), these waves can be shifted arbitrarily along the ξ axis. Note also that the traveling wave solutions (4) are periodic modulo one lattice shift, $w_{n+1}(t + T) = w_n(t)$, with period $T = 1/c$, and thus can be viewed as fixed points of the map

$$\begin{bmatrix} \{w_{n+1}(T)\} \\ \{\dot{w}_{n+1}(T)\} \end{bmatrix} \rightarrow \begin{bmatrix} \{w_n(0)\} \\ \{\dot{w}_n(0)\} \end{bmatrix}. \quad (7)$$

In [40, 41] the lattice equations (2) are approximated by a quasicontinuum model, which yields the traveling wave equation

$$(\partial_\xi^2 - s_+^2)(\partial_\xi^2 - s_-^2)\phi(\xi) = \frac{12}{c^2}(\partial_\xi^2 - \kappa^2)\phi^2(\xi), \quad (8)$$

where $\kappa = 2 \sinh(\alpha/2)$ and

$$s_\pm^2 = \frac{1}{2} \left\{ \kappa^2 + 12 \frac{c^2 - 1}{c^2} \pm \sqrt{\left(\kappa^2 - 12 \frac{c^2 - 1}{c^2} \right)^2 + 48 \kappa^2 \frac{c_s^2 - 1}{c^2}} \right\}. \quad (9)$$

Detailed analysis of the quasicontinuum approximation (8) in [40] (see also [39]) has shown that the interplay of short-range and long-range interactions in the problem gives rise to two competing velocity-dependent length scales $1/s_-$ and $1/s_+$, with s_\pm given in (9). In a certain parameter regime, this scale competition leads to the existence of two branches of STWs, associated with low and high velocities, respectively, and the emergence of crest-like waves when the velocity reaches a critical value.

Numerical computations in [41] of solutions of (5) for the discrete problem further showed that the (α, J) plane can be subdivided into three regions, separated by the curves $J_1(\alpha)$ and $J_2(\alpha)$, where

$$J_1 \approx \begin{cases} 0.23 \frac{\alpha^4}{\alpha_1^2 - \alpha^2}, & \alpha < \alpha_1 \\ \infty, & \alpha \geq \alpha_1, \end{cases} \quad J_2 \approx \begin{cases} \frac{3\alpha^4}{8(\alpha_2^2 - \alpha^2)}, & \alpha < \alpha_2 \\ \infty, & \alpha \geq \alpha_2 \end{cases} \quad (10)$$

and $\alpha_1 = 0.25$, $\alpha_2 = 0.16$. These three regions are shown in Fig. 2. They consist of the *M*-region, where the energy H of the STW monotonically increases with its velocity c , the *N*-region, where the dependence is *nonmonotone*, with $H(c)$ initially increasing, then decreasing for a certain velocity interval and then increasing again, and lastly the *Z*-region, where the function $H(c)$ becomes *multivalued* for some velocities (“*Z*-shaped”). The three different regimes were also captured in [38] using a collective-coordinate approach.

It has been conjectured in [41] that in the *N* and *Z*-regions the low-velocity and high-velocity solutions where $H'(c) > 0$ are stable, while waves along the intermediate branch are unstable. These assertions are supported by the stability analysis in [40] for the quasicontinuum model (8), where the stability threshold is linked to the change of monotonicity of the canonical momentum as a function of the velocity c of the wave, which appears to coincide with the corresponding change in the monotonicity of $H(c)$. In [21] an analogous energy-based criterion, associating the change in the multiplicity of

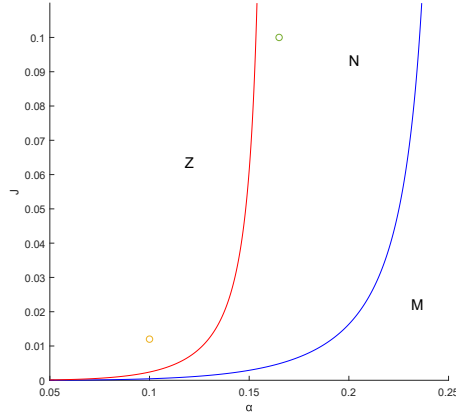


Figure 2: The M , Z and N -regions in the (α, J) plane together with the boundary curves $J_1(\alpha)$ (right) and $J_2(\alpha)$ (left) defined in (10). Circles mark the parameter values for the examples discussed in Sec. 2.3 and Sec. 2.4.

the zero eigenvalue for the linearized problem with the change of sign of $H'(c)$, was proved for the FPU problem without long-range interactions, and in [31, 32] this result was extended to a general class of discrete systems with Hamiltonian H being a single-valued function of c . Moreover, explicit leading-order expressions for the pertinent pair of eigenvalues that meet at the origin at the stability threshold and emerge on the real axis at velocity values corresponding to the unstable waves were obtained in [31, 32]. For the problem at hand, this general result was illustrated in [31, 32] by considering STWs in the N -region and investigating linear stability in two different ways: the spectral analysis of the linear operator associated with the traveling wave equation (5) and the Floquet analysis of the linearization of the map (7). Both approaches corroborated the conjecture in [41] for the N -region. In particular, the waves corresponding to $H'(c) < 0$ are unstable.

In what follows we investigate in detail the consequences of this instability by perturbing the unstable STWs along the corresponding Floquet eigenvectors. To extend these results to the Z -region, where H is a multivalued function of c , we generalize the energy-based stability result in [31, 32] and show that in this case the instability threshold is associated with $H'(s)$ crossing zero, where s is a parameter that both H and c depend on (see Appendix A for the proof that the multiplicity of the zero eigenvalue increases at this threshold). We verify this result and the conjecture in [41] by conducting the Floquet analysis in the Z -region and investigate the corresponding unstable dynamics of STWs associated with $H'(s) < 0$.

2.2 Numerical methods

To compute the STWs in the N -region for given J and α , we employ the collocation method and continuation approach described in [31,32] to generate a one-parameter family of STWs (parametrized by the velocity c) by numerically solving the traveling wave equation (5) for STW solutions starting at an initial velocity just above the sound speed (6) and using the near-sonic solution of the quasicon-
tinuum equation (8) as an initial guess. These waves are computed on the finite interval $(-L/2, L/2]$ with mesh size $\Delta\xi$ at the collocation points $\xi_j = j\Delta\xi$, $j = -N/2 + 1, \dots, N/2$, where N is even and $L = N\Delta\xi$. The fast Fourier transform is used to approximate the second-order derivative term in (5), while the advance and delay terms $\phi(\xi \pm m)$ are evaluated at the corresponding collocation points that are well defined on the chosen mesh. Following [32], we used $L = 800$ and $\Delta\xi = 0.1$ for a typical computation. The resulting nonlinear system is solved numerically for each velocity value using the Newton iteration method.

To compute the STWs in the Z -region, where the energy H is multivalued for some velocities, we combine the numerical procedure described above with the pseudo-arclength continuation method [47] to traverse the turning points in the energy-velocity curve. In this case the traveling wave solution and its velocity c depend on the arclength-like parameter s . In this parameter range, we used $L = 1200$ and $\Delta\xi = 0.1$.

To investigate linear stability of the computed waves, we use Floquet analysis. To this end, we trace the time evolution of a small perturbation $\epsilon y_n(t)$ of the periodic-modulo-shift traveling wave solution $\hat{w}_n(t) = \phi(n - ct)$, where we recall (4). This perturbation is introduced in (2) via $w_n(t) = \hat{w}_n(t) + \epsilon y_n(t)$. The resulting $O(\epsilon)$ equation reads

$$\ddot{y}_n + 2V''(\hat{w}_n)y_n - V''(\hat{w}_{n+1})y_{n+1} - V''(\hat{w}_{n-1})y_{n-1} + \sum_{m=1}^{\infty} \Lambda(m)(2y_n - y_{n+m} - y_{n-m}) = 0. \quad (11)$$

Then, in the framework of Floquet analysis, the stability properties of periodic orbits are resolved by diagonalizing the monodromy matrix \mathcal{F} (representation of the Floquet operator in finite systems), which is defined as

$$\begin{bmatrix} \{y_{n+1}(T)\} \\ \{\dot{y}_{n+1}(T)\} \end{bmatrix} = \mathcal{F} \begin{bmatrix} \{y_n(0)\} \\ \{\dot{y}_n(0)\} \end{bmatrix}, \quad (12)$$

where we recall that $T = 1/c$. We remark that the Floquet operator can be equivalently constructed in terms of the perturbations of strain and momenta variables, which is consistent with the formulation

considered in Appendix A. For symplectic Hamiltonian systems we consider in this thesis, the monodromy eigenvalues μ (also called *Floquet multipliers*) come in either real pairs $(\mu, 1/\mu)$ or complex quartets $(\mu, \bar{\mu}, 1/\mu, 1/\bar{\mu})$, and linear stability of the solutions requires that the Floquet multipliers lie on the unit circle. The presence of a multiplier satisfying $|\mu| > 1$ indicates an instability. When the relevant instability-inducing multiplier is real, we refer to the instability as *exponential*, given the exponential nature of the associated growth. In the case of a complex multiplier quartet, the instability is referred to as *oscillatory*, given that oscillations accompany the exponential growth due to the imaginary part of the associated multipliers.

The Floquet multipliers μ are related to the eigenvalues λ of the operator associated with the linearized problem via $\mu = e^{\lambda/c}$, so that the eigenvalue satisfying $\text{Re}(\lambda) > 0$ corresponds to an instability. As we will show, the instability takes place when $H'(s) < 0$, where s is the parameter along the energy-velocity curve. In the case when $H(c)$ is single-valued, as in the N -region, this simplifies to $H'(c) < 0$ [31, 32]. To find the Floquet multipliers, we construct the monodromy matrix using the numerical solution of (11) with periodic boundary conditions.

To investigate the unstable dynamics, we perturb the wave along the unstable eigenmode, setting the initial conditions $w_n(0) = \phi(n - n_0) + \epsilon y_{n-n_0}$ and $\dot{w}_n(0) = -c\phi'(n - n_0) + \epsilon z_{n-n_0}$ for $|n - n_0| \leq L/2$, and $w_n(0) = \dot{w}_n(0) = 0$ for $1 \leq n < n_0 - L/2$ and $n_0 + L/2 < n \leq N$, with the typical eigenmode profiles for y_n and z_n being depicted in Fig. 4 and ϵ measuring the strength of the applied perturbation. Here we recall that L is the length of the interval on which the traveling wave $\phi(\xi)$ is numerically computed, with (even) L chosen large enough for the wave to decay sufficiently at the end; typically, we set $L = 800$. The computed wave is shifted by n_0 and padded by zeros so that the initial condition defined at $n = 1, \dots, N$ has compact support. Here n_0 and N are chosen so that the ensuing waveforms can propagate for a sufficiently long time without boundary effects. Typically, we set $n_0 = 701$ and $N = 4001$. The equations of motion (2) are then solved numerically with this initial condition and periodic boundary conditions to investigate the fate of the unstable solution.

Of particular interest is the velocity of the ensuing waveform as a function of time. Recall that an STW solution (shifted by n_0) has the form $w_n(t) = \phi(n - n_0 - ct)$, so that if t_1 and t_2 are such that $w_{n_1}(t_1) = w_{n_2}(t_2) = \phi(0)$, we have $c = (n_2 - n_1)/(t_2 - t_1)$. Here t_1 and t_2 correspond to the times when the minimum value of the STW reaches the corresponding particles n_1 and n_2 . In the case of unstable dynamics, the wave is no longer steady, as its velocity and form change with time, but locally these changes are small. With this in mind, we determine the times t_i^* at which the minimum of the

waveform reaches the particle with $n_i = n_0 + i\Delta n$, $i = 1, \dots, K$, and approximate $c(t_i^*)$ by

$$c_i = \frac{\Delta n}{t_{i+1}^* - t_i^*}. \quad (13)$$

Here n_K is the particle number reached by the wave near the end of the simulation. To compute t_i^* more precisely, we use cubic spline interpolation of the numerical data. Experimentally, we found that setting $\Delta n = 5$ was optimal, since this value provided some averaging and yielded final velocities that were the same up to $O(10^{-5})$ as the computations with $\Delta n = 3$ and $\Delta n = 1$.

Other quantities of interest are the (local) energy and momentum of the evolving STW as functions of time. To find these, we consider sample times $\tau_i = i\Delta t$, where $\Delta t = 0.02$. At each time $t = \tau_i$, we determine the particle at which the strain reached its minimal value and compute the energy and momentum of a portion of the chain centered at this particle. The length of the portion, which is the same for each sample time τ_i , is chosen so that the main body of the wave was included in it, which we took to be when the strain was of $O(10^{-4})$ at the ends. Typically, including 125 particles is sufficient. Notice that while the total energy H and momentum P of the lattice remain conserved over the dynamical evolution (up to the relative error of $O(10^{-12})$ in the simulations), the localized energy and momentum portions associated with the wave may vary over time, especially in the scenario of the dynamical evolution of a spectrally unstable wave. In that light, these diagnostics are quite suitable for detecting the potential transformations of STWs as a result of their instability.

2.3 Unstable dynamics in the N -region

We start by investigating the unstable dynamics of STWs in the N -region. While multiple simulations in different regimes have been conducted, we present below only the results for $\alpha = 0.165$, $J = 0.1$ that are representative of the instability patterns observed in this parameter region. The corresponding H and maximal real Floquet multiplier μ as functions of c are shown in Fig. 3.

Due to translational invariance, the system always has a pair of unit Floquet multipliers, which are the maximal real multipliers in the velocity intervals corresponding to increasing energy ($H'(c) > 0$). These velocity intervals apparently correspond to linearly stable STWs, although mild spurious oscillatory instabilities associated with complex Floquet multipliers slightly outside the unit circle may be present in this regime due to numerical artifacts that diminish as L is increased [32]. As the

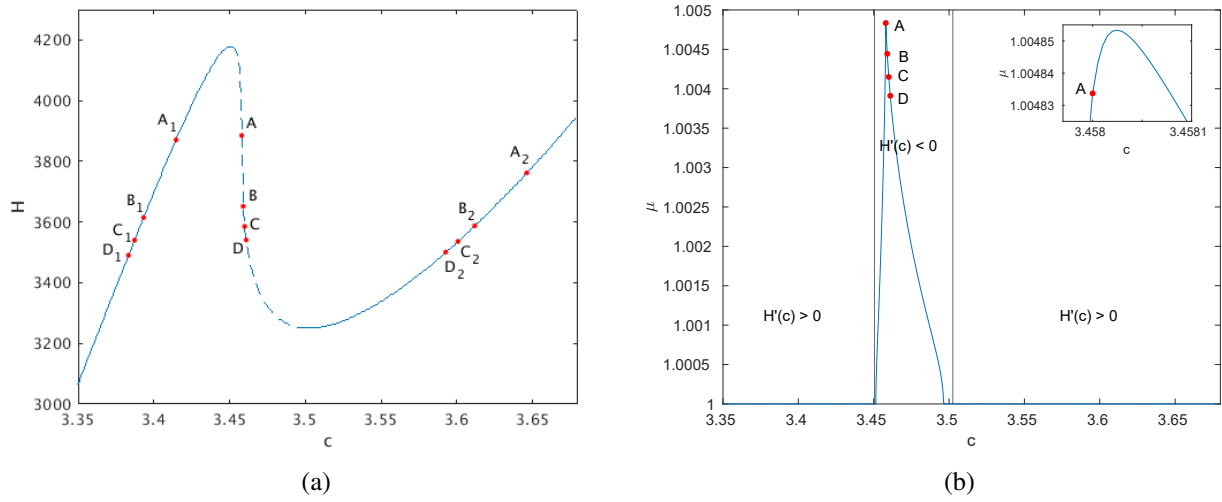


Figure 3: (a) Energy H and (b) maximal real Floquet multiplier μ as functions of velocity c of the STWs at $(\alpha, J) = (0.165, 0.1)$. Unstable waves where $\mu > 1$ correspond to the decreasing dashed portion of the energy curve ($H'(c) < 0$). Points A , B , C , and D correspond to the velocities of the tested unstable waves, and points A_1 , A_2 , B_1 , B_2 , C_1 , C_2 , D_1 , and D_2 mark the corresponding final velocities of the stable waves that the perturbed unstable STWs have evolved into, depending on the sign of the perturbation. Inset in (b) shows the enlarged view around the maximum.

first stability threshold is crossed, a symmetric pair of imaginary eigenvalues λ collides at zero and reemerges on the real axis. Equivalently, a pair of multipliers sliding along the unit circle results in a collision at the point $(1, 0)$ of the unit circle and reemerges on the real axis as a symmetric pair, with maximal real multiplier μ now exceeding unity (and the second multiplier of the pair now being inside the circle with a value of $1/\mu$), so that the corresponding STWs are unstable. The magnitude of μ increases, reaches a maximum value and then decreases again to unity when the second stability threshold is crossed. It should be noted that in the numerical computations $H'(c)$ is slightly below zero at the two stability thresholds. As discussed in [32], this is an artifact of the finite length L of the chain, and $H'(c)$ approaches zero at the threshold when L is increased.

To investigate the consequences of the instability associated with $\mu > 1$, we selected STWs with four different velocities inside the unstable interval and perturbed them along the corresponding eigenmodes, as described in Sec. 2.2. The simulations were run until a stable propagation pattern emerged. In all simulations, the perturbed unstable wave eventually evolves into a stable STW with lower energy and either smaller or higher velocity, as shown in Fig. 3. We found that the size of the perturbation only affected the time it takes for the stable waveform to emerge but not the resulting

wave itself. We also found that adding small random noise (of amplitude 10^{-4}) to the initial perturbation did not significantly affect the results; i.e., for a given unstable initial waveform, the dynamical evolution would apparently select a unique end state on the corresponding stable branches. A typical eigenmode used to initiate the instability is shown in Fig. 4. We note that each normalized eigenmode is determined up to a plus or minus sign, so to change a wave from speeding up to slowing down or vice versa it suffices to reverse the sign of ϵ .

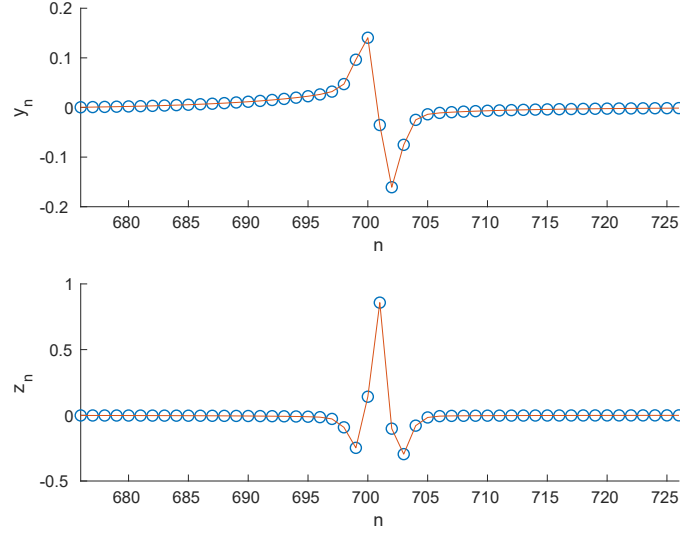


Figure 4: Eigenmode of an unstable STW with $c = 3.458$, $(\alpha, J) = (0.165, 0.1)$ corresponding to the Floquet multiplier $\mu = 1.0048$ that leads to the speeding up of the perturbed wave. Here y_n corresponds to strain and z_n to its time derivative. Reversing the sign of the perturbation results in slowing down of the perturbed wave. The red curve connecting the discrete points is included as a guide to the eye.

A representative example of velocity, energy and momentum evolution in the slow-down case is shown in Fig. 5. We observed that when the velocity of the perturbed unstable wave eventually decreases, the wave expels a small-amplitude dispersive shock wave, as can be seen in Fig. 6. As shown in Fig. 5(a), the velocity evolution in this case is nonmonotone: after initially decreasing, it briefly increases then decreases again to the final value. These velocity oscillations take place right around the time the dispersive wave formation becomes visible in the space-time plot shown in Fig. 6(a). Once this trailing dispersive wave detaches from the primary supersonic STW, the latter settles towards its final velocity. Note that while the energy of the wave decreases during this evolution, its momentum increases, with the total momentum of the system kept constant due to the negative contribution of the dispersive wave.

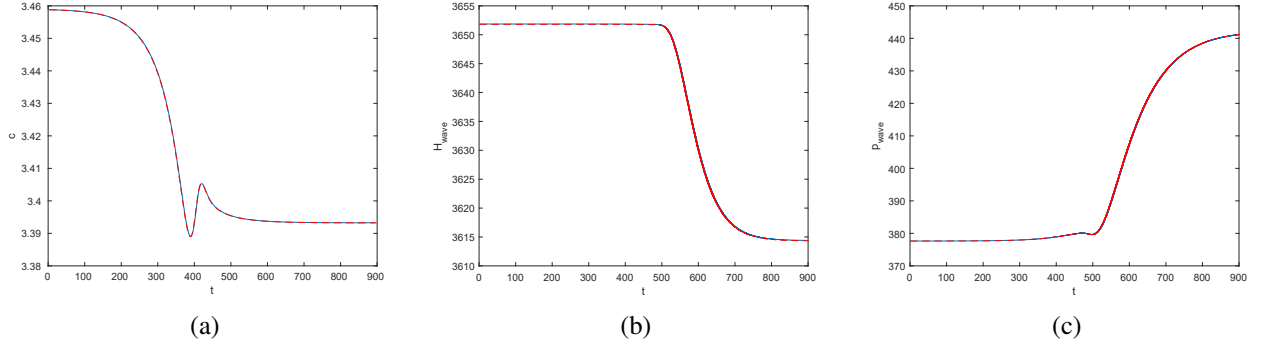


Figure 5: (a) Time evolution of the velocity of wave resulting from initial perturbation with $\epsilon = -0.25$ of the unstable STW with velocity 3.459 (point B in Fig. 3) at $(\alpha, J) = (0.165, 0.1)$. The velocity evolution is non-monotone: it initially decreases, then increases over a small time interval and then decreases again to the value 3.3932 (point B_1 in Fig. 3) towards the end of the simulation. (b) Time evolution of the energy of the STW. (c) Time evolution of the momentum of the STW. The red dashed lines show the evolution with small-amplitude random noise added to the initial perturbation, while the solid blue lines correspond to the simulations without the additional noise.

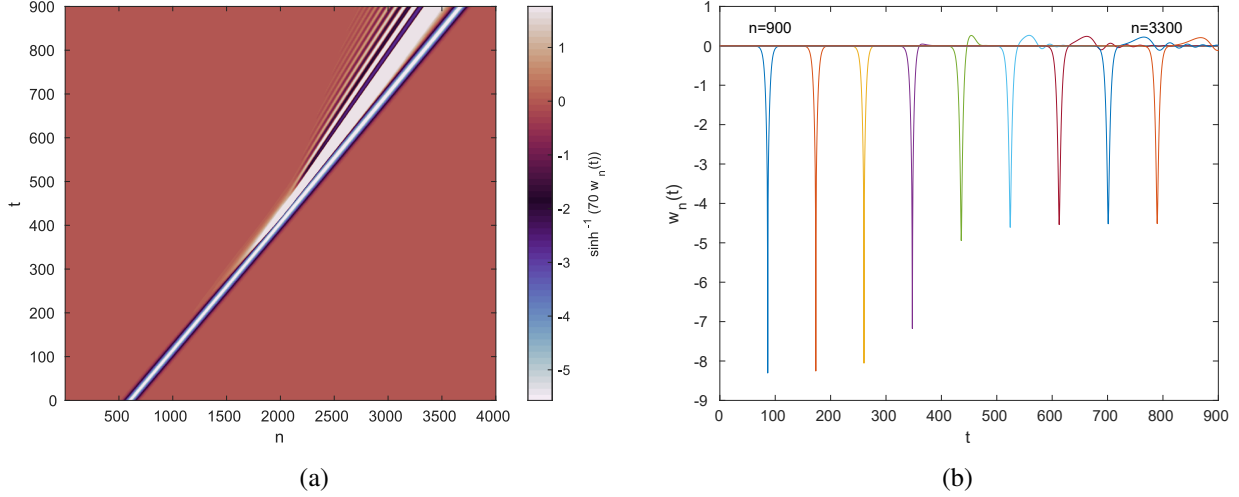


Figure 6: (a) Space-time and (b) time evolution of $w_n(t)$ at fixed n during the transition from B to B_1 shown in Fig. 5. A primarily tensile dispersive shock wave is expelled by the main waveform as it slows down. Here $n_0 = 701$, and the selected values of n are spaced 300 units apart in (b). In (a) and other space-time plots shown below, we plot $\sinh^{-1}(70w_n)$ instead of w_n so that the structure of the expelled secondary waves is more pronounced.

The dynamics is quite different when the velocity of the perturbed unstable wave increases (see Fig. 7). In this case, a small-amplitude STW, trailed by small-amplitude oscillations, forms behind the main waveform and eventually separates from it since it travels with a smaller velocity; see Fig. 8.

The momentum of the primary wave decreases during the evolution due to the positive momentum of the slower wave.

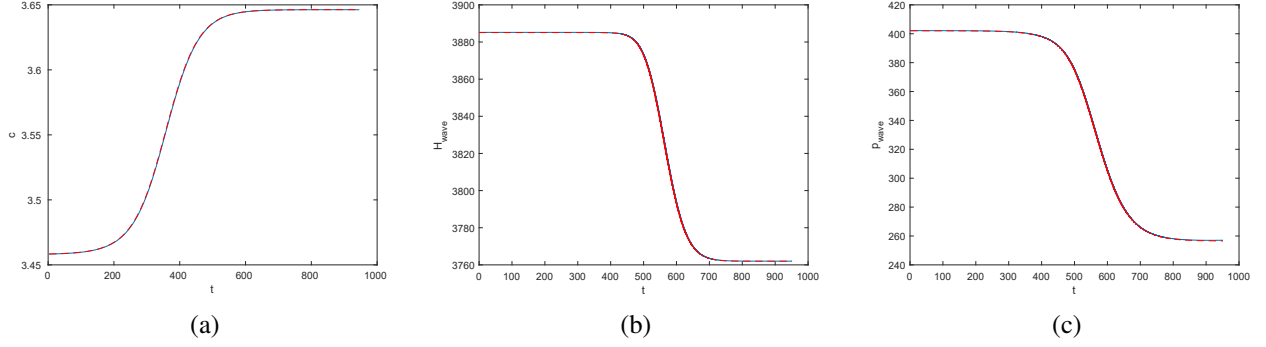


Figure 7: (a) Time evolution of the velocity of wave resulting from initial perturbation with $\epsilon = 0.25$ of the unstable STW with velocity 3.458 (point A in Fig. 3) at $(\alpha, J) = (0.165, 0.1)$. The velocity increases, approaching the value 3.6462 (point A_2 in Fig. 3) towards the end of the simulation. (b) Time evolution of the energy of the STW. (c) Time evolution of the momentum of the STW. The red dashed lines show the evolution with small-amplitude random noise added to the initial perturbation, while the solid blue lines correspond to the simulations without the additional noise.

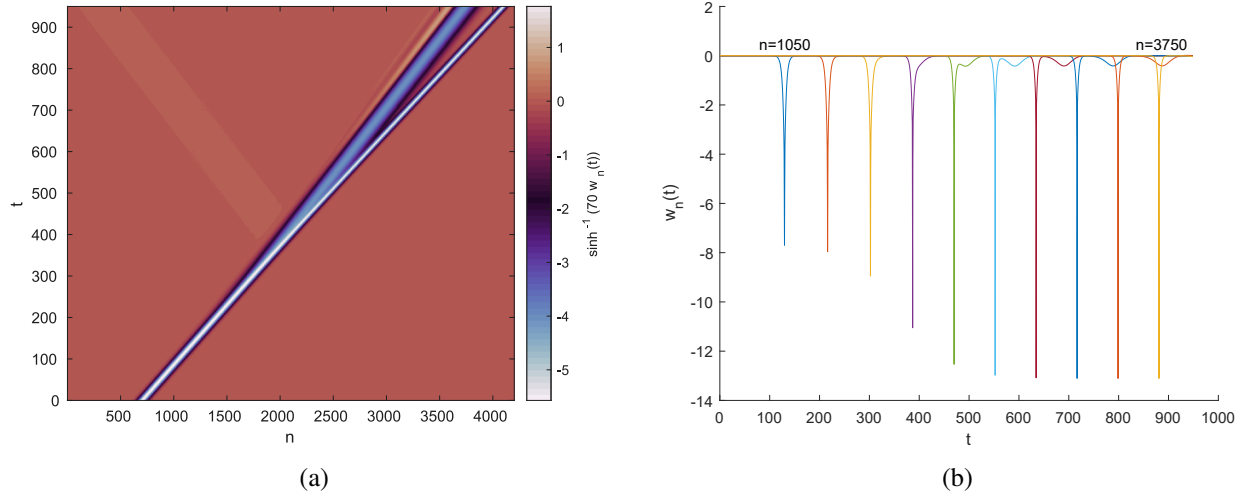


Figure 8: (a) Space-time and (b) time evolution of $w_n(t)$ at fixed n during the transition from A to A_2 shown in Fig. 7. A compressive small-amplitude STW, trailed by small amplitude oscillations, forms behind the main nonlinear waveform and eventually separates from it as the main wave increases its velocity. Here $n_0 = 701$, and the selected values of n are spaced 300 units apart in (b).

2.4 Results for the Z -region

We now consider the Z -region. Recall that in this parameter region the function $H(c)$ becomes multivalued in a certain velocity interval. Using the pseudo-arclength algorithm, as described in Sec. 2.2, we computed such curves and analyzed the linear stability of the corresponding STWs for various parameter values in the region. Below we just describe the representative case $\alpha = 0.1$, $J = 0.012$. The energy-velocity plot for these parameter values is shown in Fig. 9(a). Along the

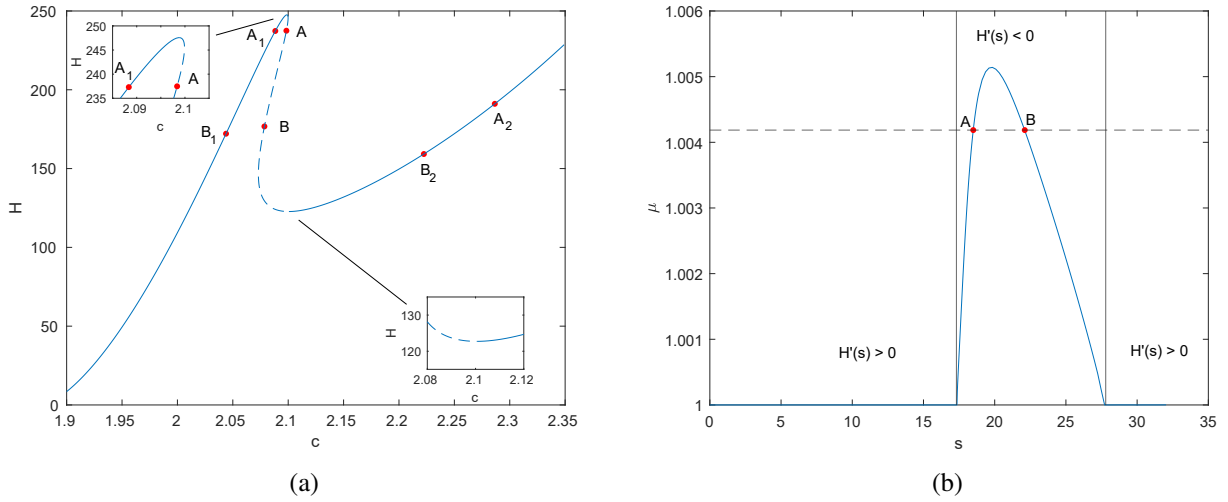


Figure 9: (a) Energy H versus velocity c of STWs at $(\alpha, J) = (0.1, 0.012)$. Points A and B correspond to the energy and velocity of the tested waves, and points A_1 , A_2 , B_1 , and B_2 mark the corresponding final velocities and energies of the stable waves the perturbed unstable STWs have evolved into. The dashed line corresponds to the portion of the curve where $H'(s) < 0$, and insets zoom in around the points where $H'(s) = 0$. (b) Maximal real Floquet multiplier μ as a function of the parameter s . The solid vertical lines indicate the values of s where $H'(s) = 0$. The dashed horizontal line marks the value $\mu = 1.0042$. In both figures, point A corresponds to the STW with velocity 2.0984 and point B corresponds to the STW with velocity 2.0785.

curve $c = c(s)$ and $H = H(s)$, and each of these is a nonmonotone up-down-up function, so that both $H'(s)$ and $c'(s)$ change sign twice; i.e., $H(c)$ is triple-valued within a relevant interval of Fig. 9(a). However, the changes in monotonicity of $H(s)$ and $c(s)$ do not take place simultaneously, as can be seen in the insets of Fig. 9(a). Specifically, the first sign change for $H'(s)$, from positive to negative, occurs slightly before $c(s)$ starts decreasing, and $c'(s)$ changes its sign back to positive prior to $H'(s)$. Thus we have $c'(s) > 0$ at both values of s where $H'(s)$ crosses zero.

As discussed in Appendix A, each threshold value of s where $H'(s) = 0$ corresponds to an increase in multiplicity of the zero eigenvalue of the operator associated with the linearized problem,

which suggests a change in stability. The Hamiltonian nature of the problem implies that at the threshold value two symmetric imaginary eigenvalues meet at the origin and emerge on the real axis as $\pm\lambda$, $\lambda > 0$, as the wave becomes unstable, so that a real Floquet multiplier $\mu = \exp(\lambda/c) > 1$ appears in the unstable regime. To verify this for our numerically computed STWs, we plot in Fig. 9(b) the maximal real Floquet multiplier μ as the function of s for the obtained solutions. One can see that $\mu > 1$ in the interval of s that nearly coincides with the interval where $H'(s) < 0$ (similarly to the observations in the previous section, $H'(s)$ is slightly below zero at the threshold values due to the finite length of the computational domain, though this numerical artifact is not visible in Fig. 9(b)). Thus, three STWs coexist for each c in the velocity interval where $c'(s) < 0$. Among these, the waves where $H'(s) < 0$ are unstable. This always includes the intermediate-energy wave, in agreement with the numerical observations in [41], but low-energy and high-energy waves also become unstable near the left and right ends of the velocity interval, respectively.

The splitting of the zero eigenvalue and transition to instability near the maximum and minimum of $H(s)$ are illustrated in Fig. 10. The plots show $\nu^2(s)$, where $\nu(s) = \lambda(s)/c(s)$ is a rescaled near-

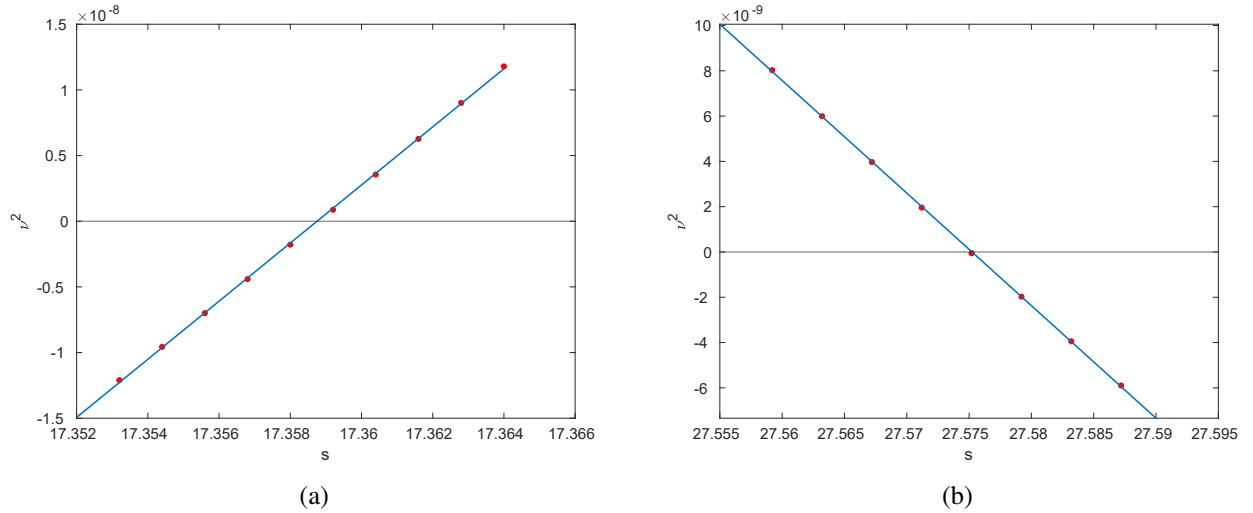


Figure 10: Squared rescaled near-zero eigenvalues $\nu(s) = \lambda(s)/c(s) = \ln(\mu(s))$ near (a) the maximum and (b) the minimum of $H(s)$ at $(\alpha, J) = (0.1, 0.012)$. The straight lines show the best linear fit in each case. The black horizontal lines mark $\nu = 0$.

zero eigenvalue (note that $\nu = \ln(\mu)$, where μ is the corresponding Floquet multiplier near 1). As the stability threshold is crossed into the unstable region in each case, a symmetric pair of purely imaginary eigenvalues ($\nu^2 < 0$) becomes a symmetric pair of real eigenvalues ($\nu^2 > 0$). We note

that $\nu^2 \sim s - s_0$ near each threshold s_0 is in agreement with the approximation derived in [31, 32] (however, see Appendix A for the discussion of the effect of a weighted-space strain formulation that destroys the Hamiltonian structure of the problem on the multiplicity of the zero eigenvalue at the stability threshold).

We now examine the dynamical fate of unstable solutions. We consider two cases with velocities 2.0785 and 2.0984 that have the same Floquet multiplier $\mu = 1.0042$, which corresponds to eigenvalues $\lambda = 0.0087$ and 0.0088 , respectively. Similar to the previously discussed cases for the N -region, the waves either slow down after expelling a dispersive wave or speed up after expelling a small-amplitude solitary wave, depending on the sign of the perturbation ϵ .

The slowing-down case for the unstable STW with velocity 2.0785 (point B in Fig. 9) is shown in Fig. 11 and Fig. 12. Note that the wave's velocity experiences a highly nonmonotone evolution

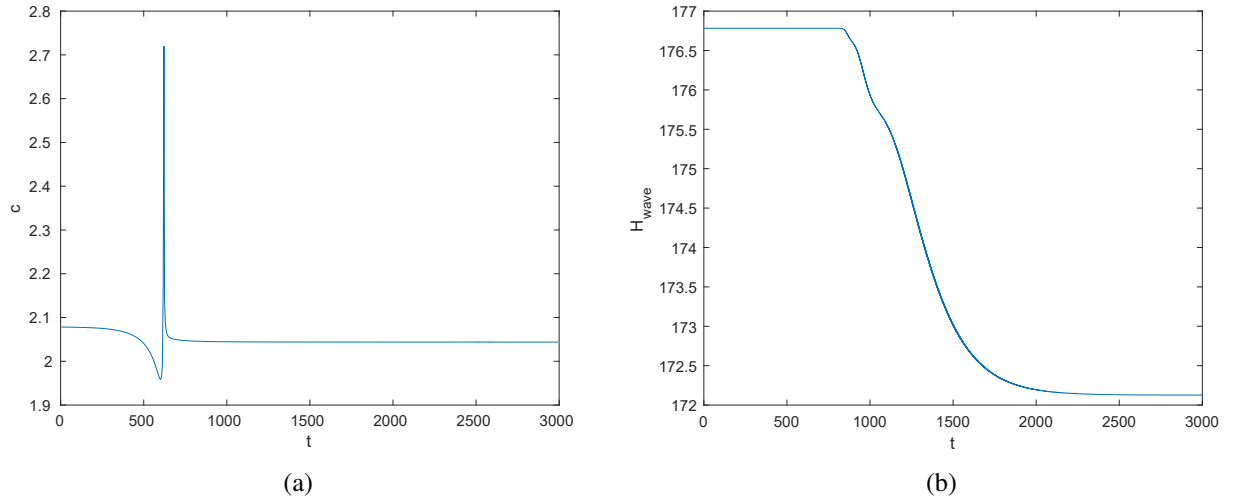


Figure 11: (a) Time evolution of the velocity of wave resulting from initial perturbation with $\epsilon = -0.25$ of the unstable STW with velocity 2.0785 (point B in Fig. 9(a)) at $(\alpha, J) = (0.1, 0.012)$. The final velocity is 2.0439 (point B_1 in Fig. 9(a)). (b) Time evolution of the energy of the STW.

in this case but eventually settles down to a lower value than the speed of the perturbed wave (point B_1 in Fig. 9(a)), as can be seen in Fig. 11(a). Fig. 13 zooms in the space-time plot of $w_n(t)$ in the time interval that includes times when the propagation velocity in Fig. 11(a) reaches its minimum and maximum. One can see that expulsion of the dispersive wave starts shortly after the velocity reaches its peak value.

When the sign of the perturbation is reversed, the wave speeds up after expelling a small-amplitude

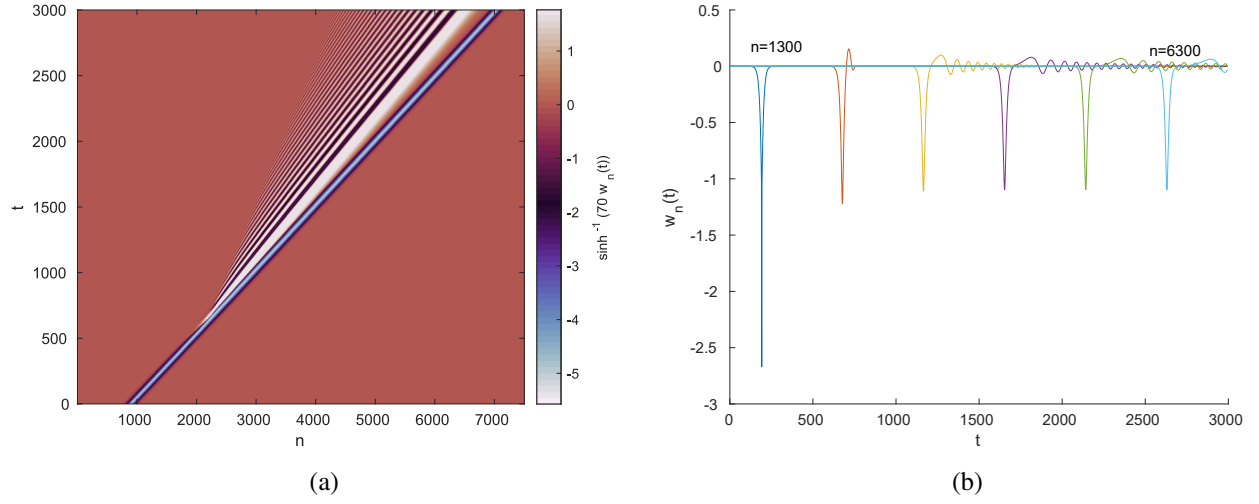


Figure 12: (a) Space-time and (b) time evolution of $w_n(t)$ at fixed n during the transition from B to B_1 shown in Fig. 11. A dispersive shock wave is expelled by the main waveform as it slows down. Here $n_0 = 901$, and the selected values of n are spaced 1000 units apart in (b).

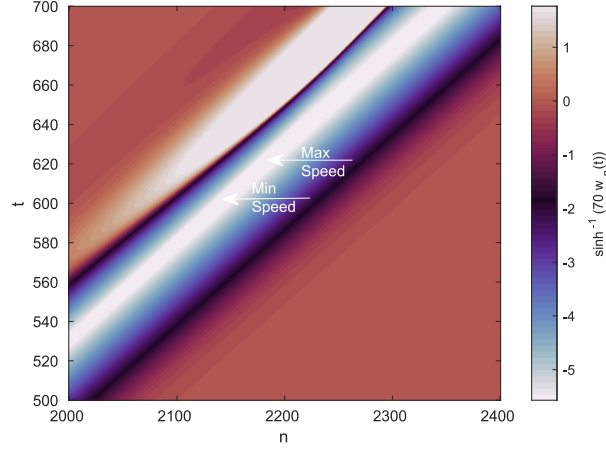


Figure 13: An enlarged view of the space-time plot Fig. 12(a). The arrows mark the points corresponding to the minimal and maximal values of the wave's velocity in Fig. 11(a).

STW, and the ensuing dynamics is similar to the one shown in Fig. 7 and Fig. 8 for the N -region. Similar slowing-down and speeding-up scenarios are observed for simulations perturbing the unstable wave that corresponds to point A in Fig. 9(a).

2.5 Concluding remarks

In this chapter we have revisited the existence, stability and dynamical features of lattice traveling waves in models where the competition between short-range nonlinear interactions and longer-range linear interactions may give rise to stability changes. To this end, we considered the model where the nearest neighbors feature an α -FPU interaction, while interactions beyond nearest neighbors are harmonic with exponentially decaying strength, and investigated different parameter regimes. The regime where the strength and rate of decay of the longer-range interactions were such that the energy H of solitary traveling waves was a nonmonotone function of their velocity c (N -region) was observed to yield instability when $H'(c) < 0$, in line with earlier work. A more detailed study was also performed in Z -region of the parameter space where $H(c)$ was not even single-valued. There, it was revealed that instability corresponds to $H'(s) < 0$, where s is a parameter along the energy-velocity curve. In Appendix A we proved that the change in the sign of $H'(s)$ is associated with the increase of the multiplicity of the zero eigenvalue.

A focal point of the present study concerned the dynamics of unstable solutions in the regions where Floquet multipliers μ of the associated spectral stability analysis were found to satisfy $\mu > 1$. There, it was seen that it is possible to “kick” the unstable waveforms through suitable multiples of the eigenvector associated with the instability to induce them to acquire a higher velocity, or recede to a lower speed. In each of the cases, the velocity modification was accompanied by the concurrent emission of a suitable coherent structure, typically represented by a slower pulse in the speeding-up case and a dispersive shock wave when slowing-down. Such possibilities were explored in both N and Z parameter regions.

Numerous questions arise as possible extensions of the present work towards future study. In particular, it is important to understand on a more general level what fundamental ingredients a physical setting must have in order to induce the kind of competition that leads to $H'(c) < 0$ and the associated instability as is the case herein. An interesting and highly nontrivial extension of the present study in a one-dimensional lattice setting would involve going beyond traveling waves and examining breathers that bear a further internal frequency (in addition to the traveling one). Finally, studies of solitary traveling waves in lattices have been mostly limited to one-dimensional setting, and little is known about existence and stability of such structures in higher dimensions. A systematic investigation of this issue in a suitably chosen model would be a topic of interest in its own right.

3.0 Moving discrete breathers in a β -FPU lattice

In this chapter, we consider moving discrete breathers in a β -FPU lattice. In particular, we develop a numerical procedure that allows a systematic construction of breathers traveling more than one lattice site per period. The procedure involves a Newton iterative method and a continuation along a sequence of velocities. We use Floquet analysis to investigate the stability spectrum of the obtained solutions. Our results show that the energy of the moving breathers is in general a multivalued function of their internal frequency and reveal a genuinely nonlinear nature of the resonances identified in the earlier work [78]. We also investigate the fate of unstable moving breathers perturbed along the corresponding eigenmode and show that the ensuing dynamics typically slows them down over a large simulation time.

The chapter is organized as follows. We formulate the problem in Sec. 3.1 and describe our numerical procedures in Sec. 3.2. In Sec. 3.3, we examine the dependence of the moving breather with different period-wise velocities on the internal frequency and discuss the multivalued nature of the obtained energies, resonances and stability. Consequences of the observed exponential instabilities in the breather dynamics are explored in Sec. 3.4. Concluding remarks can be found in Sec. 2.5, along with some suggestions for future work. In Appendix B.1, we discuss additional solutions that coexist with the ones described in Chapter 3 but have different linear spectra. The effect of the lattice size is discussed in Appendix B.2.

3.1 Problem formulation

We consider a lattice of N particles with nearest-neighbor interactions governed by a β -FPU potential. In dimensionless variables the Hamiltonian of the system is given by

$$H = \frac{1}{2} \sum_{n=1}^N p_n^2 + \sum_{n=1}^N \left(\frac{1}{2} (q_{n+1} - q_n)^2 + \frac{\beta}{4} (q_{n+1} - q_n)^4 \right) = \sum_{n=1}^N e_n, \quad (14)$$

where q_n denotes the displacement of the n th particle, $p_n = \dot{q}_n = dq_n/dt$ is its momentum (the mass is rescaled to unity), β measures the strength of the nonlinear coupling, and

$$e_n = \frac{1}{2}p_n^2 + \frac{1}{4}[(q_{n+1} - q_n)^2 + (q_n - q_{n-1})^2] + \frac{\beta}{8}[(q_{n+1} - q_n)^4 + (q_n - q_{n-1})^4] \quad (15)$$

is the site energy density. The equations of motion are

$$\ddot{q}_n = q_{n+1} + q_{n-1} - 2q_n + \beta [(q_{n+1} - q_n)^3 - (q_n - q_{n-1})^3]. \quad (16)$$

In what follows, we assume that N is even and prescribe periodic boundary conditions: $q_{n+N} = q_n$, $p_{n+N} = p_n$. We also assume $\beta > 0$ and note that in this case the rescaled variables $\tilde{q}_n = q_n\sqrt{\beta}$ satisfy (16) with $\beta = 1$. Thus, it suffices to consider $\beta = 1$ in the numerical results presented in this work.

The β -FPU problem (16) is known to have two types of stationary discrete breather solutions $q_n(t) = x_n(t)$ that are time-periodic, $x_n(T) = x_n(0)$, and spatially localized in terms of the relative displacements $x_n - x_{n-1}$. Here, $T = 2\pi/\omega$ is the period of internal oscillations with frequency ω . The first type is the site-centered Sievers-Takeno (ST) mode [51], with displacement that has even symmetry about the center, and the second type is the bond-centered Page (P) mode [52], with odd displacement. The P mode is linearly stable, while the ST mode is unstable [53]. Perturbing an ST mode along an eigenmode corresponding to the instability sets the breather in motion.

Our focus here is on *moving* discrete breathers that propagate r lattice sites over s periods $T = 2\pi/\omega$ of internal oscillations and satisfy [78]

$$\begin{bmatrix} \{q_n(sT)\}_{n=1}^N \\ \{p_n(sT)\}_{n=1}^N \end{bmatrix} - (-1)^r \begin{bmatrix} \{q_{n-r}(0)\}_{n=1}^N \\ \{p_{n-r}(0)\}_{n=1}^N \end{bmatrix} = \mathbf{0}, \quad (17)$$

where the indices are mod N due to periodic boundary conditions. Here s and r are integers, and

$$V_1 = \frac{r}{s} \quad (18)$$

denotes the period-wise velocity of the breather (the number of lattice sites transversed over the period of one internal oscillation), while its translational velocity is given by

$$V_2 = \frac{V_1}{T} = \frac{r}{sT}. \quad (19)$$

3.2 Numerical Methods

To obtain moving breathers, we must find fixed points of the map defined by (17) using the Newton iterative method, with an appropriately perturbed unstable ST stationary breather, whose instability induces the breather mobility, as an initial seed. Here and in what follows, we use a symplectic and explicit fourth-order Runge-Kutta-Nyström algorithm [82] to integrate the equations of motion. We found that over the course of the simulations, the total energy is conserved up to the relative error of the order of 10^{-10} . We start by constructing an ST breather $x_n(t)$ with a given internal frequency ω , using the Newton iterative method and numerical continuation from the anticontinuous limit [117]. Linearizing (16) around the ST breather by setting $q_n(t) = x_n(t) + \epsilon y_n(t)$ and considering $O(\epsilon)$ terms, we obtain

$$\ddot{y}_n - (y_{n+1} + y_{n-1} - 2y_n) - 3((x_{n+1} - x_n)^2(y_{n+1} - y_n) - (x_n - x_{n-1})^2(y_n - y_{n-1})) = 0,$$

which is used to compute the monodromy matrix \mathcal{F} defined by

$$\begin{bmatrix} \mathbf{y}(T) \\ \dot{\mathbf{y}}(T) \end{bmatrix} = \mathcal{F} \begin{bmatrix} \mathbf{y}(0) \\ \dot{\mathbf{y}}(0) \end{bmatrix}, \quad (20)$$

where the vector functions $\mathbf{y}(t)$ and $\dot{\mathbf{y}}(t)$ have components $y_n(t)$ and $\dot{y}_n(t)$, respectively. The Floquet multipliers μ are obtained by finding the eigenvalues of \mathcal{F} , once the iterative procedure has converged. Recall that a Floquet multiplier satisfying $|\mu| > 1$ indicates instability. An ST mode has an unstable eigenmode corresponding to a real Floquet multiplier $\mu > 1$; naturally, due to the Hamiltonian nature of the problem, there exists a complementary (inverse) one with $\mu < 1$. Following [73], we obtain the initial seed for a moving breather by applying a kinetic perturbation to the ST breather. Specifically, we use the momentum part $\delta\mathbf{p}$ of the eigenvector associated with the instability, so that our initial guess for the moving breather is given by

$$\begin{bmatrix} \mathbf{q} \\ \mathbf{p} \end{bmatrix} = \begin{bmatrix} \mathbf{x}(0) \\ \mathbf{0} \end{bmatrix} + \lambda \begin{bmatrix} \mathbf{0} \\ \delta\mathbf{p} \end{bmatrix}, \quad (21)$$

where λ is the strength of the perturbation.

To construct moving breathers with $V_1 = 1/s$ for some integer $s \geq 1$, we use the Newton iterative method to find fixed points of (17) with initial guess (21) as the values of λ are being incremented

within some interval. We typically start with $\lambda = -1$ and increase it by 10^{-2} up to $\lambda = 1$. Once this has been completed, we look at the solutions for which the square of the ℓ^2 norm of the objective function of the Newton iteration, defined by the left hand side of (17), is below some threshold. Doing this allows us to obtain moving breathers on different branches in the (ω, H) plane near the resonance values of ω , as described below. Solutions with other frequency values are then found using parameter continuation along each branch. Typically, this continuation was done in ω , but near the turning points for ω we used H as a continuation parameter. We found that this method successfully generates moving breathers with $r = 1$ but has not worked in the examples we considered for velocities with $r > 1$.

To compute moving breathers with period-wise velocity $V_1 = r/s$, where $r > 1$, we have developed the following numerical procedure. We use one of the moving breathers with $V_1 = 1/s_0$ for some integer s_0 as an initial guess and construct a monotone sequence v_1, v_2, \dots, v_k of rational values of the period-wise velocity that are close enough together and satisfy $v_1 = 1/s_0$ and $v_k = r/s$. These values are chosen in a way that minimizes s while staying within a prescribed step difference, empirically selected to be between 0.018 and 0.022. Depending on the value of ω chosen, it is possible that for one of the chosen v_i , the moving breather solution will be close to a resonance; in this case, a larger step in v_i is needed to bypass the resonance. For example, to compute a moving breather with $V_1 = 5/7$ we used the sequence

$$\{v_i\} = \{1/2, 12/23, 13/24, 9/16, 7/12, 23/38, 5/8, 20/31, 2/3, 11/16, 5/7\}.$$

We then perform a continuation procedure that involves obtaining the moving breather with velocity v_i using Newton's iterative method and the breather with velocity v_{i-1} as the initial guess. An example of a moving breather with $V_1 = 14/23$ and $\omega = 2.5$ obtained using this method is shown in Fig. 14(a,b).

To determine the stability of a computed moving breather, we linearize (16) about it and construct the monodromy matrix \mathcal{F} defined by

$$\begin{bmatrix} \{y_{n+\tilde{r}}(\tilde{s}T)\}_{n=1}^N \\ \{\dot{y}_{n+\tilde{r}}(\tilde{s}T)\}_{n=1}^N \end{bmatrix} = \mathcal{F} \begin{bmatrix} \{y_n(0)\}_{n=1}^N \\ \{\dot{y}_n(0)\}_{n=1}^N \end{bmatrix}, \quad (22)$$

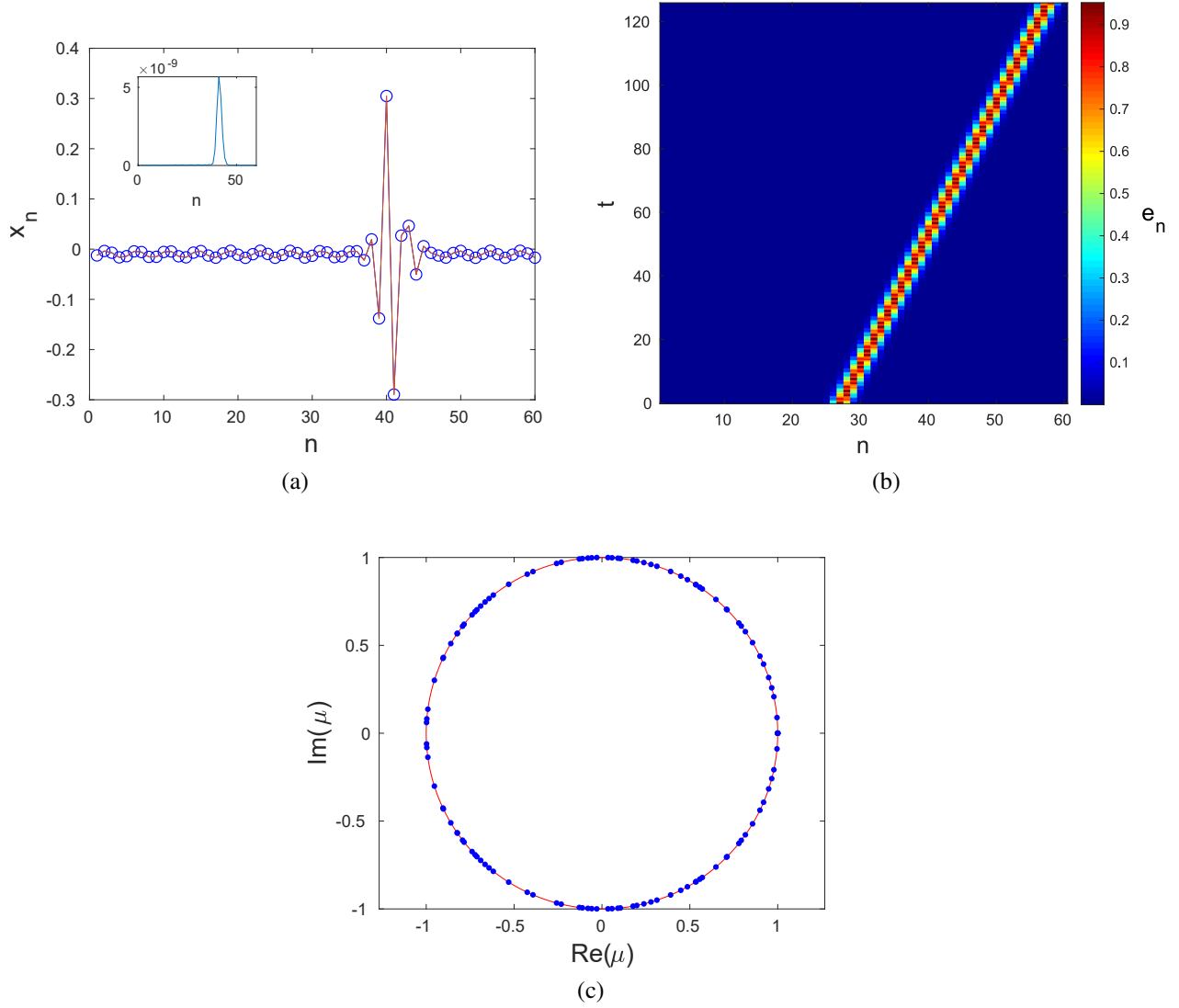


Figure 14: (a) Verification of the relation described in (17) for the moving breather with period-wise velocity $V_1 = 14/23$ and internal frequency $\omega = 2.5$. The blue circles are the displacements at time $t = 23T$, while the solid red line is the displacement at time $t = 0$ shifted to the right by 14 lattice sites. The inset shows the absolute difference between the two sets of displacements. (b) Space-time evolution of the site energy $e_n(t)$. (c) Floquet multipliers μ associated with the linearization around the solution of panels (a)-(b). The absence of multipliers lying off of the unit circle suggests the spectral stability of the relevant waveform.

where $\tilde{r} = r$, $\tilde{s} = s$ if r is even and $\tilde{r} = 2r$, $\tilde{s} = 2s$ if r is odd. Fig. 14(c) shows the Floquet multipliers for the breather with $V_1 = 14/23$ and internal frequency $\omega = 2.5$. This breather appears to be linearly stable.

To explore the consequences of an instability associated with a real Floquet multiplier $\mu > 1$ for

a moving breather, we perturb it along the corresponding eigenmode and use the following method to approximate the translational velocity V_2 of the ensuing waveform as a function of time. The procedure involves computing the location of the center of the energy density of the moving breather. We divide the time interval $[t_i, t_f]$, where t_i is the initial and t_f is the final time, into subintervals of length Δt , thus selecting sample times t_i such that $t_{j+1} - t_j = \Delta t$. Typically, we set $\Delta t = sT$, where T is the internal period and s is the number of periods the unperturbed breather needs to advance r sites. At each time t_j , we compute the energy density $e_{n,j}$ and use it to obtain an approximation for the center X_j of the waveform:

$$X_j = \frac{\sum_{n \in \{\text{core}\}} n e_{n,j}}{\sum_{n \in \{\text{core}\}} e_{n,j}}. \quad (23)$$

In order to improve the accuracy of this approximation, we use a spline interpolation of the energy density. We then compute (23) including the interpolated points in the core of the moving breather. To determine the width of the core, we start from the maximum of the energy density. We then traverse the chain until the absolute difference between the energy density and wing energy, which is determined by averaging the ten particles that make up the wings, is on the order of 10^{-4} . [We have verified that using smaller tolerances, on the orders of 10^{-5} and 10^{-6} , yields a negligible difference in the results, approximately 0.04%. Hence, the selection of the cutoff is representative, while its precise threshold value is not crucial to our observations described below.] The distance between the particle where the maximum occurs and the cutoff particle is half of the core width. We choose as a center point the maximum of the interpolated energy density. Once the weighted energy center has been found, we repeat the above procedure using the weighted energy center as the center point. This has little effect for waveforms with small-amplitude wings, but when the wings have larger amplitude, the recalculation is necessary to compensate for the effect they have on the energy density as the center crosses a boundary. The translational velocity $V_2(t)$ of the wave is then approximated by

$$V_2(t_j) \approx \frac{X_{j+1} - X_j}{t_{j+1} - t_j}. \quad (24)$$

3.3 Frequency dependence, resonances and stability

We now investigate the dependence of the moving breather solutions on the internal frequency ω at fixed period-wise velocity V_1 and the lattice size N . The results for $V_1 = 1/3$ and $N = 60$ are

shown in Fig. 15. Panel (a) shows the total energy (Hamiltonian) H as a function of ω . One can

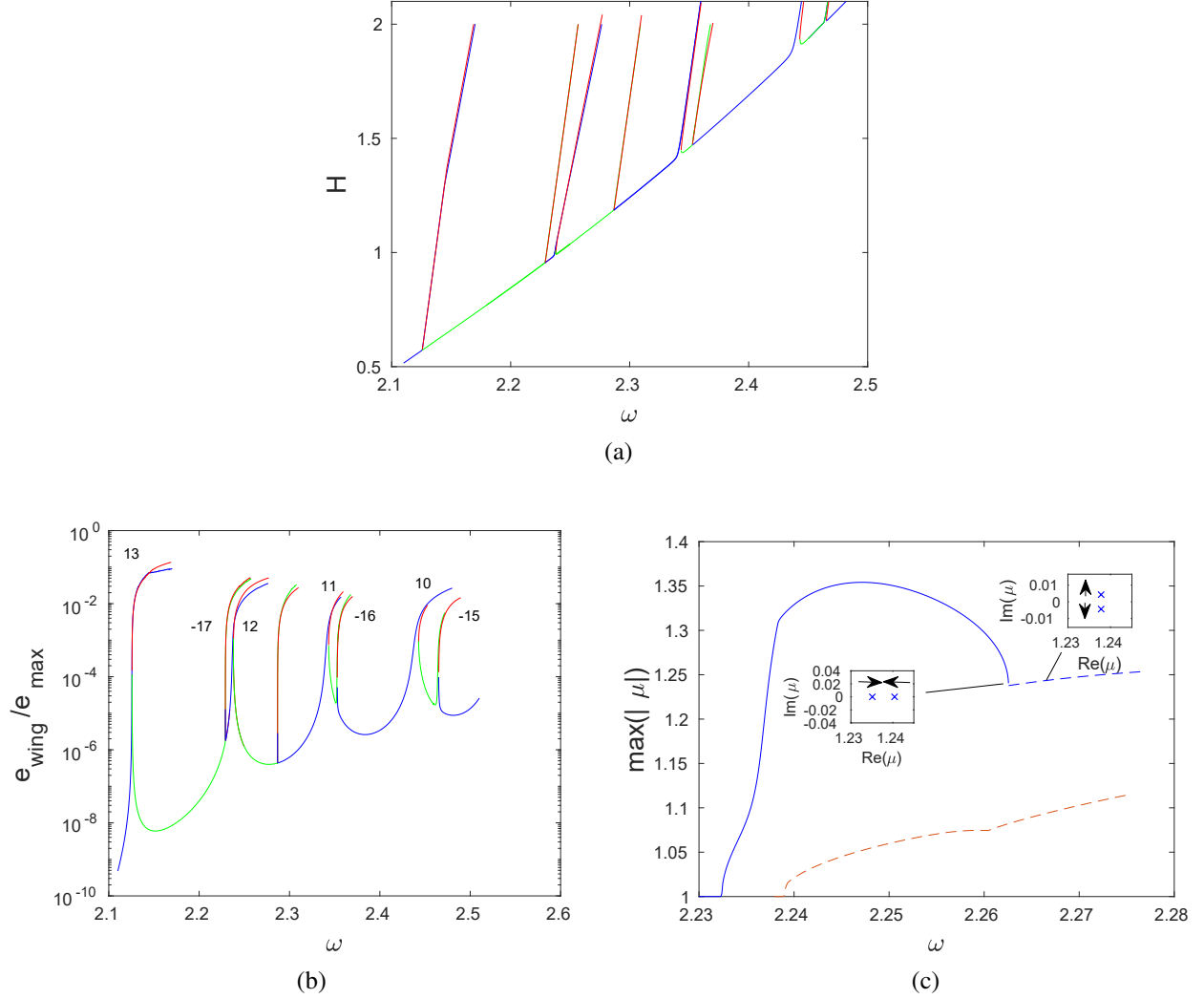


Figure 15: (a) Energy H , (b) the normalized average site energy $e_{\text{wing}}/e_{\text{max}}$ of the wings and (c) the maximum moduli of the Floquet multipliers μ along different branches as functions of ω at $V_1 = 1/3$ and $N = 60$ near the resonance $\omega = 2.237$. The Floquet multiplier with the maximum modulus has nonzero real and imaginary parts along dashed portions the curve and is real along the solid one. Insets illustrate that this transition occurs due to the collision of a pair of real Floquet multipliers and subsequent emergence of a quadruplet of complex-valued multipliers symmetric about the unit circle (only the pair of such multipliers outside the unit circle is shown in the second inset). Different colors correspond to different branches in (a). The numbers in (b) are the values of m for the corresponding resonances (see the text for detail).

see that there is a number of resonances at certain frequency values. At these values, the amplitude of the wing oscillations rapidly increases. Near the resonance frequencies, the breather energy is a *multivalued* function of ω . Indeed, near each resonance frequency, the curve can be split into three pieces: the top branch, the middle branch, and the bottom branch, where the middle and bottom

branches are connected to each other by a turning point. We distinguish between the bottom and top branches by alternating colors between green and blue at each resonance. Note that the bottom branch corresponding to one resonance frequency eventually merges with the top branch near another resonance. Along the three branches near each resonance, there are distinct moving breathers with the same internal frequency, as illustrated in Fig. 16 for $\omega = 2.126$.

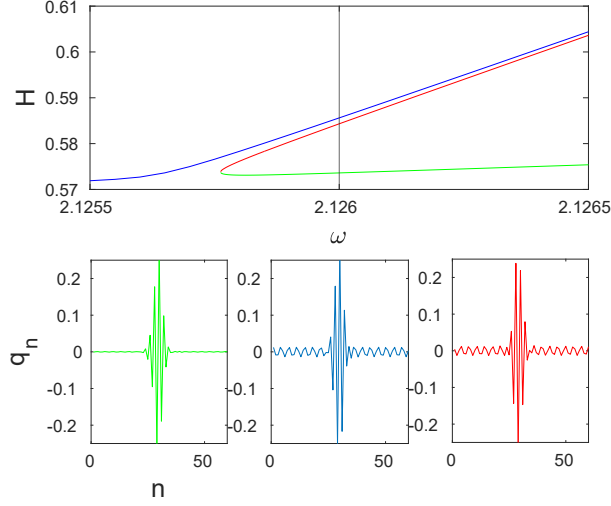


Figure 16: The top panel shows a zoomed-in view of the resonance near $\omega = 2.126$. The black vertical line marks $\omega = 2.126$ at which three different moving breathers coexist. These breathers are shown in the three bottom panels, where colors match the respective branches depicted in the top panel. Here $V_1 = 1/3$ and $N = 60$.

Panel (b) of Fig. 15 shows the corresponding average site energy in a wing portion of the breather, normalized by the maximum site energy. One can clearly see the *nonlinear* character of the resonances, with rapid increase in wing energy followed by a more gradual one. Both the nonlinear form of the resonances and the multivalued nature of the frequency dependence were, apparently, missed in the earlier computations [74, 78].

Yoshimura and Doi in [78] used a normal mode analysis to approximate resonance frequencies. For completeness, we briefly describe the main steps of their derivation. The normal mode coordinates $Q_m(t)$, $m = -N/2 - 1, \dots, N/2$, are defined by [118]

$$q_n(t) = \frac{(-1)^n}{\sqrt{N}} \sum_{m=-(N/2-1)}^{N/2} Q_m(t) \left[\cos\left(\frac{2\pi}{N}mn\right) - \sin\left(\frac{2\pi}{N}mn\right) \right], \quad n = 1, 2, \dots, N$$

and have the natural frequency associated with the dispersion relation:

$$\Omega_m = 2 \cos\left(\frac{\pi m}{N}\right). \quad (25)$$

For stationary breathers these modes are approximated in [78] using the method in [119] with frequency ω , which yields $Q_m(t) \approx A_m \cos(\omega t)$, where

$$A_m = \frac{\pi}{2\sqrt{6\beta N}} \operatorname{sech} \left[\frac{\pi^2 m}{N\sqrt{\omega^2 - 4}} \right]. \quad (26)$$

Complex normal modes $U_m(t) = \frac{1}{2}(Q_m + Q_{-m}) + \frac{i}{2}(Q_m - Q_{-m})$ are then used to construct moving breather solutions with $V_1 = r/s$ in the form

$$U_m(t) = \psi_m(t) e^{-i \frac{mr}{Ns} \omega t},$$

where $\psi_m(t)$ are complex-valued functions satisfying

$$\begin{aligned} & \frac{d^2 \psi_m}{dt^2} - i \frac{2mr\omega}{Ns} \frac{d\psi_m}{dt} + \left\{ \Omega_m^2 - \left(\frac{mr\omega}{Ns} \right)^2 \right\} \psi_m \\ &= -\frac{\beta}{N} \sum_{i,j,k=-N_h}^{N_h} \Omega_m \Omega_i \Omega_j \Omega_k \psi_i \psi_j \psi_k \cdot e^{i\{m-(i+j+k)\}r/Ns\omega t} \Delta(m - (i + j + k)), \end{aligned} \quad (27)$$

where $\Delta(m) = (-1)^m$ if $r = mN$ for $m \in \mathbb{Z}$ and zero otherwise, $N_h = N/2 - 1$, and Ω_m is defined in (25). The solution of (27) is then sought in the form

$$\psi_m(t) = \psi_m^0(t) + u_m(t), \quad \psi_m^0(t) = \sum_{\ell=\pm 1} A_m e^{i\ell\omega t}, \quad u_m(t) = \sum_{n=-\infty}^{\infty} a_{m,n} e^{in(\omega/s)t}, \quad (28)$$

where $u_m(t)$ is the deviation from the stationary breather $\psi_m^0(t)$ with A_m given by (26), and both components are periodic functions with period sT that are expanded in Fourier series, with coefficients $a_{m,n}$ for $u_m(t)$. Here, only the dominant fundamental frequency components are kept in the expansion for $\psi_m^0(t) = A_m \cos(\omega t)$. Substituting (28) into (27) and considering the leading-order approximation in terms of $u_m(t)$ results in a linear system for $a_{m,n}$. Analysis of this system shows that $|a_{m,n}|$ becomes large when its coefficient is close to zero. Setting these coefficients to zero thus yields an approximation for the resonance frequency values ω_m , $|m| < N/2$, at which the m th normal mode is excited. The approximate resonance condition [78] is given by

$$\left| \frac{n}{s} - \frac{mr}{Ns} \right| \omega_m = \Omega_m \sqrt{1 + \frac{2}{N} \sqrt{\omega_m^2 - 4}}, \quad (29)$$

where n may take values $n = \pm s$ or $n = \pm(s \pm r)$, depending on the frequency interval and the value of $V_1 = r/s$, and we also recall (25). Using (29), we computed the values of m and ω_m for all

numer ω_m	approx ω_m	m
2.126	2.129	13
2.237	2.244	12
2.342	2.352	11
2.440	2.454	10
2.464	2.483	-15
2.352	2.364	-16
2.229	2.236	-17

Table 1: Comparison of numerical and approximate resonance values ω_m for $V_1 = 1/3$ and $N = 60$. The approximate values were computed using (29). The numerical values were computed by using the wing energy plots, such as Fig. 15(b), and estimating the frequency at the center of the gap that separates branches corresponding to each resonance.

except one of the resonances shown in Fig. 15(b); the corresponding values of m are shown in the plot. Table 1 compares the predicted values of resonance frequencies with the numerical ones.

Panel (c) of Fig. 15 shows the maximal moduli of the Floquet multipliers associated with the computed breathers near the resonance $\omega = 2.237$ as a representative example. As the top branch nears a resonance, an *exponential instability*, which corresponds to a real Floquet multiplier $\mu > 1$, manifests itself. As ω continues to increase along the branch, and the wings of the moving breathers become more pronounced, this exponential instability is accompanied by the emergence of *oscillatory instability* modes associated with Floquet multipliers μ that have nonzero imaginary part and satisfy $|\mu| > 1$ (recall the definitions in Sec. 2.2). As can be seen in the insets, the largest real multiplier is accompanied by a smaller real one that eventually collides with it. This collision results in the formation of a symmetric quadruplet of complex-valued multipliers. Meanwhile, both the bottom branch and the middle branch are stable near the resonance frequency. Understanding the relevant turning point structure that connects the two is an interesting question for future work.

In the case of the middle branch, stability only persists over a short interval of ω , as oscillatory instabilities quickly arise. In this case, the modulus of the complex multipliers is larger than that

of any real multipliers that emerge. The exponential instabilities exist as pairs of real multipliers that collide, separate and rejoin, shifting between complex and real, similar to what is seen in the top branch. This behavior is demonstrated in panel (c) of Fig. 17. The lower branch only becomes unstable as it merges with the top branch for the next resonance.

The results for $V = 2/5$ and $N = 60$ are shown in Fig. 17 and Table 2. Overall, they are

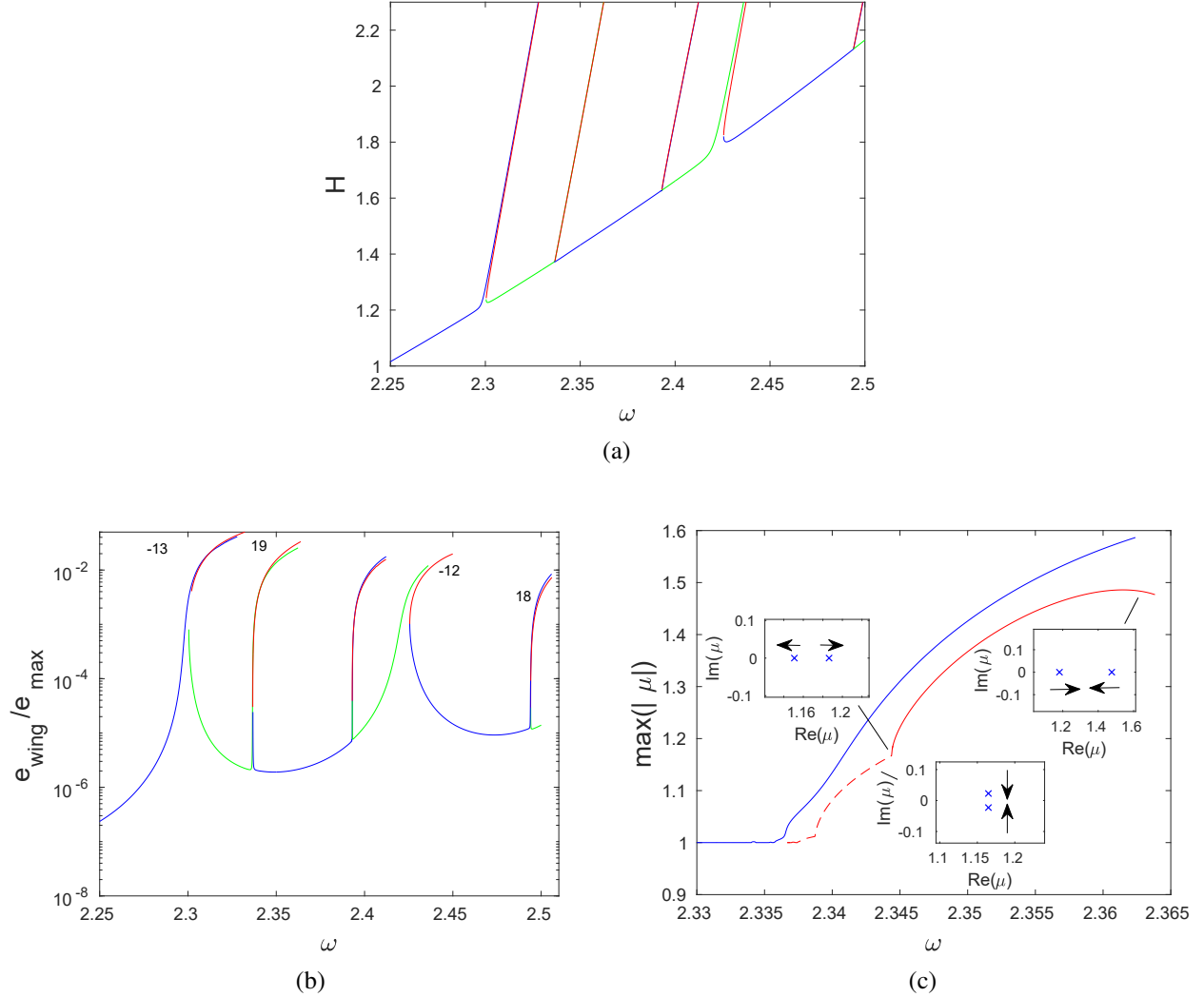


Figure 17: (a) Energy H , (b) the normalized average site energy e_{wing}/e_{max} of the wings and (c) maximum moduli of the Floquet multipliers μ along different branches as functions of ω at $V_1 = 2/5$ and $N = 60$ near the resonance $\omega = 2.337$. The Floquet multiplier with the maximum modulus has nonzero real and imaginary parts along the dashed portions of the curve and is real along the solid one. Insets illustrate that transitions between these regimes occur due to the collisions of pairs of real and complex Floquet multipliers. Different colors correspond to different branches in (a). The numbers in (b) are the values of m for the corresponding resonances (see the text for details).

similar to the case $V_1 = 1/3$, but the number of resonances is smaller over the same interval of ω .

numer ω_m	approx ω_m	m
2.337	2.348	19
2.494	2.510	18
2.423	2.434	-12
2.300	2.306	-13

Table 2: Comparison of approximate and numerical resonance values ω_m for $V_1 = 2/5$ and $N = 60$. The approximate values were computed using (29).

In both examples, one of the resonances is not accounted by (29). As can be seen in the respective figures, both positive and negative integer resonances manifest themselves sequentially in the context of (29), yet one cannot be included in this sequence. This also constitutes an intriguing question for future study. Additionally, in panel (c) of Fig. 17, the maximum moduli of Floquet multipliers along the middle branch which satisfy $|\mu| > 1$ are determined by two pairs of complex Floquet multipliers that start near the point $\mu = 1$, in contrast to the case discussed above. These complex multipliers eventually collide to form a pair of real multipliers, which initially separate but then start moving toward each other, as shown in the insets.

3.4 Dynamical consequences of exponential instabilities

We now consider the consequences of the instability of a moving breather with real Floquet multipliers $\mu > 1$. To this end, we perturb the breather along the corresponding eigenmode by solving Eq. (16) with the initial displacement vector set to $\mathbf{q}(0) + \epsilon\delta\mathbf{q}$ and initial momentum to $\mathbf{p}(0) + \epsilon\delta\mathbf{p}$, where $\mathbf{p}(t)$ and $\mathbf{q}(t)$ are the displacement and momentum vector functions, respectively, for the moving breather, $\delta\mathbf{q}$ and $\delta\mathbf{p}$ are the displacement and momentum parts of the unstable eigenmode, and ϵ measures the strength of the applied perturbation along this unstable eigendirection.

We consider the unstable moving breather with $V_1 = 1/3$, $\omega = 2.424$ and $N = 60$, from the top (blue) branch in Fig. 15, which has the maximum real Floquet multiplier $\mu = 1.0989$ (see Fig. 18).

Note that the breather has wings of relatively small amplitude. Fig. 19 shows the evolution of the translational velocity V_2 when the breather is perturbed with $\epsilon = -0.01$ (panel (a)) and $\epsilon = 0.01$ (panel (b)). In both cases, after initial transients leading to substantial deceleration, the velocity of the perturbed breather appears to stabilize and oscillate around specific values, before decreasing again and eventually coming to oscillate around zero. As an inspection of the relative sizes of the horizontal and vertical axes reveals, this is a particularly slow process. Interestingly, the $\epsilon = -0.01$ perturbation case takes much longer to reach this state.

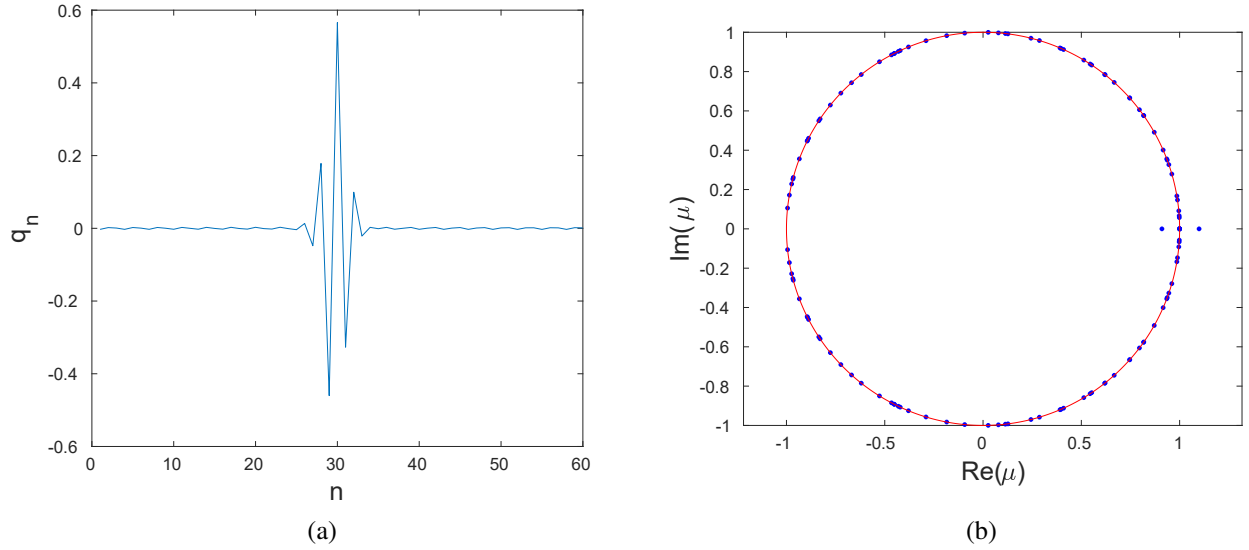


Figure 18: (a) Displacement profiles q_n of the unperturbed moving breather with $V_1 = 1/3$, $\omega = 2.424$, and $N = 60$. (b) Floquet multipliers μ . The largest real multiplier is $\mu = 1.0989$.

Figure 20 shows the space-time evolution of the energy density at the lattice nodes early on in the simulation for the case when $\epsilon = 0.01$. As can be seen in Fig. 20(a), the core of the perturbed breather emits a backwards traveling wave. This corresponds to a minimum in the translational velocity V_2 as can be seen in Fig. 20(b). Once this offshoot wave travels around the chain of particles and strikes the core, a secondary wave is emitted. This additional wave travels around the chain and its collision with the core is associated with a maximum in V_2 as can be seen in Fig. 20(b). As more and more waves are emitted, the time between successive extrema decreases due to more frequent collisions. Consequently, the oscillation of V_2 becomes more and more pronounced. Nevertheless, this phenomenology reflects the instability manifestation and explains the progressive decrease of the energy harbored within the breather and the corresponding increase of energy redistributed throughout the

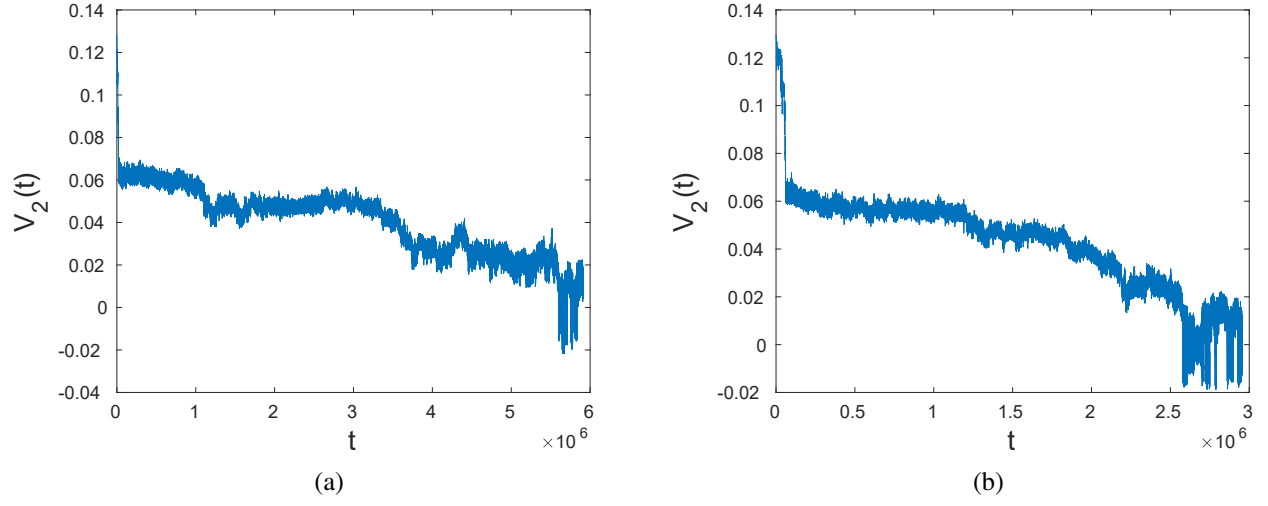


Figure 19: Time evolution of the translational velocity V_2 for the moving breather with largest real Floquet multiplier $\mu = 1.0989$ at (a) $\epsilon = -0.01$; (b) $\epsilon = 0.01$. Here $V_1 = 1/3$, $\omega = 2.424$ and $N = 60$. After an initial transient resulting from the instability manifestation, the breather can be seen to incur a very slow velocity decrease over the long time evolution.

lattice.

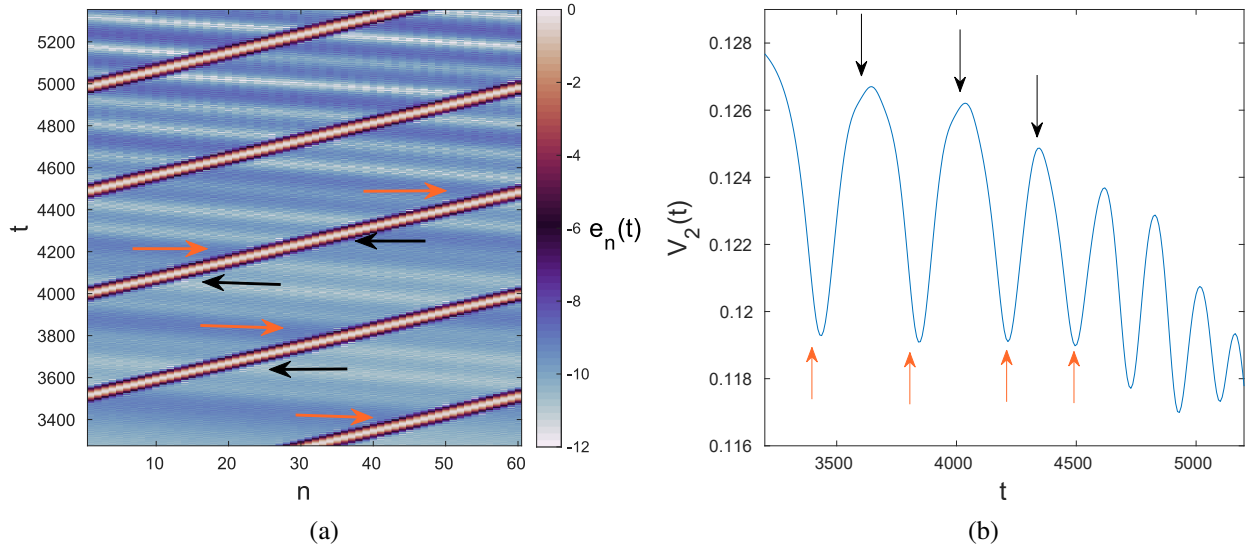


Figure 20: (a) Space-time evolution of the site energy $e_n(t)$ and (b) time evolution of the velocity V_2 near the start of the simulation with $\epsilon = 0.01$. The arrows pointing left and right in (a) correspond to the arrows pointing up and down, respectively, in (b). Here $V_1 = 1/3$, $\omega = 2.424$ and $N = 60$.

3.5 Conclusions

In this chapter we have revisited the topic of the identification, stability classification and dynamical instability manifestation of discrete breathers in the well-known β -FPU lattice. Our exploration has enabled a number of insights into this problem. In particular, we developed a numerical procedure of continuation along a sequence of rational values of the period-wise velocity that allows for the examination of different breather families traversing r sites of the lattice over s multiples of the breather period. The continuation of the relevant waves over the frequency of the breather revealed an intriguing resonance structure, as well as the multivalued nature of the corresponding energy-vs-frequency dependence, enabling the identification of multiple breather waveforms for the same frequency. The resonance structure was elucidated quantitatively for different integer harmonics of frequencies around the breather in comparison with ones of the continuous spectrum, following the work of [78]. The specific harmonics leading to the observed resonances were explicitly identified. At the stability level, the Floquet multipliers of the different branches involved in the resonances were discussed, including also their potential collisions and bifurcations in the complex plane. We remark that in contrast to stationary breathers [69], the emergence of an exponential instability in this case was not associated with the change in the monotonicity of the energy as a function of frequency. Finally, long-time simulations of the dynamical evolution were performed using a symplectic method in order to reveal the manifestation of the relevant instabilities (via the emission of and collision with offshoot waves) and their net result in decelerating and eventually stopping the initially moving breather state.

Naturally, while this study has provided new insights into the dynamics of moving breathers, it has also raised some questions that require further consideration. For instance, among the interesting technical questions that arose were the specific bifurcation structure of the associated periodic orbits in the vicinity of the highly nonlinear resonances that we explored. Another related aspect concerned the fact that we could enumerate all positive and negative resonances in sequence, in connection with the analytical condition of (29) but for a single one. It is also interesting to investigate whether the results obtained in this work extend to Klein-Gordon lattices.

In addition, there exist larger scale questions for future studies. For instance, it would be interesting to explore how the resonance structure and nonlinear state continuation would manifest themselves in higher-dimensional models. In the latter, the issue of transverse (modulational along a stripe or a ring) stability of the relevant waveforms would need to be considered as well. Another aspect

of consideration that at the moment eludes a systematic mathematical formulation is the existence of traveling waveforms with genuinely real (rather than rational) period-wise velocity. Such questions are of substantial interest for potential future investigations.

4.0 Discrete breathers in a mechanical metamaterial

In this chapter we consider a discrete system that models a flexible mechanical metamaterial experimentally realized in [96]. The system consists of a chain of pairs of rigid cross-like units (made from LEGO pieces in [96]) that are connected by flexible hinges. Using the analysis of the linear band structure of the model, we determine the parameter regimes in which this system may possess discrete breather solutions with frequencies inside the gap between optical and acoustic dispersion bands. Setting the parameter values in these regimes, we compute exact (up to a prescribed numerical tolerance) solutions of this type, explore their properties and conduct linear stability analysis. We find that with an appropriate parameter tuning the system exhibits a complex bifurcation structure of discrete breathers with multiple branches that include stability change via period-doubling and symmetry-breaking bifurcations, in addition to saddle-center and Hamiltonian Hopf bifurcations. The stability analysis is complemented by direct numerical simulations that point to effective stability of some of the obtained solutions.

The chapter is organized as follows. In Sec. 4.1 we introduce the discrete model and formulate the problem. Analysis of the dispersion relation for the linearized system is presented in Sec. 4.2. In Sec. 4.3 we discuss a solution branch bifurcating from the edge of the optical mode for the parameter values in [96] and exhibiting period-doubling bifurcations. In Sec. 4.4 we consider another set of parameters and describe the complex bifurcation diagrams involving branches either bifurcating from or existing near the edges of optical and acoustic bands. Concluding remarks can be found in Sec. 4.5.

4.1 Problem formulation

Motivated by experimental and theoretical investigations in [96], we consider a chain that consists of $2 \times N$ cross-type rigid units of mass m and moment of inertia J connected by thin flexible hinges, as shown in Fig. 1. The neighboring horizontal hinges are shifted in the vertical direction by $a \tan \phi_0$, where a is the center-to-center horizontal distance between the neighboring units (see the bottom panel of Fig. 1). The hinges are modeled as a combination of three linear springs, with stiffness parameters k_l , k_s and k_θ corresponding to longitudinal stretching, shearing and bending, respectively.

Following [96], we describe the dynamics of the system by two degrees of freedom for n -th vertical pair of rigid units: the longitudinal displacement $u_n(t)$ and the rotation angle $\theta_n(t)$ at time t . Here it is assumed [96] that the two rigid units in each vertical pair have the same displacement and rotate by the same amount but in the opposite directions, with positive direction of rotation defined as shown in the bottom panel of Fig. 1. Introducing dimensionless variables

$$\tilde{u}_n = \frac{u_n}{a}, \quad \tilde{t} = t \sqrt{\frac{k_l}{m}}$$

and parameters

$$\alpha = \frac{a}{2 \cos \phi_0} \sqrt{\frac{m}{J}}, \quad K_s = \frac{k_s}{k_l}, \quad K_\theta = \frac{4k_\theta \cos^2 \phi_0}{k_l a^2},$$

one obtains [96]

$$\begin{aligned} \ddot{u}_n &= u_{n+1} - 2u_n + u_{n-1} - \frac{\cos(\theta_{n+1} + \phi_0) - \cos(\theta_{n-1} + \phi_0)}{2 \cos(\phi_0)} \\ \frac{1}{\alpha^2} \ddot{\theta}_n &= -K_\theta(\theta_{n+1} + 4\theta_n + \theta_{n-1}) + K_s \cos(\theta_n + \phi_0) \left(\sin(\theta_{n+1} + \phi_0) + \sin(\theta_{n-1} + \phi_0) \right. \\ &\quad \left. - 2 \sin(\theta_n + \phi_0) \right) - \sin(\theta_n + \phi_0) \left(2 \cos(\phi_0)(u_{n+1} - u_{n-1}) + 4 \cos(\phi_0) - \cos(\theta_{n+1} + \phi_0) \right. \\ &\quad \left. - 2 \cos(\theta_n + \phi_0) - \cos(\theta_{n-1} + \phi_0) \right), \end{aligned} \quad (30)$$

where we dropped the tildes in the rescaled displacement and time variables, and double dot denotes second time derivative. The total energy of the system is [96]

$$H = \sum_{n=1}^N \left[(\Delta_n^l)^2 + K_s (\Delta_n^s)^2 + \frac{K_\theta}{8 \cos^2(\phi_0)} (2(\delta_n^h)^2 + (\delta_n^v)^2) + \dot{u}_n^2 + \frac{1}{4\alpha^2 \cos^2(\phi_0)} \dot{\theta}_n^2 \right], \quad (31)$$

where

$$\begin{aligned} \delta_n^h &= \theta_{n+1} + \theta_n, \quad \delta_n^v = 2\theta_n, \\ \Delta_n^l &= u_{n+1} - u_n + \frac{1}{2 \cos(\phi_0)} [2 \cos(\phi_0) - \cos(\phi_0 + \theta_n) - \cos(\phi_0 + \theta_{n+1})], \\ \Delta_n^s &= \frac{1}{2 \cos(\phi_0)} [\sin(\phi_0 + \theta_{n+1}) - \sin(\phi_0 + \theta_n)] \end{aligned}$$

characterize the deformation associated with horizontal $(\delta_n^h, \Delta_n^l, \Delta_n^s)$ and vertical (δ_n^v) hinges.

We consider discrete breather (DB) solutions of (30). These are time-periodic nonlinear waves with frequency ω and the corresponding period $T = 2\pi/\omega$,

$$u_n(t+T) = u_n(t), \quad \theta_n(t+T) = \theta_n(t) \quad (32)$$

that are spatially localized in terms of strain

$$w_n(t) = u_{n+1}(t) - u_n(t) \quad (33)$$

and angle $\theta_n(t)$ variables.

4.2 Dispersion Relation

To obtain conditions for existence of DB solutions bifurcating from the linear modes, we need to study the linear spectrum of the problem first. To that effect, we linearize (30) around the undeformed configuration. This yields

$$\begin{aligned} \ddot{u}_n &= u_{n+1} - 2u_n + u_{n-1} + \frac{1}{2} \tan \phi_0 (\theta_{n+1} - \theta_{n-1}) \\ \frac{1}{\alpha^2} \ddot{\theta}_n &= (K_s \cos^2 \phi_0 - \sin^2 \phi_0 - K_\theta) (\theta_{n+1} + \theta_{n-1}) \\ &\quad - 2(K_s \cos^2 \phi_0 + \sin^2 \phi_0 + 2K_\theta) \theta_n - \sin(2\phi_0) (u_{n+1} - u_{n-1}). \end{aligned} \quad (34)$$

Considering plane-wave solutions $u_n(t) = U e^{i(kn - \omega t)}$, $\theta_j(t) = \Theta e^{i(kn - \omega t)}$ of (34) in the limit of an infinite chain ($N \rightarrow \infty$), we obtain the following solvability condition:

$$\begin{aligned} \left(\omega^2 - 4 \sin^2 \frac{k}{2} \right) \left[\frac{\omega^2}{\alpha^2} - 2(K_\theta - K_s \cos^2 \phi_0 + \sin^2 \phi_0) \cos(k) - 2(2K_\theta + K_s \cos^2 \phi_0 + \sin^2 \phi_0) \right] \\ - 2 \tan(\phi_0) \sin(2\phi_0) \sin^2(k) = 0, \end{aligned}$$

which yields explicit (but cumbersome) expressions for the acoustic, $\omega_-(k)$, and optical, $\omega_+(k)$, branches of the dispersion relation between the wave number k and the frequency ω . The two branches satisfy

$$\omega_-(0) = 0, \quad \omega_+(0) = \alpha \sqrt{2(3K_\theta + 2 \sin^2 \phi_0)} > 0. \quad (35)$$

We now examine the evolution of the dispersion relation when the parameters α , K_s and K_θ are fixed, while ϕ_0 is varied. Due to 2π -periodicity and even symmetry about $k = \pi$, it suffices to consider wave numbers k in $[0, \pi]$. In what follows, we consider two sets of parameters α , K_s and K_θ . In the first representative example, we set $\alpha = 1.8$, $K_s = 0.02$, and $K_\theta = 1.5 \times 10^{-4}$ from [96]. In the second case we keep the same value of K_s and set $\alpha = 5$ and $K_\theta = 0.01$. In both cases

$$\alpha^2 (K_\theta + 2K_s \cos^2 \phi_0) < 2 \quad (36)$$

is satisfied for all ϕ_0 , and we thus have

$$\omega_-(\pi) = \alpha \sqrt{2(K_\theta + 2K_s \cos^2 \phi_0)} < \omega_+(\pi) = 2. \quad (37)$$

Furthermore, one can show that for these parameter values the acoustic branch $\omega_-(k)$ has the maximum value at $k = \pi$ given in (37) for all ϕ_0 . Meanwhile, as shown in Fig. 21(a), the optical branch $\omega_+(k)$ has a maximum at $k = \pi$ and a minimum at $k = 0$ for $0 \leq \phi_0 < \phi'_0$, where

$$\phi'_0 = \arccos \left(\sqrt{\frac{1 + \frac{K_\theta}{2} - \frac{1}{\alpha^2}}{1 - K_s}} \right) \quad (38)$$

is obtained by setting $\omega''_+(\pi) = 0$ at $\phi_0 = \phi'_0$ and using (36). The corresponding inflection point at $k = \pi$ is shown in Fig. 21(b). For $\phi'_0 < \phi_0 < \phi''_0$, where

$$\phi''_0 = \arcsin \left(\sqrt{\frac{1}{\alpha^2} - \frac{3}{2}K_\theta} \right), \quad (39)$$

$k = \pi$ becomes a local minimum, and $\omega_+(k)$ reaches its maximum at $k = k_{max}$ in $(0, \pi)$ and a global minimum at $k = 0$ (see Fig. 21(c)). At $\phi_0 = \phi''_0$, the case shown in Fig. 21(d), we have $\omega_+(0) = \omega_+(\pi) = 2$, which together with the second expression in (35) yields (39). For $\phi_0 > \phi''_0$, the optical branch has a global minimum $\omega_+(\pi) = 2$ at $k = \pi$. As shown in Fig. 21(e), it has a local minimum at $k = 0$ and the maximum at $k = k_{max}$ in $(0, \pi)$ until ϕ_0 reaches the value

$$\begin{aligned} \phi'''_0 = \arccos \left(\frac{1}{2\alpha} \left[\left(-2 + \alpha^2(K_s(3K_\theta + 2) + 5K_\theta + 4) \right. \right. \right. \\ \left. \left. \left. - \sqrt{\alpha^4(K_s(3K_\theta + 2) + K_\theta)^2 - 4\alpha^2(K_s(3K_\theta - 2) + 5K_\theta + 4)} \right) / (K_s + 1) \right]^{1/2} \right), \end{aligned} \quad (40)$$

where $k = 0$ becomes an inflection point ($\omega''_+(0) = 0$); see Fig. 21(f). For $\phi_0 > \phi'''_0$ the optical branch is inverted and has the maximum value at $k = 0$ and the minimum value at $k = \pi$, as shown in Fig. 21(g). We obtain $\phi'_0 = 0.5736$, $\phi''_0 = 0.5888$ and $\phi'''_0 = 0.6032$ for the parameters $\alpha = 1.8$, $K_s = 0.02$, $K_\theta = 1.5 \times 10^{-4}$. In the case $\alpha = 5$, $K_s = 0.02$, $K_\theta = 0.01$, the evolution of the optical branch is similar to Fig. 21 but the critical values are $\phi'_0 = 0.1240$, $\phi''_0 = 0.1588$ and $\phi'''_0 = 0.1959$.

Let k_{min} denote the wave number where the optical branch $\omega_+(k)$ reaches its minimum value. From the above discussion it follows that $k_{min} = 0$ for $0 \leq \phi_0 \leq \phi''_0$, with the minimum value

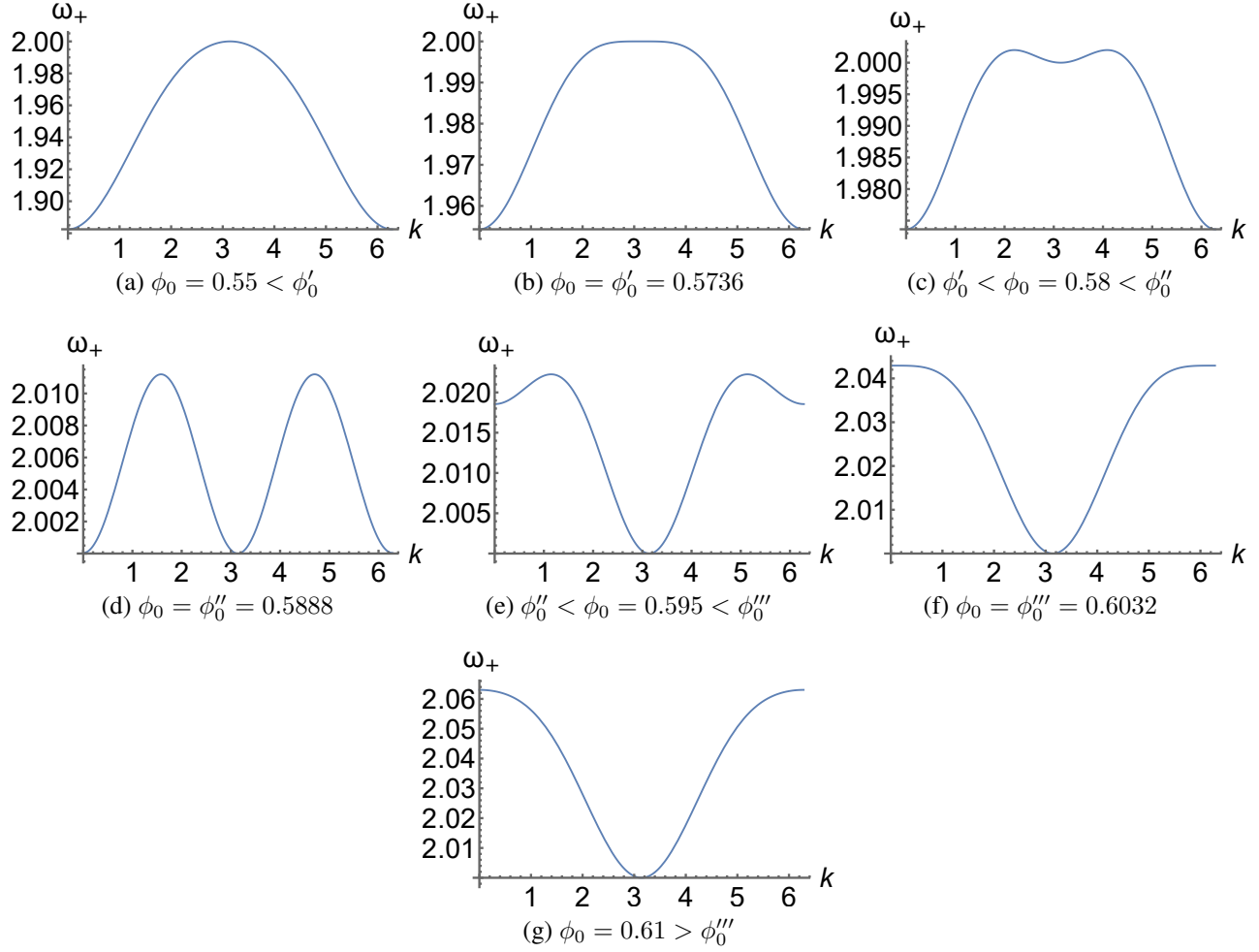


Figure 21: Optical branch of the dispersion relation at different values of ϕ_0 . For each panel the corresponding value of ϕ_0 is given; see also the discussion in the text. Here $\alpha = 1.8$, $K_s = 0.02$, $K_\theta = 1.5 \times 10^{-4}$.

$\omega_+(0) = \alpha(6K_\theta + 4\sin^2 \phi_0)^{1/2}$, and $k_{min} = \pi$ for $\phi_0 > \phi''_0$, with the minimum value $\omega_+(\pi) = 2$.

Recalling that the acoustic branch has a maximum at $k = \pi$, we find that when

$$G = \omega_+(k_{min}) - \omega_-(\pi) > 0, \quad (41)$$

there is a *band gap* between the two branches. See Fig. 22 for examples of such a gap. A DB solution with frequency ω inside the gap, i.e., $\omega_-(\pi) < \omega < \omega_+(k_{min})$, may exist provided that

$$S = \omega_+(k_{min}) - \frac{1}{2}\omega_+(k_{max}) > 0 \quad (42)$$

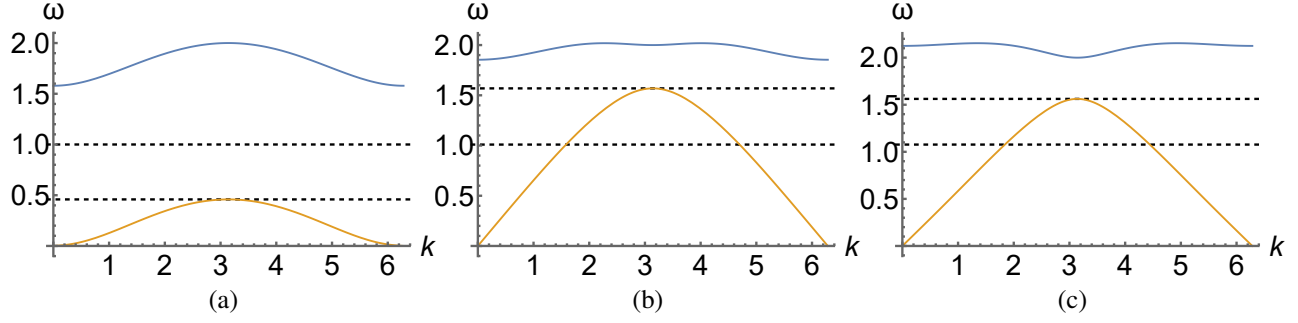


Figure 22: Optical (blue) and acoustic (orange) branches for (a) $\phi_0 = 26\pi/180 \approx 0.4538$, $\alpha = 1.8$, $K_s = 0.02$, $K_\theta = 1.5 \times 10^{-4}$; (b) $\phi_0 = 8\pi/180 \approx 0.1396$, $\alpha = 5$, $K_s = 0.02$, $K_\theta = 0.01$; (c) $\phi_0 = 10\pi/180 \approx 0.1745$, $\alpha = 5$, $K_s = 0.02$, $K_\theta = 0.01$. The horizontal lines indicate the maximum $\omega_-(\pi)$ of the acoustic branch and $\omega_+(k_{max})/2$, half of the maximum of the optical branch. When the optical branch is above $\omega_-(\pi)$, (41) holds, and when it is above $\omega_+(k_{max})/2$, (42) holds.

holds in addition to (41) and $\omega > \omega_+(k_{max})/2$. Here k_{max} is the wavenumber where the optical branch $\omega_+(k)$ reaches its maximum value. The fact that ω does not coincide with either optical or acoustic values for any wave number means that the breather is not in resonance with any linear modes, while the condition (42) eliminates the second harmonic resonances by ensuring that $2\omega > \omega_+(k)$ for all wave numbers. This enables both the spatial localization (due to its presence in the bandgap) and the non-resonance of the breather, as discussed, e.g., in [120].

Fig. 23 shows G and S defined in (41) and (42), respectively, as functions of ϕ_0 for the first parameter set. Both functions have a corner at $\phi_0 = \phi_0''$ where k_{min} changes from 0 to π . Noting that G changes sign from negative to positive for $\phi_0 < \phi_0''$, when $k_{min} = 0$, we set

$$G = \omega_+(0) - \omega_-(\pi) = \alpha \left(\sqrt{6K_\theta + 4\sin^2(\phi_0)} - \sqrt{2K_\theta + 4K_s\cos^2(\phi_0)} \right) = 0$$

to find the critical angle

$$\phi_0^* = \arccos \sqrt{\frac{1+K_\theta}{1+K_s}} \quad (43)$$

above which (41) holds. The function S in Fig. 23(b) also changes sign for $\phi_0 < \phi_0'$, where $k_{min} = 0$ and $k_{max} = \pi$, so that

$$S = \omega_+(0) - \frac{1}{2}\omega_+(\pi) = \alpha \sqrt{6K_\theta + 4\sin^2(\phi_0)} - 1 = 0$$

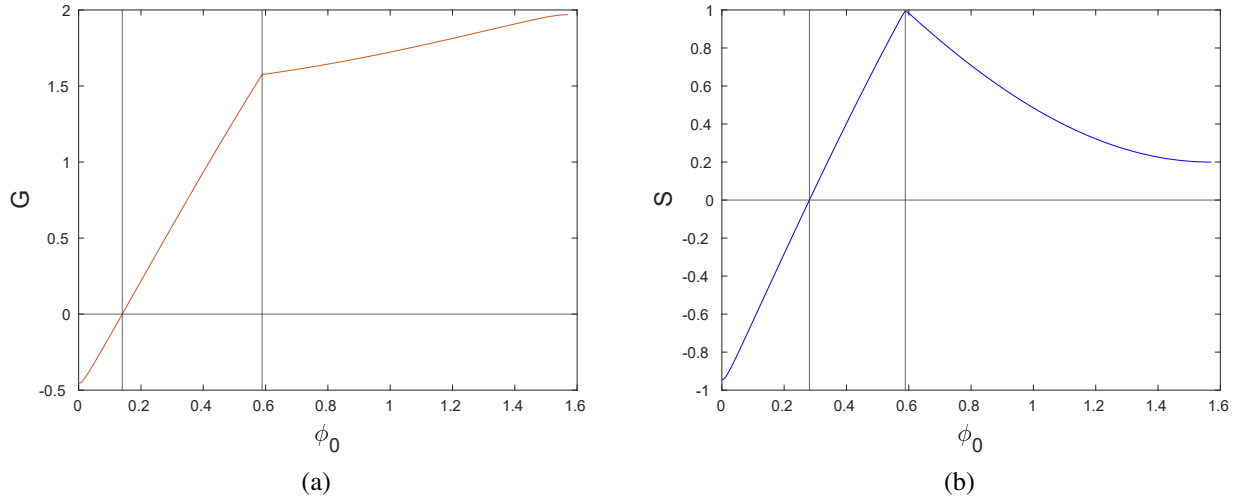


Figure 23: (a) G defined in (41) as a function of ϕ_0 . The horizontal line is $G = 0$, and the two vertical lines indicate $\phi_0 = \phi_0^* = 0.1400$ and $\phi_0 = \phi_0'' = 0.5888$. (b) S defined in (42) as a function of ϕ_0 . The horizontal line is $S = 0$ and the two vertical lines indicate $\phi_0 = \phi_0^{**} = 0.2811$ and $\phi_0 = \phi_0'' = 0.5888$. Here $\alpha = 1.8$, $K_s = 0.02$, $K_\theta = 1.5 \times 10^{-4}$.

at

$$\phi_0^{**} = \arcsin \left(\sqrt{\frac{1}{4\alpha^2} - \frac{3}{2}K_\theta} \right), \quad (44)$$

and hence (42) holds for $\phi_0 > \phi_0^{**}$. We find that $\phi_0^* = 0.1400$ and $\phi_0^{**} = 0.2811$ in this case. Thus for $\phi_0 > 0.2811$, both (41) and (42) hold, and DB solutions may exist with frequencies ω in the interval $(\omega_+(k_{\max})/2, \omega_+(k_{\min}))$; otherwise, first or second resonances set in. The example at $\phi_0 = 26\pi/180 \approx 0.4538$, where (41) and (42) hold for $1 < \omega < 1.57906$, is shown in Fig. 22(a). As shown in Fig. 23(b), the frequency gap increases until $\phi_0'' = 0.5888$ and then starts decreasing. Note that for $\phi_0 < \phi_0''$, DB solutions bifurcating from the optical band emerge from $k = 0$ mode, while for ϕ_0 above this threshold the breathers bifurcate from the $k = \pi$ mode.

The functions $G(\phi_0)$ and $S(\phi_0)$ for the second parameter set are shown in Fig. 24. Recall that in this case (38), (39) and (40) yield $\phi_0' = 0.1240$, $\phi_0'' = 0.1588$ and $\phi_0''' = 0.1959$. One can see that (41) holds ($F(\phi_0) > 0$) for $\phi_0 > \phi_0^*$, where $\phi_0^* = 0.0992$ is found from (43). Meanwhile, $S(\phi_0)$ is positive for $0 \leq \phi_0 < \phi_0^{***}$. To find this value, we observe that it is above ϕ_0''' , which means that $k_{\min} = \pi$ and $k_{\max} = 0$ in (42). Thus,

$$S = 2 - \frac{1}{2}\alpha\sqrt{6K_\theta + 4\sin^2(\phi_0)} = 0$$

must hold at $\phi_0 = \phi_0^{***}$, which yields

$$\phi_0^{***} = \arcsin \left(\sqrt{\frac{4}{\alpha^2} - \frac{3}{2}K_\theta} \right). \quad (45)$$

We obtain $\phi_0^{***} = 0.3906$ for the second parameter set. Thus, in this case (41) and (42) both hold when $0.0992 < \phi_0 < 0.3906$. Examples of dispersion relations with band gaps for this parameter regime are shown in panels (b) and (c) of Fig. 22. Note that in both cases the maximum of the acoustic branch lies above the half of the maximum of the optical one, and hence the frequency range where DB solutions may exist includes the entire gap between the two bands. This is in contrast to the example shown in Fig. 22(a) for the first parameter set, where the breather frequency must exceed $\omega_+(\pi)/2 = 1$.

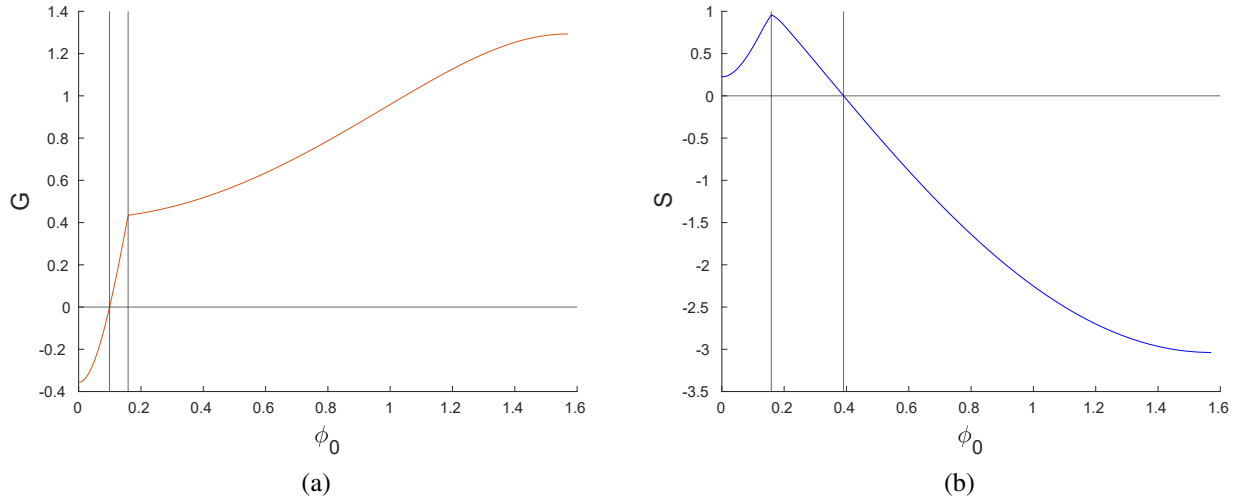


Figure 24: (a) G defined in (41) as a function of ϕ_0 . The horizontal line is $G = 0$ and the two vertical lines indicate $\phi_0 = \phi_0^* = 0.0992$ and $\phi_0 = \phi_0'' = 0.1588$. (b) S defined in (42) as a function of ϕ_0 . The horizontal line is $S = 0$ and the two vertical lines indicate $\phi_0 = \phi_0'' = 0.1588$ and $\phi_0 = \phi_0^{***} = 0.3906$. Here $\alpha = 5$, $K_s = 0.02$, $K_\theta = 0.01$.

4.3 Period-doubling bifurcation

We first discuss DB solutions bifurcating from the optical $k = 0$ mode for $\phi_0 < \phi_0''$ for the parameters considered in [96] and associated with the experimental implementation of the metamaterial in that work: $\alpha = 1.8$, $K_s = 0.02$, $K_\theta = 1.5 \times 10^{-4}$. We set $\phi_0 = 26\pi/180 \approx 0.4538$, which enables

existence of DB solutions with frequency ω in $(1, 1.57906)$. The corresponding dispersion relation is shown in Fig. 22(a).

To obtain the breathers with frequency ω and corresponding period $T = 2\pi/\omega$, we consider a chain of $N = 200$ elements and solve iteratively using Newton's method the following equations:

$$\begin{pmatrix} \mathbf{u}(T) - \mathbf{u}(0) \\ \dot{\mathbf{u}}(T) - \dot{\mathbf{u}}(0) \\ \boldsymbol{\theta}(T) - \boldsymbol{\theta}(0) \\ \dot{\boldsymbol{\theta}}(T) - \dot{\boldsymbol{\theta}}(0) \end{pmatrix} = \mathbf{0},$$

where the vector functions $\mathbf{u}(t)$, $\dot{\mathbf{u}}(t)$, $\boldsymbol{\theta}(t)$, and $\dot{\boldsymbol{\theta}}(t)$ have the components $u_n(t)$, $\dot{u}_n(t)$, $\theta_n(t)$, and $\dot{\theta}_n(t)$, $n = 1, \dots, N$, respectively. We perform numerical continuation in the frequency ω , starting with $\omega = 1.57$, just below the edge of the optical band at $k = 0$. The initial guess is of the form

$$u_n = \varepsilon_u \tanh[\delta(n - N/2)], \quad \theta_n = \varepsilon_\theta \operatorname{sech}[\delta(n - N/2)], \quad (46)$$

where ε_u , ε_θ and δ are small. The dynamical evolution of Eq. (30) (over the prescribed period T) is performed using the symplectic fourth-order Runge-Kutta-Nyström algorithm [82] with free-end boundary conditions.

To study the linear stability of the obtained solutions, we use Floquet analysis. Setting $u_n(t) = \hat{u}_n(t) + \epsilon v_n(t)$ and $\theta_n(t) = \hat{\theta}_n(t) + \epsilon \gamma_n(t)$ in (30), where $\hat{u}_n(t)$ and $\hat{\theta}_n(t)$ comprise the DB solutions, and considering $O(\epsilon)$ terms, we obtain the linearized system

$$\begin{aligned} \ddot{v}_n &= v_{n+1} + v_{n-1} - 2v_n - \left[\frac{-\sin(\hat{\theta}_{n+1} + \phi_0)\gamma_{n+1} + \sin(\hat{\theta}_{n-1} + \phi_0)\gamma_{n-1}}{2\cos(\phi_0)} \right] \\ \frac{1}{\alpha^2} \ddot{\gamma}_n &= -K_\theta(\gamma_{n+1} + 4\gamma_n + \gamma_{n-1}) + K_s[\cos(\hat{\theta}_n + \phi_0)\cos(\hat{\theta}_{n+1} + \phi_0)\gamma_{n+1} \\ &\quad - \sin(\hat{\theta}_n + \phi_0)\sin(\hat{\theta}_{n+1} + \phi_0)\gamma_n + \cos(\hat{\theta}_n + \phi_0)\cos(\hat{\theta}_{n-1} + \phi_0)\gamma_{n-1} \\ &\quad - \sin(\hat{\theta}_n + \phi_0)\sin(\hat{\theta}_{n-1} + \phi_0)\gamma_n - 2(\cos^2(\hat{\theta}_n + \phi_0) - \sin^2(\hat{\theta}_n + \phi_0))\gamma_n] \\ &\quad - [2\sin(\hat{\theta}_n + \phi_0)\cos(\phi_0)(v_{n+1} - v_{n-1}) + 2\cos(\hat{\theta}_n + \phi_0)\cos(\phi_0)(\hat{u}_{n+1} - \hat{u}_{n-1})\gamma_n \\ &\quad + 4\cos(\hat{\theta}_n + \phi_0)\cos(\phi_0)\gamma_n - (\cos(\hat{\theta}_n + \phi_0)\cos(\hat{\theta}_{n+1} + \phi_0)\gamma_n \\ &\quad - \sin(\hat{\theta}_n + \phi_0)\sin(\hat{\theta}_{n+1} + \phi_0)\gamma_{n+1}) - 2(\cos^2(\hat{\theta}_n + \phi_0) - \sin^2(\hat{\theta}_n + \phi_0))\gamma_n \\ &\quad - (\cos(\hat{\theta}_n + \phi_0)\cos(\hat{\theta}_{n-1} + \phi_0)\gamma_n - \sin(\hat{\theta}_n + \phi_0)\sin(\hat{\theta}_{n-1} + \phi_0)\gamma_{n-1})], \end{aligned}$$

which is used to compute the monodromy matrix \mathcal{F} defined by

$$\begin{pmatrix} \mathbf{v}(T) \\ \dot{\mathbf{v}}(T) \\ \gamma(T) \\ \dot{\gamma}(T) \end{pmatrix} = \mathcal{F} \begin{pmatrix} \mathbf{v}(0) \\ \dot{\mathbf{v}}(0) \\ \gamma(0) \\ \dot{\gamma}(0) \end{pmatrix},$$

where the vector functions $\mathbf{v}(t)$, $\dot{\mathbf{v}}(t)$, $\gamma(t)$, and $\dot{\gamma}(t)$ have the components $v_n(t)$, $\dot{v}_n(t)$, $\gamma_n(t)$, and $\dot{\gamma}_n(t)$, $n = 1, \dots, N$, respectively. The Floquet multipliers μ are the eigenvalues of the matrix \mathcal{F} . The existence of a Floquet multiplier μ satisfying $|\mu| > 1$ indicates the presence of instability. When the relevant instability-inducing multiplier is real, we refer to the instability as *exponential*, given the exponential nature of the associated growth. When such real multipliers arise, they come in pairs $(\mu, 1/\mu)$ (one of which is outside, while the other is inside the unit circle). In the case of a complex multiplier quartet $(\mu, 1/\mu, \bar{\mu}, 1/\bar{\mu})$ with $|\mu| > 1$, the instability is referred to as *oscillatory*, given that oscillations accompany the exponential growth due to the imaginary part of the associated multipliers. The fact that the multipliers come in real pairs or complex quartets is a generic by-product of the Hamiltonian nature of the underlying lattice dynamical system.

Fig. 25(a) shows the energy H of the breathers bifurcating from the $k = 0$ mode as a function of the frequency ω . As we will see below, using this pair of independent and dependent variables to illustrate our bifurcation diagrams allows us to connect the change in monotonicity of the energy-frequency curve with a potential stability change [113]. As illustrated in the insets, the amplitude of both the strain (33) and angle variables increases as the frequency is decreased away from the edge of the optical band, i.e., as the strength of the nonlinear contribution increases. The maximum modulus of the Floquet multipliers computed for this solution branch is shown by the blue curve in Fig. 25(c). One can see that it exceeds unity and rapidly increases near the end of the continuation. As illustrated in the inset (see also panels (a) and (b) of Fig. 26, which show the Floquet multipliers at the beginning and the end of the continuation, respectively), this is due to the emergence of a pair $(\mu, 1/\mu)$ of real Floquet multipliers from $\mu = -1$ at $\omega = 1.05155$. One of these has modulus greater than one and hence leads to an exponential instability, at the point d in Fig. 25(b), which corresponds to a *period-doubling bifurcation* [50]. A second pair of real Floquet multipliers emerges from $\mu = -1$ at $\omega = 1.05006$, leading to another exponential instability mode (not further explored). As the frequency is decreased, these multipliers first move away from the unit circle along the real line and then start

moving back toward it, eventually colliding at $\mu = -1$ at $\omega = 1.0499$, which corresponds to the point e in Fig. 25(b) and is associated with another period-doubling bifurcation.

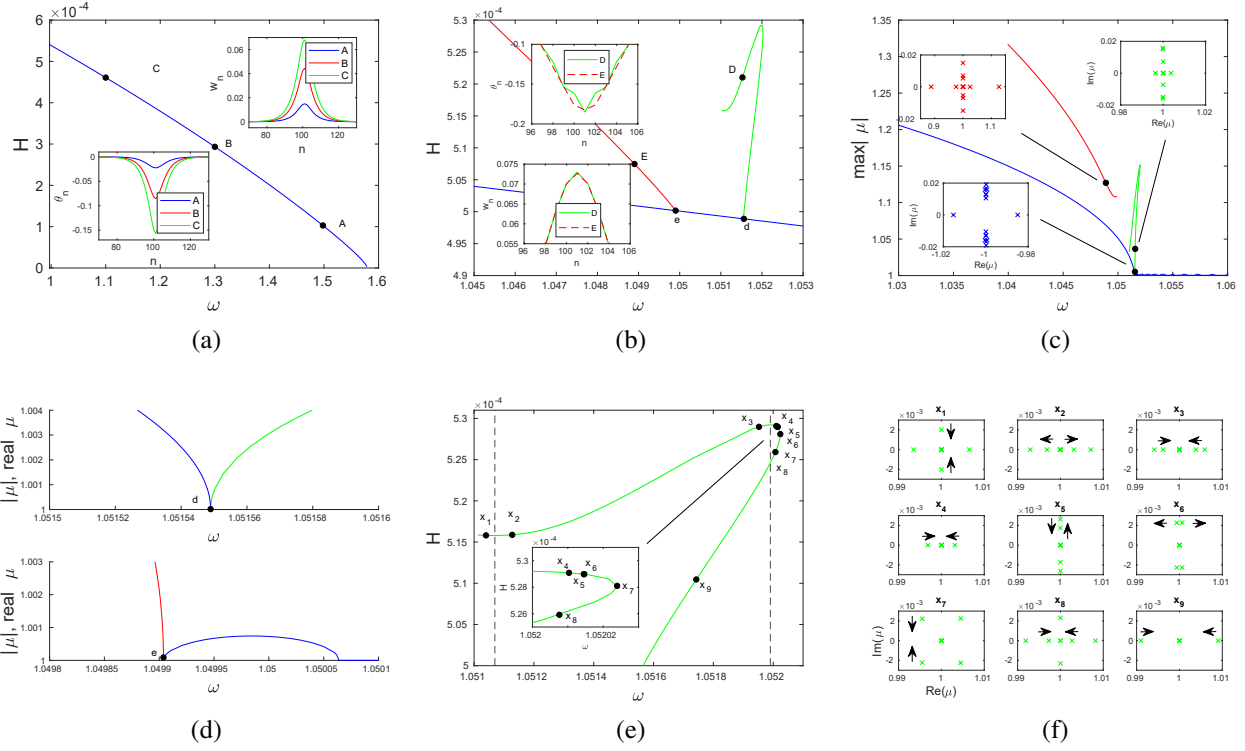


Figure 25: (a) Energy H as a function of frequency ω . The two insets show the strain (33) and angle variables at the points A , B , and C along the solution curve. (b) $H(\omega)$ for the single-period (blue curve) and double-period (red and green curves) solution branches at twice their frequency. The bifurcation points are marked by d and e . The two insets show the strain and angle variables at the points D and E along the double-period solution curves. (c) Maximum modulus $|\mu|$ of Floquet multipliers versus frequency ω along the single-period (blue) and double-period (red and green) solution branches. The insets show the corresponding Floquet multipliers near the unit circle. While the double-period solution along the red curve coincides with the single period solution (blue curve) at the bifurcation point e , the Floquet multipliers for the double-period solution are squares of those for the single-period one, resulting in the gap between the blue and red curves. (d) Upper panel: largest modulus $|\mu|$ of the real Floquet multipliers as a function of frequency ω along the blue single-period and green double-period solution curves near the bifurcation point d . Lower panel: second largest modulus $|\mu|$ of the real Floquet multipliers as a function of ω along the blue single-period and red double-period solution curves near the bifurcation point e . Note that these real Floquet multipliers are negative for the blue curve and positive for the red and green curves. (e) Enlarged view of $H(\omega)$ along the green double-period solution curve. The dashed vertical lines indicate the local minimum (left) and maximum (right). The points x_1, \dots, x_9 correspond to the Floquet multiplier panels shown in (f). The inset shows an enlarged view around the cluster of points. (f) The Floquet multipliers near $\mu = 1$ for the points marked in the panel (e). The arrows indicate the motion of the Floquet multipliers. Here and in the remainder of this section we have $\alpha = 1.8$, $K_s = 0.02$, $K_\theta = 1.5 \times 10^{-4}$, $N = 200$, and $\phi_0 = 26\pi/180$.

To compute the double-period solutions that arise as a result of the bifurcations at the points d and e along the single-period solution branch, we used the same iterative procedure as discussed above with the initial guess consisting of a single-period solution with twice the frequency perturbed along the corresponding unstable mode. Solutions along the bifurcating branches were then obtained using

parameter continuation in frequency or energy. The resulting energy as a function of frequency for the double-period solutions (red and green curves) is shown in Fig. 25(b) for each case together with the single-period solution branch (blue curve) discussed above. The double-period solution curves are plotted at twice their actual frequency in order to facilitate the comparison with the single-period solution curve. Insets in Fig. 25(b) show examples of the symmetric breather solutions along the different double-period solution curves. As the insets of Fig. 25(c) reveal, the Floquet spectra of the double-period and single-period solution branches are markedly different. While the single-period solutions, as noted above, are characterized by an exponential period-doubling instability associated with a Floquet multiplier $\mu < -1$ for frequencies below the value at the bifurcation point d , the double-period branches exhibit an exponential instability associated with a Floquet multiplier satisfying $\mu > 1$. As the bifurcation points are approached, the corresponding pairs of real multipliers collide at $\mu = -1$ for the parent single-period branch and at $\mu = 1$ for the bifurcating branches.

To examine the nature of these bifurcations further, we plot in the top panel of Fig. 25(d) the largest modulus of real Floquet multipliers μ as a function of ω along the green and blue curves near the bifurcation point d . One can see that at the period-doubling bifurcation point d the single-period branch develops an exponential instability associated with a Floquet multiplier $\mu < -1$ via a subcritical pitchfork bifurcation of the double-period branch, which has a pair of real multipliers $(\mu, 1/\mu)$ with $\mu > 1$. In the bottom panel of Fig. 25(d), we show the second largest modulus of the real Floquet multipliers near the bifurcation point e , where the second pair of real multipliers emerges near $\mu = -1$ for the single-period branch and near $\mu = 1$ for the bifurcating red branch. Due to the presence of the first pair of real multipliers, all solutions are unstable near the bifurcation point e , as indicated in Fig. 25(c).

Note that the upper branch of the multivalued energy-frequency function corresponding to the unstable green double-period solution curve bifurcating from the point d has a local minimum and a local maximum, marked by the dashed vertical lines in Fig. 25(e). As illustrated in the first four panels in Fig. 25(f), these extrema are associated with a change of multiplicity of the Floquet multiplier at $\mu = 1$ along this branch and subsequent emergence or collision of a second pair of real Floquet multipliers. The change in multiplicity of the unit Floquet multiplier when $H'(\omega)$ changes sign is consistent with the energy-based stability criterion proved in [113] for discrete breathers in Fermi-Pasta-Ulam and Klein-Gordon lattices. Note, however, that in this case the change in multiplicity does not lead to a stability change due to the presence of an additional pair of non-unit real multipliers

at these frequency values. As we trace the solution curve toward the point d , this pair collides at $\mu = 1$ on the unit circle at a bifurcation point and subsequently briefly remains on it (see panels 4 and 5 in Fig. 25(f)), while the solutions are still unstable due to the presence of complex multipliers μ satisfying $|\mu| > 1$ (not shown in panel 5). However, as illustrated in panels 7 and 8 in Fig. 25(f), two pairs of real multipliers subsequently emerge on the real axis via collisions of complex conjugate pairs of multipliers. One of the pairs eventually collides on the unit circle at another bifurcation point, leaving a single pair (panel 9), which in turn collides at $\mu = 1$ at the point d .

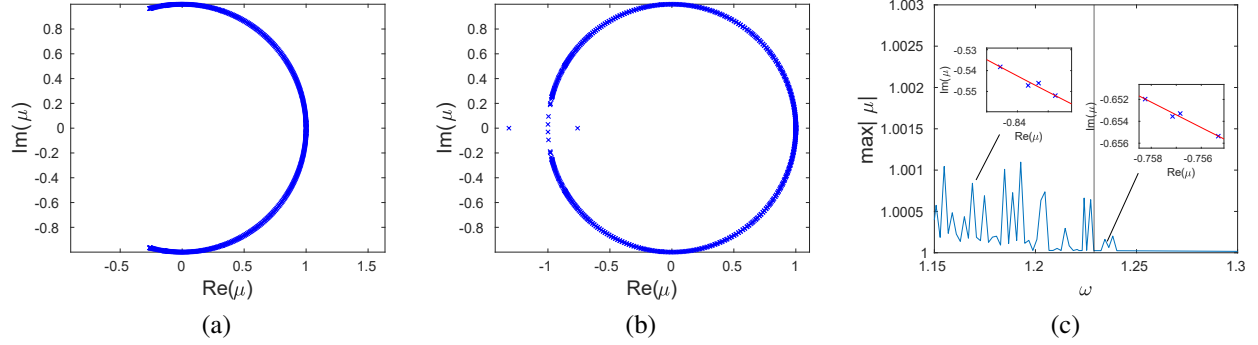


Figure 26: Panels (a) and (b) show Floquet multipliers μ at the start ($\omega = 1.57$, panel (a)) and the end ($\omega = 0.9972$, panel (b)) of the continuation. Panel (c) shows an enlarged view of Fig. 25(b). The vertical line indicates the frequency $\omega = 1.229$, at which the top optical and bottom acoustic arcs shown in Fig. 27 below first intersect (see the text for details). Here $|\mu| > 1$ corresponds to oscillatory instabilities, as shown in the insets, where the red curve is part of the unit circle.

The enlarged view of the Floquet multiplier curve for the single-period solution branch and the insets shown in Fig. 26(c) reveal that the onset of the period-doubling instability is preceded by small-magnitude *oscillatory* instabilities associated with pairs of multipliers colliding on the unit circle and then moving slightly off it in the form of a quartet as discussed above. Note also that the Floquet multipliers μ form an arc on or near the unit circle. Using the linearization (34) of Eq. (30) about the uniform equilibrium state for an infinite chain, one can show [121] that the background state of the breather with period T contributes the Floquet multipliers

$$\mu = e^{\pm i\omega_{\pm}(k)T}, \quad (47)$$

where we recall from Sec. 4.2 that $\omega_+(k)$ and $\omega_-(k)$ are the optical and acoustic branches of the dispersion relation. As we vary k from 0 to π , we obtain arcs of multipliers along the unit circle. Such arcs corresponding to the upper optical ($\omega_+(k)$, red arc) and the bottom acoustic ($-\omega_-(k)$, light blue

arc) bands are depicted in panels (a), (b) and (c) of Fig. 27 for different values of ω (and hence different $T = 2\pi/\omega$ in (47)) along with the numerically computed Floquet multipliers (dark blue crosses) for the obtained DB solutions. There are also symmetric arcs (not shown in the figure) corresponding to the bottom optical ($-\omega_+(k)$) and the upper acoustic ($\omega_-(k)$) bands.

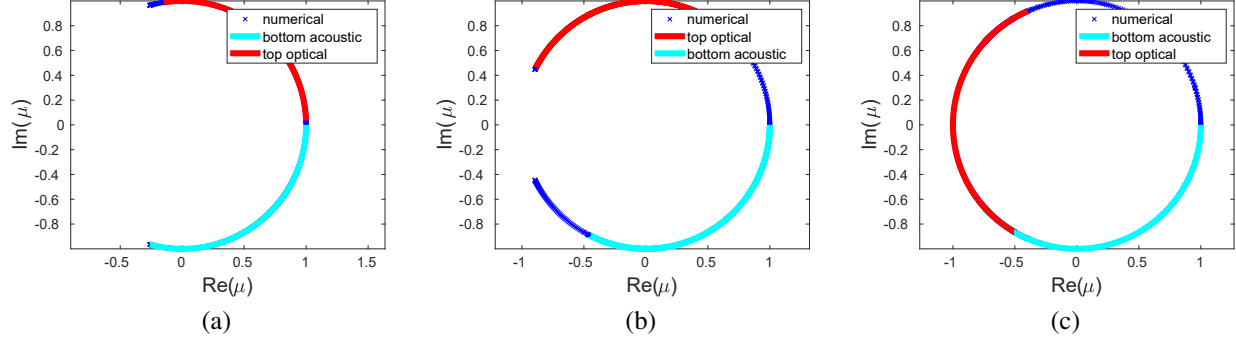


Figure 27: Numerically computed Floquet multipliers (dark blue crosses) and arcs of Floquet multipliers (47) corresponding to top optical ($\omega_+(k)$, red arc) and bottom acoustic ($-\omega_-(k)$, light blue arc) dispersion bands at (a) $\omega = 1.57$; (b) $\omega = 1.4$; (c) $\omega = 1.201$.

Under the mapping given by (47), the left ends of the arcs corresponding to the top optical and bottom acoustic bands, respectively, seen in Fig. 27, are associated with $\omega_+(\pi)$ and $-\omega_-(\pi)$. As ω is decreased, the two ends approach each other along the unit circle and eventually coincide when

$$e^{i2\pi\omega_+(\pi)/\omega} = e^{-i2\pi\omega_-(\pi)/\omega},$$

which yields

$$\frac{\omega_+(\pi) + \omega_-(\pi)}{\omega} = n,$$

where n is a positive integer. We find that the first such collision takes place when $n = 2$, which together with (37) yields

$$\omega = \frac{2 + \alpha\sqrt{2(K_\theta + 2K_s \cos^2 \phi_0)}}{2} \approx 1.2293.$$

This predicted value of $\omega = 1.2293$ is close to the first significant peak shown in Fig. 26(c), although there are also two smaller peaks to the right of it at $\omega = 1.231$ and $\omega = 1.239$. This discrepancy between predicted and actual collision frequency values may be attributed to numerical accuracy of computing the Floquet multipliers, as well as possible effects of weak nonlinearity.

The solution curve shown in Fig. 25(a) was continued until the frequency $\omega = 0.9972$, and thus includes solutions with frequencies $\omega \leq 1$. As noted in Sec. 4.2, these frequencies are associated with second harmonic resonances of the DB solution with the linear waves that have frequencies in the optical band. As a result, the corresponding solutions are no longer localized and instead possess non-decaying oscillatory wings. Such solutions are known as *phantom breathers* [122] or *nanoptera* [123, 124]. The latter term stems from their non-vanishing tails given the resonance with the linear modes. An example of a phantom breather with frequency $\omega = 0.9972$ (red curve) is shown in Fig. 28 along with the regular (localized) DB solution at $\omega = 1.02$ (dashed blue).

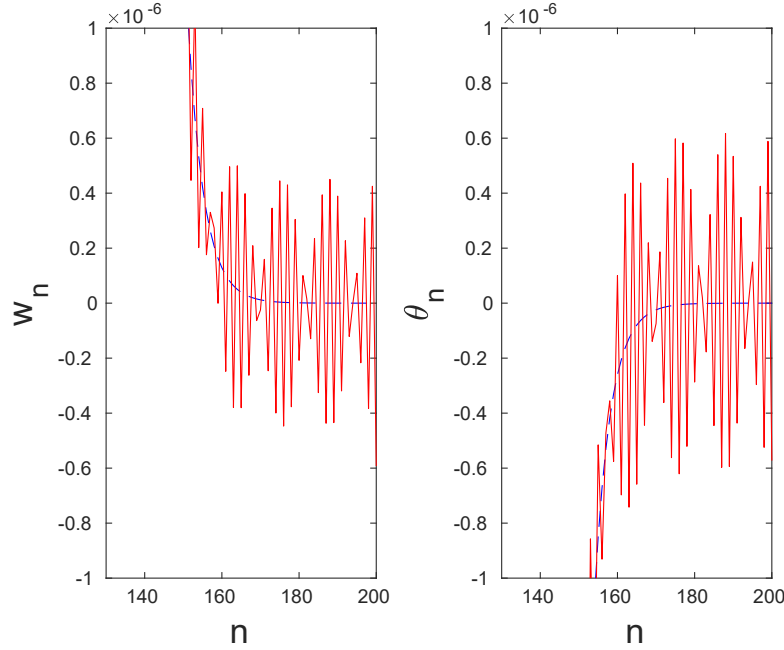


Figure 28: The angle and strain variables near the right end of the chain for the phantom breather with frequency $\omega = 0.9972$ (solid red) and the regular (localized) discrete breather with frequency $\omega = 1.02$ (dashed blue).

We now consider the Fourier spectrum associated with the dynamic evolution of the obtained breathers with prescribed frequency $\tilde{\omega}$. Fig. 29 shows the Fast Fourier Transform (FFT) results involving the dynamics simulated over a course of 100 oscillation periods for two different values of $\tilde{\omega}$, along with the acoustic and optical bands shaded in gray. In the case $\tilde{\omega} = 1.1$ (panel (a)), there are only two peaks at nonzero frequencies for the displayed range, at $\tilde{\omega}$ and $2\tilde{\omega}$, and the latter is clearly above the top of the optical band (the right shaded strip) at $\omega = 2$. When $\tilde{\omega} = 1.02$ (panel (b)), one can see a third nonzero-frequency peak in addition to $\tilde{\omega}$ and $2\tilde{\omega}$. This peak is at $\tilde{\omega}/2$ and is associated with the period-doubling instability, which is present at this frequency. Note that $2\tilde{\omega}$ is above the optical

band (the right shaded strip), and $\tilde{\omega}/2$ is above the acoustic band (the left shaded strip), so there are no resonances with either optical or acoustic linear waves. In contrast, in the case $\tilde{\omega} = 0.9972$ (not shown), the peak at $2\tilde{\omega}$ is just inside the optical band, and the second-harmonic resonance results in the phantom breather structure shown in Fig. 28.

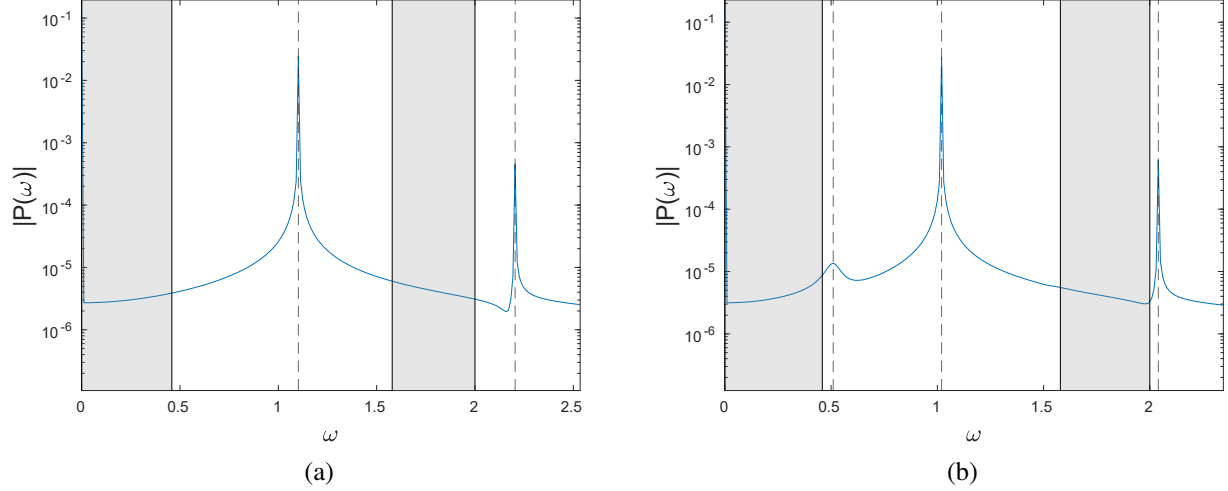


Figure 29: The amplitude spectrum $P(\omega)$ obtained using the FFT for different values of the prescribed breather frequency $\tilde{\omega}$: (a) $\tilde{\omega} = 1.1$; (b) $\tilde{\omega} = 1.02$. The left and right shaded stripes in each of the bottom panels indicate the acoustic and optical dispersion bands, respectively. The dashed vertical lines indicate $\tilde{\omega}$ and $2\tilde{\omega}$ in both panels and $\tilde{\omega}/2$ in panel (b). It is clear that the frequencies associated with the breather do not resonate with the linear spectral bands in the cases shown.

4.4 Snake-like solution branches

As we have seen, the existence of DB solutions with frequencies inside the band gap requires rather large angles ϕ_0 (above 16°) for the set of model parameters used in the previous subsection. Since large offset angles may render the present description of the system with only two degrees of freedom somewhat less accurate [125], we consider in what follows the parameters $\alpha = 5$, $K_s = 0.02$, $K_\theta = 0.01$, which allow breather existence at smaller values of ϕ_0 .

4.4.1 Branches associated with the $k = \pi$ mode

We start by considering solutions that exist when the bottom of the optical band is at $k = \pi$, which, as shown in Sec. 4.2, can occur when the angle ϕ_0 is above ϕ_0'' . Recalling that $\phi_0'' = 0.1588$ for the chosen parameter values, we set $\phi_0 = 10\pi/180 \approx 0.1745$. The corresponding dispersion relation plot is shown in Fig. 22(c).

To compute solutions associated with the $k = \pi$ mode, we modify our initial guess as follows. To obtain the initial guess for the angle variable θ_n , we solve the linear problem (34) for the finite chain of size $N = 200$ with zero strain and zero angle prescribed at the boundaries, observing that the eigenvalues ν are equal to the negative of the square of the frequencies that make up the optical and acoustic bands obtained for the linearized problem, and selecting the angle-related part of the eigenvector associated with the eigenvalue $\nu = -\omega_+^2(\pi) = -4$. Selecting the corresponding displacement part of the eigenvector did not yield nontrivial solutions, and thus we used the same form of the initial guess for u_n as in (46). Fig. 30 shows the initial guess we used in the computation.

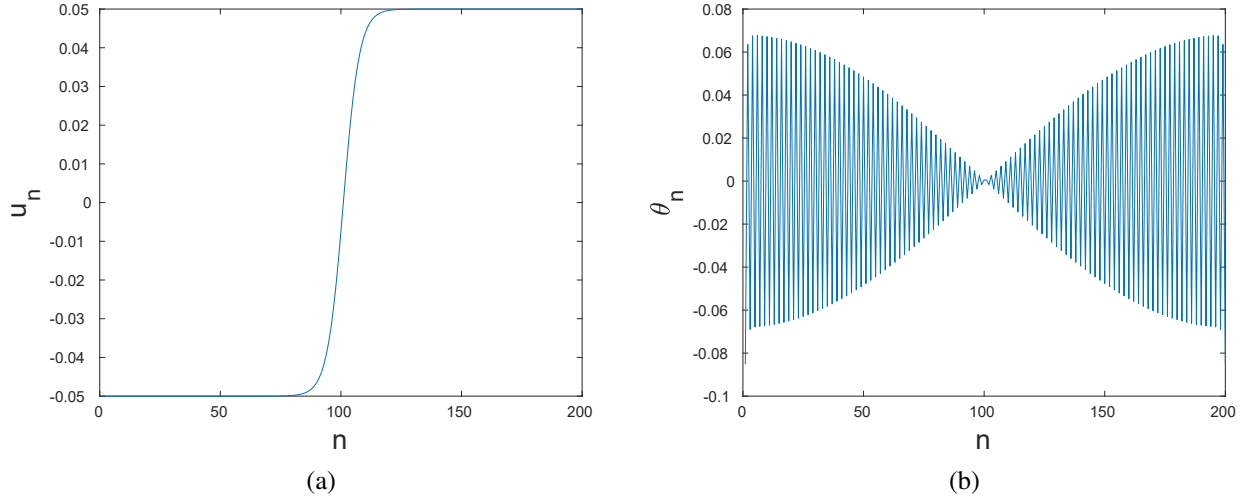


Figure 30: Initial guess for (a) displacement $u_n = \varepsilon_u \tanh(\delta(n - N/2))$; (b) angle θ_n obtained from the π -mode eigenvector (see the text for details). Here $\varepsilon_u = 0.05$ and $\delta = 0.15$.

The results of our computations are summarized in Fig. 31, which shows the energy of the obtained solution branches as a function of frequency. Blue, red and green curves show branches of DB solutions that have even symmetry, while the black curves indicate asymmetric solution branches. For each solution branch, thin dashed portions of the curve indicate the existence of real Floquet multi-

pliers satisfying $\mu > 1$, along with the corresponding real multipliers $1/\mu$ inside the unit circle along the real line. Thick dashed segments indicate the additional presence of real Floquet multipliers μ and $1/\mu$ satisfying $\mu < -1$ and thus corresponding to a period-doubling instability akin the one discussed in Sec. 4.3. Parts of the curve where there are only oscillatory instabilities with the maximum modulus of the Floquet multipliers exceeding 1.009 are shown by thin dotted segments, while along the thick dotted portions there are also real multipliers μ and $1/\mu$ with $\mu < -1$. Solid curves indicate the portions where there are no exponential instabilities, and the maximum modulus of the Floquet multipliers is below the threshold value 1.009. Small-magnitude oscillatory instabilities along the solid portions are similar to the ones observed in Sec. 4.3 and can be neglected, so that the associated solutions can be considered effectively (i.e., practically, for long-time simulations) stable. The threshold of 1.009 is (by necessity) somewhat arbitrary and is connected with observations over the time horizons selected for our numerical simulations of the breather dynamics.

We first consider the blue and red symmetric solution curves shown in panels (a) and (c), respectively, of Fig. 32. Panels (b) and (d) of the same figure show strain and angle variables for the solutions at selected points along the corresponding curves in panels (a) and (c) at the time instances of maximal amplitude. Near $\omega = 2$, the solutions for the blue curve have only a single trough in the angle θ_n . As the curve is traversed, this single trough evolves first into a double trough, as can be seen at points *A* and *B* in Fig. 32(b), and later into a quadruple trough at point *C*. Meanwhile, the strain w_n evolves from a single initial peak at point *A* into a single trough at point *B* in Fig. 32(b), and finally into a quadruple trough at point *C*. The solutions along the red curve near $\omega = 2$ have a single minimum in θ_n , which is maintained at points *A* and *B* in Fig. 32(d). However, as can be seen at point *C* in Fig. 32(d), these solutions also evolve from having a single minimum to multiple extrema. As before, in the strain component we see an inversion of an initial peak to a single trough as seen at points *A* and *B* in Fig. 32(d). A key distinction between the blue and red solution curves is that the solutions along the blue branch are site-centered, and the solutions along the red branch are bond-centered.

We remark that although both the energy and the amplitude of solutions along the blue and red branches decreases as the frequency approaches the edge of the optical band, they do not appear to tend to zero in the limit. This suggests that instead of bifurcating from the band edge, these DB branches retain a finite amplitude as their frequency approaches the band edge, akin the large-amplitude bright breathers computed in [126] for the Fermi-Pasta-Ulam lattices.

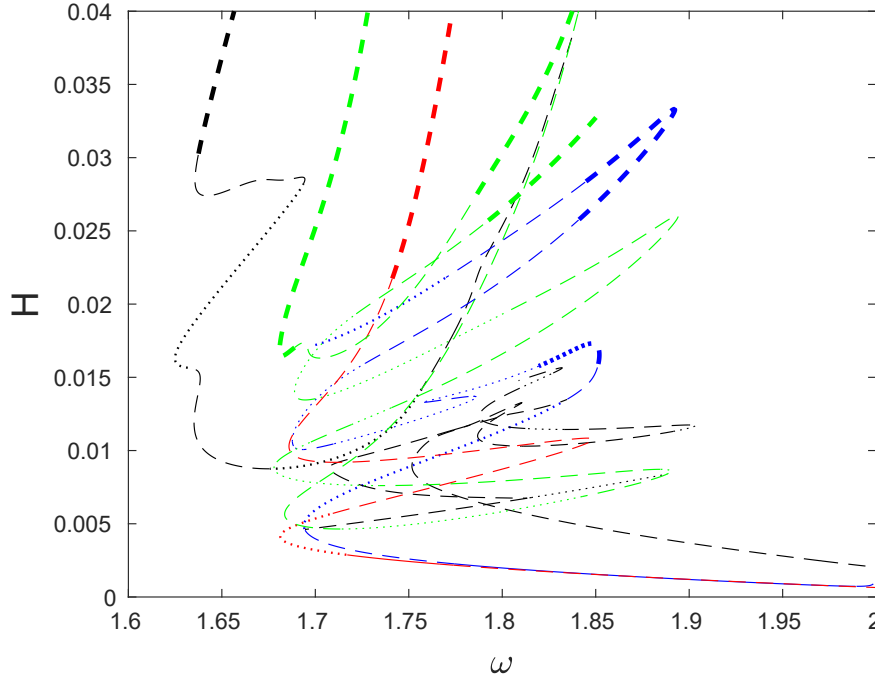


Figure 31: Energy H of the computed DB solutions as a function frequency ω . Blue, red and green curves are branches of solutions that have even symmetry, while the asymmetric solution curves are shown in black. Thin dashed portions of the curves indicate the presence of the real multiplier pairs $(1/\mu, \mu)$ with $\mu > 1$. Along the thick dashed segments there are also real multipliers $(1/\mu, \mu)$ with $\mu < -1$. Parts of the curve where there are only oscillatory instabilities with the maximum modulus of the Floquet multipliers exceeding 1.009 are indicated by thin dotted segments. Solutions that also have real multiplier pairs $(1/\mu, \mu)$ with $\mu < -1$ are along the thick dotted parts. Solid curves indicate the portions where there are no exponential instabilities, and the maximum modulus of the Floquet multipliers is below 1.009. Here and in the remainder of this subsection we have $\alpha = 5$, $K_s = 0.02$, $K_\theta = 0.01$, $N = 200$, and $\phi_0 = 10\pi/180$.

Examining now the stability of the solutions along the two branches, we note first that as shown in the left panel of Fig. 32(e), the two exchange an effective stability via a connecting unstable asymmetric solution branch. This is reminiscent of a similar phenomena observed in different settings (yet still connecting the bifurcations from site-centered and bond-centered solution branches) [127]; see also the discussion of [49], where asymmetric solution curves carry instabilities between neighboring symmetric solutions. The blue curve has a real Floquet multiplier pair $(1/\mu, \mu)$ with $\mu > 1$ until the bifurcation point at $\omega = 1.7742$ and $H = 2.264 \times 10^{-3}$, where it becomes effectively stable (modulo small-amplitude oscillatory instabilities), while the emerging asymmetric branch is exponentially unstable; in other words, this is a subcritical pitchfork bifurcation. The asymmetric branch then connects to the red curve, where a similar stability exchange (i.e., another subcritical pitchfork

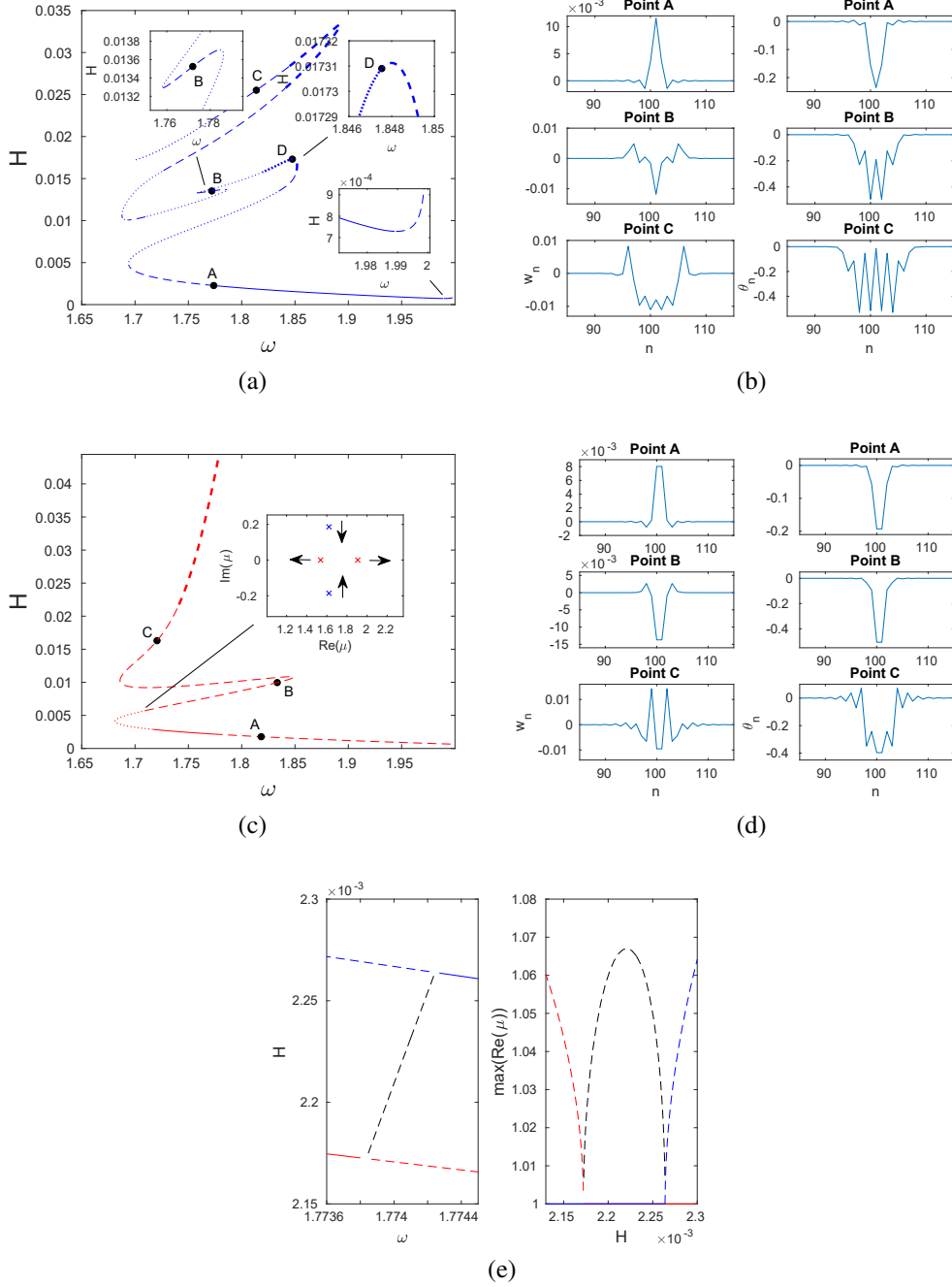


Figure 32: (a) Energy H as a function of frequency ω along the blue symmetric solution branch. The insets provide an enlarged view of the turning points. (b) Strain and angle variables for the solutions at the points A, B, and C in (a). (c) $H(\omega)$ along the red symmetric solution branch. The inset showing Floquet multipliers illustrates the emergence of an exponential instability. A pair of complex Floquet multipliers (blue crosses) associated with a solution before the transition collides to form two positive real multipliers (red crosses) associated with the solution after the collision. The corresponding symmetric multipliers inside the unit circle are not shown. (d) Strain and angle variables for the solutions at the points A, B, and C in (c). (e) Left panel: the unstable asymmetric branch connecting the red and blue symmetric branches (left panel). Right panel: maximum real Floquet multiplier as a function of energy for the three branches. All solution profiles are shown at the time instances of maximal amplitude.

bifurcation) takes place at $\omega = 1.7738$ and $H = 2.172 \times 10^{-3}$. The stability exchange is further illustrated in the right panel of Fig. 32(e), where we plot the maximum real Floquet multiplier μ as a function of the energy H .

Next, we note that the exponential instability that emerges from the oscillatory instability in the solutions along the red curve, indicated by the inset in Fig. 32(c), is due to the collision of two complex pairs of Floquet multipliers μ (only the multipliers outside the unit circle are shown in the inset). A similar collision is responsible for the transition to exponential instability near the first local maxima in the blue curve, which is indicated in the inset containing the point D in Fig. 32(a).

Panels (a) and (b) of Fig. 33 show a bifurcation at the point a along the blue curve, at which point the blue curve loses its exponential instability (while still retaining oscillatory instability modes). The instability is transferred to an asymmetric solution branch (again through a subcritical pitchfork bifurcation). Another exponentially unstable asymmetric branch bifurcates at the point b from this branch and at the point c from the blue curve. The resulting part of the bifurcation diagram, depicted in the right panel of Fig. 33(b), is reminiscent of the “snaking” behavior that has been observed in other systems [114, 115]. Further exploration of such snaking features and associated asymmetric branches in the present metamaterial setting is a potentially interesting topic for future studies.

We also observe that stability changes at the points where $H'(\omega)$ changes sign are associated with the emergence of a pair of real Floquet multipliers from $\mu = 1$. The multiplier $\mu > 1$ then corresponds to an exponential instability. One such example is shown in the inset of Fig. 32(a) zooming in on a sharp turning point. The initial stability change happens at a local minimum, and the second saddle-center bifurcation at a local maximum. This change in multiplicity of the unit Floquet multiplier at the extrema of the energy-frequency curve is similar to the one we observed earlier in Sec. 4.3 and again consistent with the stability criterion in [113]. The same mechanism is responsible for the onset of exponential instability at a local minimum of $H(\omega)$ near $\omega = 2$ (see the bottom right inset of Fig. 32(a)). Another example of such change in multiplicity takes place at the local maximum near the point D in Fig. 32(a) (see the inset). At this point, a second pair of real Floquet multipliers emerges from the unit circle, and this new pair subsequently collides at the point D with an already existing pair of real multipliers forming a complex quartet of Floquet multipliers. A similar emergence of a pair of real Floquet multipliers from $\mu = 1$ is observed at the local extrema of energy along the red curve.

As discussed above, a secondary asymmetric branch bifurcates from a primary asymmetric branch

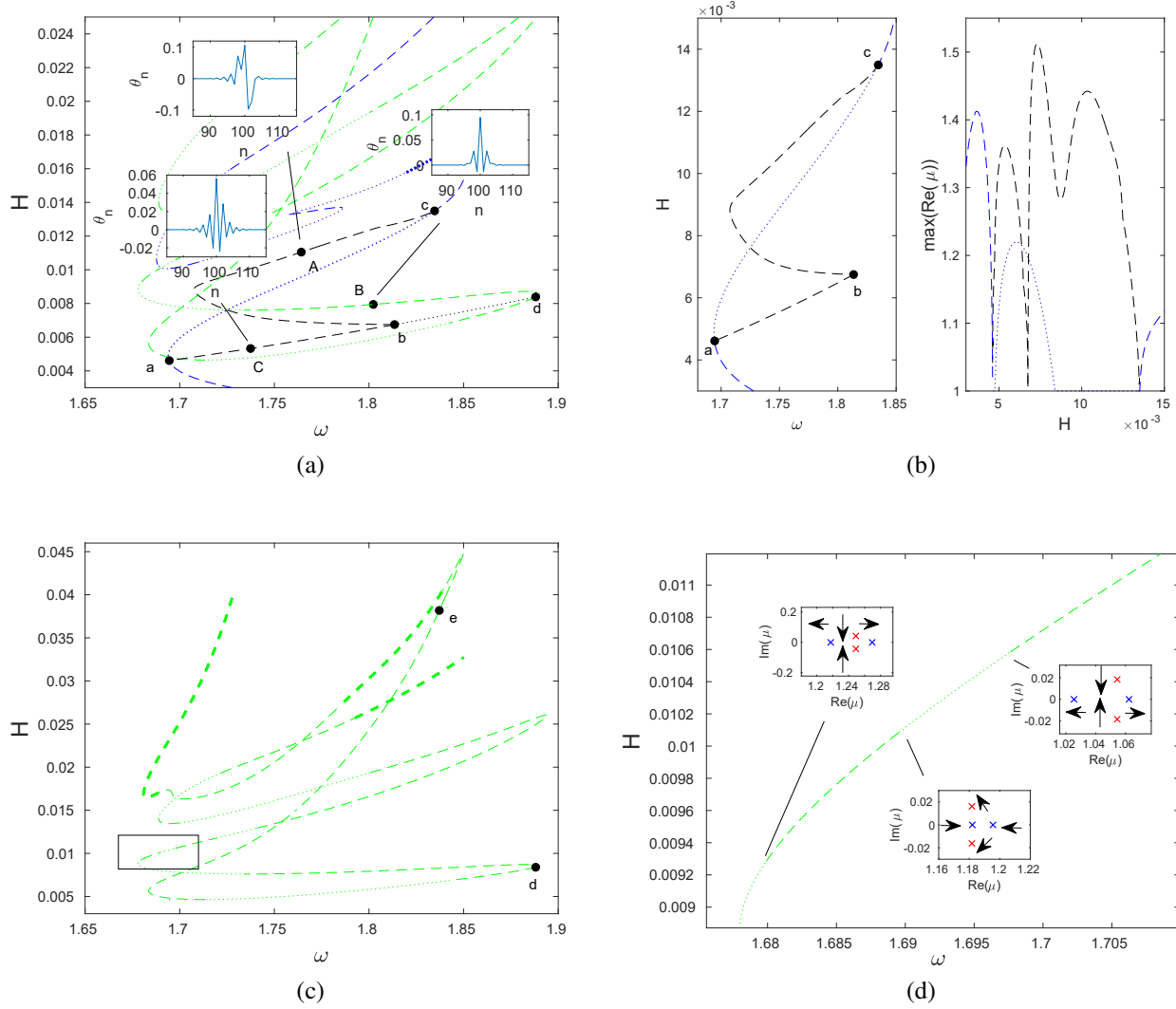


Figure 33: (a) Energy H as a function of frequency ω along the blue and green symmetric solution branches and bifurcating branches of asymmetric solutions, with a , b , c , and d marking the bifurcation points. The insets show the solutions of the asymmetric and symmetric branches at the points A , B , and C . (b) The stability exchange between the symmetric (blue) and the asymmetric (black) branch. Both the associated portion of the bifurcation diagram and the dominant multiplier of each branch associated with the instability growth rate are shown. (c) Energy H versus frequency ω for the green symmetric solution branch with d and e marking the bifurcation points (see Fig. 34 for the asymmetric branch bifurcating from e). (d) The enlarged view of the region inside the rectangle in (c). The insets show the transition from exponential to oscillatory instabilities and vice versa that take place over the green symmetric curve. The red and blue crosses indicate Floquet multipliers μ outside the unit circle that correspond to solutions before and after the transition point, respectively.

at the point b in panels (a) and (b) of Fig. 33. The primary branch continues on past this bifurcation point to intersect with a symmetric solution curve at the point d , shown in green color in panel (a).

Following this green curve, shown in its entirety in Fig. 33(d), upward from point d , we observe the sequence of events illustrated in Fig. 33(d). Two pairs of real multipliers $(1/\mu, \mu)$ with $\mu > 1$ emerge due to two pairs of complex multipliers colliding on the real axis (only the multipliers outside the unit circle are shown in the insets). The real multipliers then collide to form complex ones anew, and subsequently reemerge again due to another collision of the oscillatory multipliers. Eventually, the real multipliers rejoin the unit circle. This provides a sense of the complexity of the associated bifurcation diagram.

Traveling downward now from the point d along the green curve, we eventually arrive at another bifurcation of an asymmetric solution branch at the point e . This bifurcation is shown in Fig. 34 and appears not to be associated with any stability change. A closer examination shows that this is due to the prior existence of two pairs of real Floquet multipliers (one is not included due to its larger magnitude), shown in the inset zooming in around the point D . After the bifurcation, a third pair of real Floquet multipliers joins the other two, as shown in the inset of Fig. 34(b) zooming in around the point E , indicating the emergence of a new exponential instability. It is important to note that in both insets of panel (b) around points D and E , an additional exponential instability is present but not shown due to its larger magnitude. As before, we also observe changes in stability due to collisions of complex pairs, as shown in the inset zooming in around the point F , as well as due to turning points in energy, e.g., near the local minimum of the black asymmetric solution curve of Fig. 34.

Finally, we consider the asymmetric branch in Fig. 31 that has not yet been discussed. This branch is unique among the other asymmetric branches in that it comes near the π -mode edge of the optical branch. However, that similar to the blue and red branches, it does not appear to bifurcate from the edge. As in the previous cases, we observe the emergence or collision of real Floquet multipliers at the turning points in energy. In Fig. 35(a), we show the evolution of the solutions as the branch is traversed, and in Fig. 35(b), one can see the emergence of pairs of real multipliers from complex ones; once again these are signaled by transitions from dotted lines to dashed ones.

To examine the consequences of an instability associated with real Floquet multipliers $\mu > 1$ along the blue and red symmetric solution branches, we perturb unstable solutions at various points featuring such an exponential instability along the corresponding eigenmodes and simulate the resulting dynamics. In Fig. 36(a), these points on the blue and red dashed portions of the curves are labeled $A - L$. The corresponding final states are indicated by the points $A^* - L^*$. As can be seen in the inset of Fig. 36(a), in all cases, the perturbed solution eventually settles onto one of the two effectively

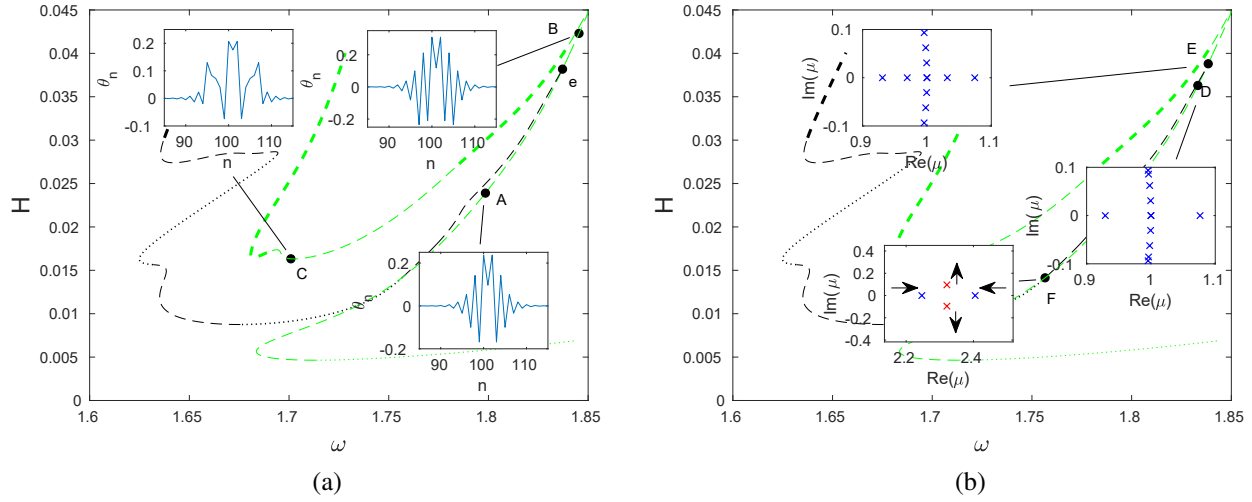


Figure 34: (a) Energy H as a function of frequency ω along the green symmetric solution branch and a branch of asymmetric solutions (different from the ones discussed earlier) bifurcating at the point e . The insets include profiles of the angle variable at the points A , B , and C . (b) The insets pointing toward points D and E show the emergence of a third pair of real Floquet multipliers. In both insets, an additional pair of real multipliers is present but not shown due to its larger magnitude. The inset pointing toward the point F illustrates the collision of two pairs of real multipliers to form two complex pairs. The red and blue crosses indicate Floquet multipliers outside the unit circle that correspond to solutions before and after the transition point, respectively.

stable regions of the blue and red solution curves, with an apparent preference toward the blue curve, which is effectively stable for a much larger interval of frequencies than the red curve.

As an example, we consider the point E in Fig. 36(a) and show the dynamic evolution of the perturbed solution in Fig. 36(b-d). Here $\epsilon = 10^{-5}$, and the largest real Floquet multiplier is $\mu = 1.3596$. The space-time plots of the displacement and angle are shown in panels (b) and (c), respectively, while panel (d) zooms in on the dynamic evolution of the angle variable at smaller times. Both (c) and (d) are shown on a logarithmic scale. This facilitates the last plot to show the nontrivial amount of radiation that is emitted by the perturbed wave as it develops, as well as its temporary mobility. Eventually, this perturbed wave settles into a stable breather, associated with the point E^* , as can be verified by comparing its properties (once it settles) with those of the latter solution.

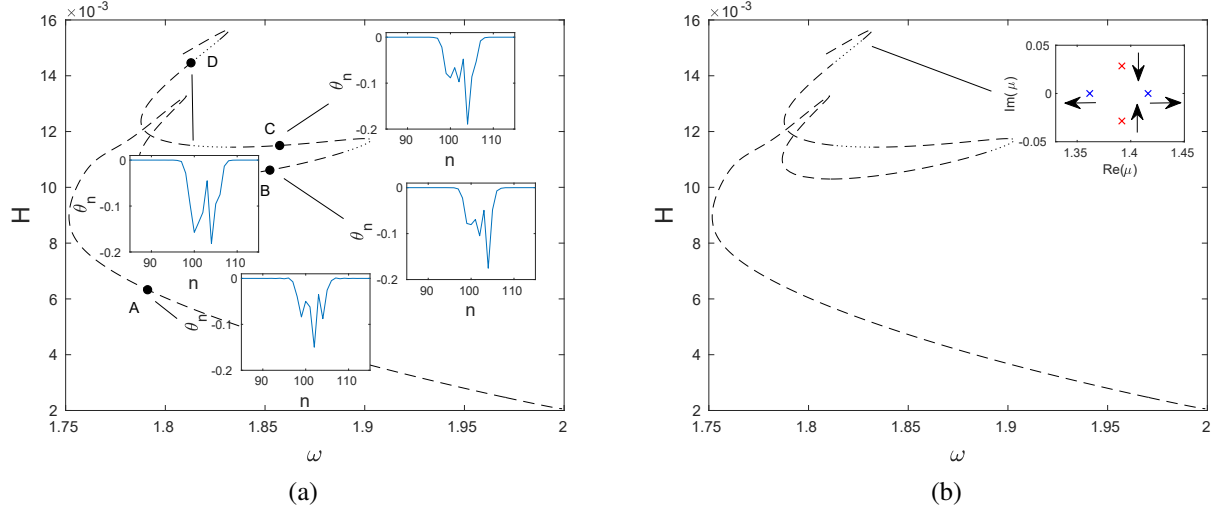


Figure 35: (a) Energy H as a function of frequency ω along an asymmetric solution branch that exists near the $k = \pi$ edge of the optical branch. The insets include profiles of the angle variable at the points A , B , C , and D . (b) The same branch, with the inset showing the collision of two pairs of complex Floquet multipliers to form two real pairs. Blue and red crosses show the pairs outside the unit circle that correspond to solutions before and after the transition, respectively.

4.4.2 Zero-mode optical and π -mode acoustic branches

We now consider breather solutions bifurcating from the bottom of the optical band at $k = 0$, as well as solutions that exist near the top of the acoustic branch at $k = \pi$. To ensure that the optical branch has a minimum at $k = 0$, we choose $\phi_0 = 8\pi/180 \approx 0.1396$, which is below $\phi_0'' = 0.1588$. The corresponding dispersion relation plot is shown in Fig. 22(b).

Using the continuation procedure with the initial guess of the form (46), we obtained the blue and red branches of symmetric DB solutions shown in Fig. 37 that are site-centered and bond-centered, respectively, and bifurcate from the edge of the optical band at $k = 0$. The green solution branch of site-centered breathers shown in the same figure extends from near the top of the acoustic band at $k = \pi$ and was obtained using the initial guess that was constructed as described in Sec. 4.4.1. As in the previous case discussed in Sec. 4.4.1, we expect there to be other solution branches emanating from the band edges, as well as secondary branches that bifurcate from the primary ones. However, the discussion below is limited to the three branches included in Fig. 37.

Fig. 38, shows each of the branches (left panels) along with the evolution of the strain and angle variables along each curve (right panels). Along the blue branch shown in panel (a), the strain variable

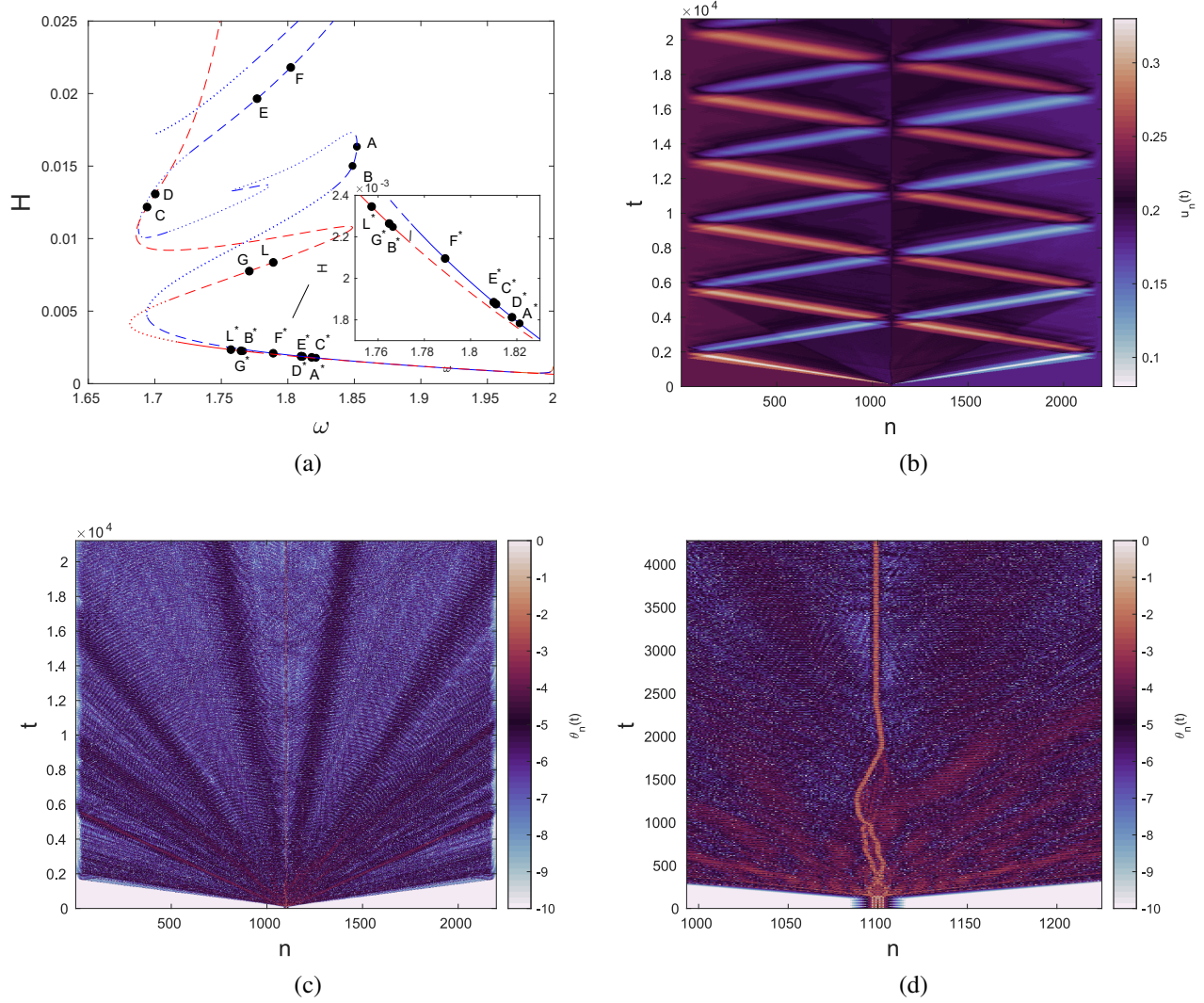


Figure 36: (a) Energy H as a function of frequency ω along the red and blue symmetric solution curves. The points A - L indicate the perturbed unstable solutions, while the points A^* - L^* mark the corresponding final states. The inset zooms in on the region including the end points. (b) Space-time plot of the displacement $u_n(t)$ for the solution corresponding to point E . Here $\epsilon = 10^{-5}$ is the strength of the perturbation, and $\mu = 1.3596$ is the largest real Floquet multiplier. (c) Space-time plot of the angle $\theta_n(t)$. (d) Enlarged view of (c). Both (c) and (d) are shown in a logarithmic plot to facilitate the visualization of the small scales involving dispersive wave radiation as a result of the instability.

shown in panel (b) has a single peak at point A , which evolves to a single trough at point B , and then to a triple trough at point C . Meanwhile, the angle variable changes from a single trough at point A to a double trough at point B , and finally to a quadruple trough at point C .

In the case of the red symmetric branch (panel (c)), the strain variables shown in panel (d) initially has a single peak at point A , which then evolves into a single trough at point B and later to a double

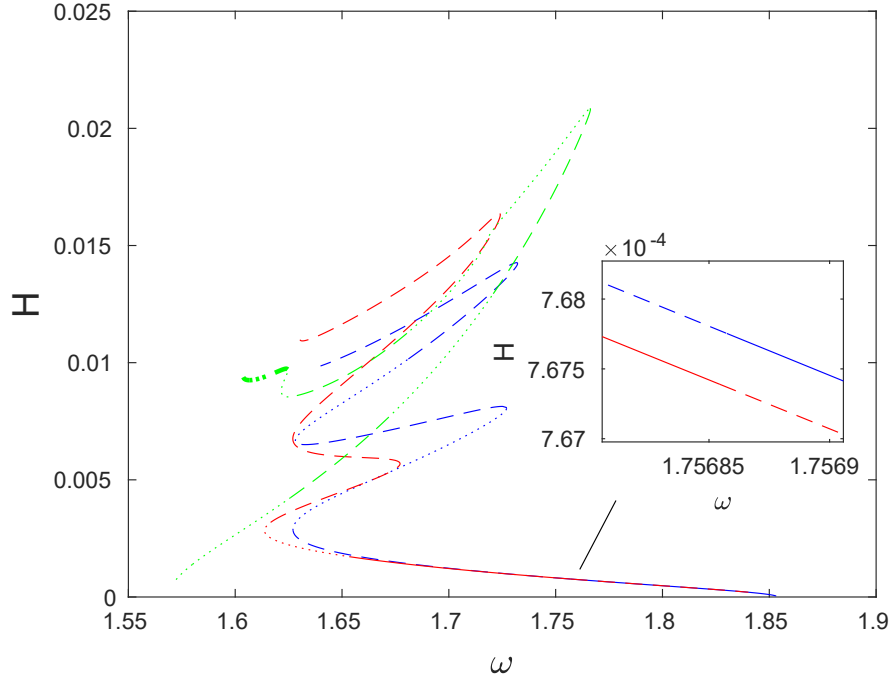


Figure 37: Energy H of the computed DB solutions as a function frequency ω . Blue and red curves bifurcate from the optical band at $k = 0$, while the green curve is associated with the acoustic π -mode. All of the branches shown contain solutions with even symmetry. Thin dashed portions of the curves indicate the presence of the real multiplier pairs $(1/\mu, \mu)$ with $\mu > 1$. Along the thick dashed segments there are also real multipliers $(1/\mu, \mu)$ with $\mu < -1$. Parts of the curve where there are only oscillatory instabilities with the maximum modulus of the Floquet multipliers exceeding 1.009 are indicated by thin dotted segments. Solutions that also have real multiplier pairs $(1/\mu, \mu)$ with $\mu < -1$ are along the thick dotted parts. Solid curves indicate the portions where there are no exponential instabilities, and the maximum modulus of the Floquet multipliers is below 1.009. Here and in the remainder of this subsection we have $\alpha = 5$, $K_s = 0.02$, $K_\theta = 0.01$, $N = 200$, and $\phi_0 = 8\pi/180$.

trough at point C . Meanwhile, the angular variable has a single trough at point A and develops steps at point B , which subsequently evolve into a triple trough at point C . In this case too, as is the case for the blue branch, the expansion of the solution to more sites bearing high amplitudes is associated with higher energies along the snake-like solution branch.

For the green solution branch that extends to near the top of the acoustic band (panel (e)), we find that as we move from point A to point C , the strain variable shown in panel (f) develops two peaks. Notice that in this case, the point A illustrates the provenance of this mode from a $k = \pi$ band edge, since adjacent sites are out of phase with each other at the starting point of the relevant branch in panel (f). In the angular variable, we observe a widening of the core from point A to point C along

with the emergence of two troughs at point C .

As in the previous case discussed in Sec. 4.4.1, we expect the existence of an asymmetric solution branch connecting the red and blue branches and facilitating an exchange of the exponential instability shown in the inset in Fig. 37. Due to the extremely narrow frequency and energy intervals over which this exchange takes place, we were unable to accurately compute the asymmetric solutions. Similar stability exchange through symmetry-breaking bifurcations is expected at other points where the emergence of an exponential instability is not caused by a collision of complex multipliers, as depicted in the inset of Fig. 38(c), or associated with splitting of a pair of real multipliers at $\mu = 1$ when $H'(\omega)$ changes sign.

4.5 Concluding remarks

In this chapter we have revisited a dynamical system that constitutes a prototypical, experimentally tractable example of a nonlinear mechanical metamaterial. While earlier work [94, 96, 112] on this system focused on the possibility of its featuring propagating nonlinear excitations in the form of traveling waves, the emphasis in this chapter has been on the dynamics of discrete breathers with parameters allowed by the experimental setting (in accordance, e.g., with the Supplemental material in [96]). To explore the DB waveforms, we started with a systematic analysis of the linear spectrum of the system. We ensured the presence of a gap between the acoustic and optical branches of the linear dispersion relation. In addition, we ensured the avoidance of resonances involving the second harmonic, in order for the DBs to exist [120]. When the relevant conditions applied, we were able to identify a rich set of families of discrete breathers, both symmetric and asymmetric. This includes DB solutions bifurcating from or existing near the lower edge of the optical band, as well as solution branches that extend to the upper edge of the acoustic band. Utilizing the energy-vs-frequency representation of the associated bifurcation diagrams, we were able to showcase numerous solution branches, and importantly identified the wealth of bifurcations emerging between them. These included saddle-center bifurcations (leading to exponential instabilities), symmetry-breaking bifurcations (involving asymmetric branches) and finally Hamiltonian-Hopf bifurcations associated with the emergence of complex multipliers. We also briefly discussed the nonlinear evolution dynamics associated with different branch instabilities and showed how these could lead to a restructuring of the

waveforms towards stable DB patterns, while shedding some dispersive wave radiation as a result of the dynamical instability.

Naturally, we believe that this chapter paves the way for further explorations of nonlinear wave structures in this class of metamaterial lattices. The relevant possibilities emerge at different levels of experiment, computation and theory. Experimentally, it remains to be seen whether parametric regimes considered in this chapter allow for the identification of the discrete breather waveforms examined in this chapter. Theoretically, we showed that some of the obtained solutions bifurcate from the band edges of the dispersion relation. This is a feature that calls for the analysis of such a bifurcation via multiple-scale expansions and the possible derivation of a nonlinear Schrödinger type model to describe it, an effort that is already underway [128]. Lastly, it would be particularly interesting to extend the relevant considerations of breathing waveforms to (numerically) exact computations of discrete traveling solutions along the lines of recent connections between the two types of structures [31]. Such studies are currently in progress and will be reported in future publications.

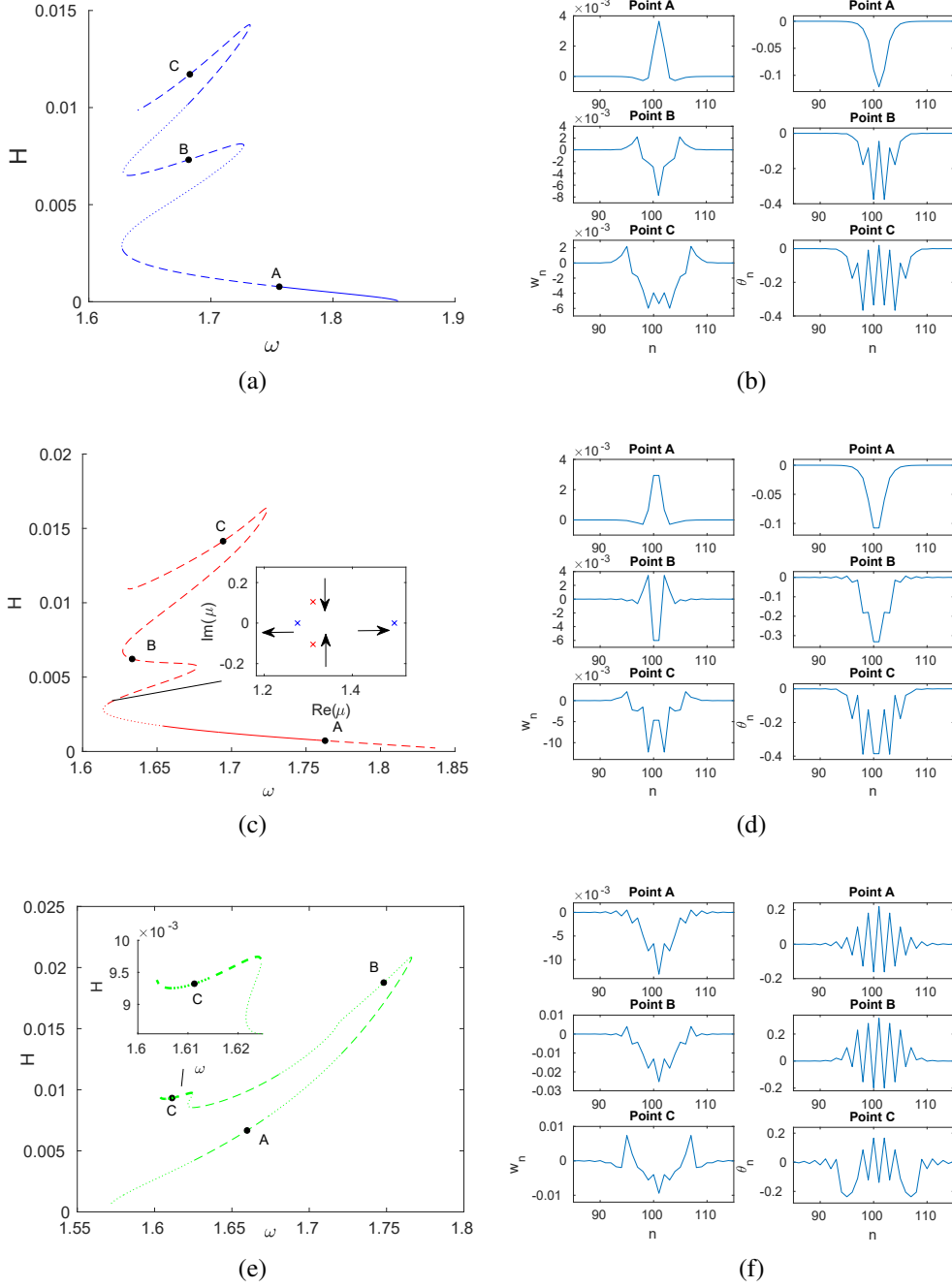


Figure 38: (a) Energy H as a function of frequency ω along the blue symmetric solution branch. (b) Strain and angle variables for the solutions at the points A, B, and C in panel (a). (c) $H(\omega)$ along the red symmetric solution branch. The inset showing Floquet multipliers illustrates the emergence of an exponential instability. A pair of complex Floquet multipliers (red crosses) associated with a solution before the transition collides to form two positive real multipliers (blue crosses) associated with the solution after the collision. The corresponding symmetric multipliers inside the unit circle are not shown. (d) Strain and angle variables for the solutions at the points A, B, and C in panel (c). (e) $H(\omega)$ along the green symmetric solution branch. The inset shows the enlarged view near the end of the computed branch. (f) Strain and angle variables for the solutions at the points A, B, and C in panel (e). All solution profiles are shown at the time instances of maximal amplitude.

Appendix A

In this Appendix, we derive the condition for the change in multiplicity of the zero eigenvalue that generalizes the corresponding condition in [20, 21, 31, 32] to the case when the energy of a STW is not necessarily a single-valued function of its velocity. As in [31, 32], we consider a more general Hamiltonian than in [20, 21] that goes beyond nearest-neighbor interactions. However, in [31, 32] the effect of essential spectrum of the linearization operator was neglected in the derivation of the stability criterion and perturbation results. Moreover, the proof was provided for the displacement formulation and assumed localized displacements. Following [20, 21], here we consider the strain formulation more appropriate for the problem at hand and work with weighted spaces that shift the essential spectrum into the left half-plane.

A.1 Weighted spaces, skew symmetry and essential spectrum

Consider a Hamiltonian system in the form

$$H = \sum_{n \in \mathbb{Z}} \left(\frac{1}{2} p_n^2 + U_n(w) \right) = \sum_{n \in \mathbb{Z}} H_n(w(t), p(t)), \quad (48)$$

where $p(t) = [p_n(t)]$ is an infinite vector of particle momenta, $w(t) = [w_n(t)]$ is the strain vector, and the potential energy term $U_n(w)$ may include long-range interactions as in (1). The dynamics of the lattice are governed by

$$\frac{d}{dt} r(t) = \mathcal{J} \frac{\partial H}{\partial r}, \quad r(t) = \begin{pmatrix} w(t) \\ p(t) \end{pmatrix}, \quad \mathcal{J} = \begin{pmatrix} 0 & e^\partial - I \\ I - e^{-\partial} & 0 \end{pmatrix}. \quad (49)$$

Here $e^{\pm\partial}$ are the shift operators satisfying $(e^{\pm\partial} x)_i = x_{i \pm 1}$, and I is the identity operator.

Remark 1. The operator \mathcal{J} is invertible on space $\ell^2 \times \ell^2$, but the inverse is not bounded in this space because zero is in the essential spectrum of \mathcal{J} . In particular, if $\mathbf{1}$ represents a vector with all elements being 1, then $\mathcal{J} \begin{pmatrix} c_1 \mathbf{1} \\ c_2 \mathbf{1} \end{pmatrix}$ vanishes for any c_1 and c_2 . By using weighted spaces, one can make \mathcal{J} a one-to-one function and change the essential spectrum of \mathcal{J} so that its inverse is bounded. In particular, if $a > 0$ and $\ell_{\pm a}^2 = \{u : \sum_{j \in \mathbb{Z}} |u_j|^2 e^{\pm 2aj} < \infty\}$, then the inverse of \mathcal{J} on $\ell_a^2 \times \ell_a^2$ is explicitly given by

$$\mathcal{J}_{a,a}^{-1} = \begin{pmatrix} 0 & -\sum_{k=1}^{\infty} e^{k\partial} \\ -\sum_{k=0}^{\infty} e^{k\partial} & 0 \end{pmatrix} \quad (50)$$

and the inverse of \mathcal{J} on $\ell_{-a}^2 \times \ell_{-a}^2$ is of the form

$$\mathcal{J}_{-a,-a}^{-1} = \begin{pmatrix} 0 & \sum_{k=0}^{-\infty} e^{k\partial} \\ \sum_{k=-1}^{-\infty} e^{k\partial} & 0 \end{pmatrix}. \quad (51)$$

In particular, $\mathcal{J}_{a,a}^{-1}u = \mathcal{J}_{-a,-a}^{-1}u$ when $u \in (\ell_a^2 \cap \ell_{-a}^2) \times (\ell_a^2 \cap \ell_{-a}^2)$ and

$$\begin{pmatrix} \sum_{k=-\infty}^{\infty} e^{k\partial} & 0 \\ 0 & \sum_{k=-\infty}^{\infty} e^{k\partial} \end{pmatrix} u = 0.$$

Remark 2. If one considers \mathcal{J} on $\ell^2 \times \ell^2$, then its adjoint is also viewed as an operator on $\ell^2 \times \ell^2$, and in particular $\mathcal{J}^* = -\mathcal{J}$, which implies that \mathcal{J} is skew-symmetric. If \mathcal{J} is defined on $\ell_a^2 \times \ell_a^2$, then its adjoint $\mathcal{J}_{a,a}^*$ can be viewed as on $\ell_{-a}^2 \times \ell_{-a}^2$. Since we can also treat \mathcal{J} as an operator $\mathcal{J}_{-a,-a}$ on $\ell_{-a}^2 \times \ell_{-a}^2$, then

$$\langle u, \mathcal{J}_{a,a}v \rangle_{\ell^2 \times \ell^2} + \langle \mathcal{J}_{-a,-a}u, v \rangle_{\ell^2 \times \ell^2} = 0$$

where $u \in \ell_a^2 \times \ell_a^2$, $v \in \ell_{-a}^2 \times \ell_{-a}^2$ and $\langle \cdot, \cdot \rangle_{\ell^2 \times \ell^2}$ represents the inner product on $\ell^2 \times \ell^2$. This property can be equivalently written as $\mathcal{J}_{a,a}^* = -\mathcal{J}_{-a,-a}$ and it is another version of the skew-symmetry. Moreover, since \mathcal{J}^{-1} has different inverses on different weighted spaces, it in general does not inherit the skew symmetry from \mathcal{J} .

We now assume that (49) has a smooth family of solitary traveling wave solutions which have the form

$$r_{tw}(t; s) = \begin{pmatrix} w_{tw}(t; s) \\ p_{tw}(t; s) \end{pmatrix}, \quad w_{tw,n}(t; s) = \hat{w}(\xi(s)), \quad p_{tw,n}(t; s) = \hat{p}(\xi(s)), \quad (52)$$

where $\xi(s) = n - c(s)t$ and $c(s)$ is the velocity of the wave, which is strictly above the sound speed and depends on the parameter s . We assume that s provides a regular parametrization of the energy-velocity curve, so that $c'(s)$ and $H'(s)$ do not vanish simultaneously. This parametrization is not necessarily unique. It is convenient to use rescaled time $\tau = c(s)t$, so that the wave period is rescaled to one. Then we have

$$\frac{dR}{d\tau} = \frac{1}{c(s)} \mathcal{J} \frac{\partial H}{\partial R}, \quad R(\tau) = \begin{pmatrix} W(\tau) \\ P(\tau) \end{pmatrix} = r(t). \quad (53)$$

Linearizing (53) around the solution $R_{tw} = \begin{pmatrix} W_{tw} \\ P_{tw} \end{pmatrix}$ with $R(\tau) = R_{tw}(\tau) + \epsilon S(\tau)$, we find

$$\frac{dS}{d\tau} = \frac{1}{c(s)} \mathcal{J} \frac{\partial^2 H}{\partial R^2} \Big|_{R=R_{tw}} S(\tau). \quad (54)$$

We consider perturbations in the form $S(\tau) = S_{tw}(\tau)e^{\nu\tau}$, where

$$S_{tw} = \begin{pmatrix} X_{tw} \\ Y_{tw} \end{pmatrix}$$

is a traveling wave with unit velocity; i.e., periodic modulo shift with period 1. This yields the eigenvalue problem

$$\mathcal{L} S_{tw}(\tau) = \nu S_{tw}(\tau) \quad (55)$$

for the linear operator

$$\mathcal{L} := \frac{1}{c(s)} \mathcal{J} \frac{\partial^2 H}{\partial R^2} \Big|_{R=R_{tw}} - \frac{d}{d\tau} \quad (56)$$

with eigenvalue ν , which is related to the eigenvalue λ used in Chapter 2 via $\nu = \lambda/c(s)$ due to the time rescaling. Note also that Floquet multiplier μ is related to ν via $\mu = e^\nu$. For the Hamiltonian (1) the eigenvalue problem becomes

$$\begin{aligned} & -\frac{d}{d\tau} \begin{pmatrix} X_{tw,j}(\tau) \\ Y_{tw,j}(\tau) \end{pmatrix} + \frac{1}{c(s)} \begin{pmatrix} Y_{tw,j+1}(\tau) - Y_{tw,j}(\tau) \\ V''(W_{tw,j}(\tau))X_{tw,j}(\tau) - V''(W_{tw,j-1}(\tau))X_{tw,j-1}(\tau) \end{pmatrix} \\ & + \frac{1}{c(s)} \begin{pmatrix} 0 \\ \sum_{m=1}^{\infty} \Lambda(m) \left[\sum_{l=0}^{m-1} X_{tw,j+l}(\tau) - \sum_{l=-m}^{-1} X_{tw,j+l}(\tau) \right] \end{pmatrix} = \nu \begin{pmatrix} X_{tw,j}(\tau) \\ Y_{tw,j}(\tau) \end{pmatrix}. \end{aligned} \quad (57)$$

In order to investigate the case with well-localized perturbations S_{tw} (that belong to spaces like $(\ell_a^2 \cap \ell_{-a}^2) \times (\ell_a^2 \cap \ell_{-a}^2)$), we view \mathcal{L} as an operator densely defined on $D_{tw,a,a}^0([0, 1])$ with domain $D_{tw,a,a}^1([0, 1])$, where

$$\begin{aligned} D_{tw,a,a}^0([0, 1]) := & \left\{ Z(\tau) = \begin{pmatrix} X(\tau) \\ Y(\tau) \end{pmatrix}, \tau \in [0, 1] \middle| Z(1) = \begin{pmatrix} e^{-\partial} & 0 \\ 0 & e^{-\partial} \end{pmatrix} Z(0), \right. \\ & \left. \int_0^1 \sum_{j \in \mathbb{Z}} (|X_j(\tau)|^2 e^{2a(j-\tau)} + |Y_j(\tau)|^2 e^{2a(j-\tau)}) d\tau < \infty \right\} \end{aligned}$$

and

$$\begin{aligned} D_{tw,a,a}^1([0, 1]) := & \left\{ Z(\tau) = \begin{pmatrix} X(\tau) \\ Y(\tau) \end{pmatrix}, \tau \in [0, 1] \middle| Z(1) = \begin{pmatrix} e^{-\partial} & 0 \\ 0 & e^{-\partial} \end{pmatrix} Z(0), \right. \\ & \left. \int_0^1 \sum_{j \in \mathbb{Z}} [(|X_j(\tau)|^2 + |X_j'(\tau)|^2) e^{2a(j-\tau)} + (|Y_j(\tau)|^2 + |Y_j'(\tau)|^2) e^{2a(j-\tau)}] d\tau < \infty \right\}, \end{aligned}$$

with prime denoting the time derivative. Following the steps similar to the discussion about \mathcal{J} on $\ell_a^2 \times \ell_a^2$, we can also show that \mathcal{J} has a bounded inverse on $D_{tw,a,a}^0([0, 1])$.

We note that when \mathcal{L} is considered on unweighted spaces such as $D_{tw,0,0}^0([0, 1])$, zero is usually embedded in the essential spectrum of \mathcal{L} . To be specific, consider the Hamiltonian (1). Since R_{tw} tends to zero and $V''(0) = 1$, the limiting operator \mathcal{L}_∞ can be defined as

$$\begin{aligned} \mathcal{L}_\infty \begin{pmatrix} X_{tw,j}(\tau) \\ Y_{tw,j}(\tau) \end{pmatrix} = & -\frac{d}{d\tau} \begin{pmatrix} X_{tw,j}(\tau) \\ Y_{tw,j}(\tau) \end{pmatrix} + \frac{1}{c(s)} \begin{pmatrix} Y_{tw,j+1}(\tau) - Y_{tw,j}(\tau) \\ X_{tw,j}(\tau) - X_{tw,j-1}(\tau) \end{pmatrix} \\ & + \frac{1}{c(s)} \begin{pmatrix} 0 \\ \sum_{m=1}^{\infty} \Lambda(m) \left[\sum_{l=0}^{m-1} X_{tw,j+l}(\tau) - \sum_{l=-m}^{-1} X_{tw,j+l}(\tau) \right] \end{pmatrix} \end{aligned} \quad (58)$$

Substituting

$$\begin{pmatrix} X_{tw,j}(\tau) \\ Y_{tw,j}(\tau) \end{pmatrix} = e^{ik(j-\tau)} \begin{pmatrix} b_1 \\ b_2 \end{pmatrix}$$

into $\nu S_{tw} = \mathcal{L}_\infty S_{tw}$ and using $\Lambda(m) = J(e^\alpha - 1)e^{-\alpha|m|}$, $m = 1, 2, \dots$, one can compute the essential spectrum (similar to [21]) of \mathcal{L} on $D_{tw,0,0}^0([0, 1])$ in the form

$$\left\{ \nu = i \left(k \pm \frac{2}{c(s)} \sin \frac{k}{2} \sqrt{1 + \frac{J(e^\alpha + 1)}{2(\cosh \alpha - \cos k)}} \right), k \in \mathbb{R} \right\}. \quad (59)$$

Thus in this case the essential spectrum is along the imaginary axis and includes 0. Similarly, the essential spectrum of \mathcal{L} on $D_{tw,a,a}^0([0, 1])$ with $a > 0$ is obtained by replacing k by $k + ia$ in the above, which yields

$$\left\{ \nu = -a + ik \pm \frac{2i}{c(s)} \left(\cosh \frac{a}{2} \sin \frac{k}{2} + i \cos \frac{k}{2} \sinh \frac{a}{2} \right) \times \right. \\ \left. \sqrt{1 + \frac{J(e^\alpha + 1)}{2(\cosh \alpha - \cos k \cosh a + i \sin k \sinh a)}}, k \in \mathbb{R} \right\}. \quad (60)$$

One can show that for $c(s) > c_s$, where we recall that c_s is the sound speed defined in (6), the essential spectrum in this case is contained in the left half plane $\text{Re}(\nu) < 0$ (and thus does not include zero) for $0 < a < a_c$, where $a_c > 0$ is the exponential decay rate of R_{tw} . It satisfies

$$\frac{2}{c(s)} \sqrt{1 + \frac{J(1 + e^\alpha)}{2(\cosh \alpha - \cosh a_c)}} \sinh \frac{a_c}{2} - a_c = 0 \quad (61)$$

For $J > 0$, we have $0 < a_c < \alpha$, with a_c tending to zero as $c \rightarrow c_s$ and to α as $c \rightarrow \infty$. At $J = 0$, a_c solves $2 \sinh(a_c/2) = a_c c(s)$ [21].

A.2 Multiplicity of the zero eigenvalue

We now differentiate (53) with respect to τ to obtain

$$\frac{d^2 R}{d\tau^2} = \frac{1}{c(s)} \mathcal{J} \frac{\partial^2 H}{\partial R^2} \frac{dR}{d\tau}. \quad (62)$$

Rearranging (62) and evaluating it at $R = R_{tw}$ then yields $\mathcal{L}(\partial_\tau R_{tw}) = 0$. Thus $e_0 := \partial_\tau R_{tw}$ is an eigenvector of \mathcal{L} with eigenvalue $\nu = 0$ if $e_0 \in D_{tw,a,a}^0([0, 1])$. Multiplying (53) by $c(s)$ and differentiating the result with respect to s , we obtain

$$c'(s) \partial_\tau R + c(s) \partial_s \partial_\tau R = \mathcal{J} \frac{\partial^2 H}{\partial R^2} \partial_s R$$

Evaluating this equation at $R = R_{tw}$, we obtain

$$\mathcal{L}(c(s) \partial_s R_{tw}) = c'(s) e_0, \quad (63)$$

which for $c'(s) \neq 0$ yields

$$\mathcal{L}(e_1) = e_0, \quad e_1 := \frac{c(s)}{c'(s)} \partial_s R_{tw}.$$

Thus e_1 is a generalized eigenvector of \mathcal{L} for eigenvalue $\nu = 0$ if $e_0, e_1 \in D_{tw,a,a}^0([0, 1])$. Here we assume

$$e_0, e_1 \in D_{tw,-a,-a}^0([0, 1]) \cap D_{tw,a,a}^0([0, 1]), \quad (64)$$

which holds when (positive) a is less than a_c , the exponential decay rate of R_{tw} , which for our problem solves (61). This assumption then implies that the multiplicity of eigenvalue $\nu = 0$ is always no less than two. To further investigate the multiplicity of the eigenvalue $\nu = 0$, we consider the adjoint of \mathcal{L} as

$$\mathcal{L}^* = \frac{d}{d\tau} - \frac{1}{c(s)} \frac{\partial^2 H}{\partial R^2} \Big|_{R=R_{tw}} \mathcal{J}, \quad (65)$$

on $D_{tw,-a,-a}^0([0, 1])$. Suppose that $\mathcal{L}_{-a,-a}$ has the same form of \mathcal{L} , but it is restricted on $D_{tw,-a,-a}^0([0, 1])$, the adjoint of \mathcal{L} for $Z \in D_{tw,-a,-a}^0([0, 1])$ can then be written as

$$\mathcal{L}^* Z = -\mathcal{J}_{-a,-a}^{-1} \mathcal{L}_{-a,-a} \mathcal{J} Z. \quad (66)$$

Consider the generic case when $c'(s) \neq 0$ and $\ker(\mathcal{L}) = \text{span}\{e_0\}$ and similarly $\ker(\mathcal{L}^*) = \text{span}\{\mathcal{J}_{-a,-a}^{-1} e_0\}$, where we note that $\mathcal{L}^*(\mathcal{J}_{-a,-a}^{-1} e_0) = 0$. From the definition of e_0 , it can be examined that

$$\mathcal{J}_{a,a}^{-1} e_0 = \mathcal{J}_{-a,-a}^{-1} e_0. \quad (67)$$

Since $\langle \mathcal{J}_{-a,-a}^{-1} e_0, e_0 \rangle = \langle e_0, \mathcal{J}_{a,a}^{-1} e_0 \rangle$, it follows $\langle \mathcal{J}_{-a,-a}^{-1} e_0, e_0 \rangle = 0$. When \mathcal{L} is defined on $D_{tw,a,a}^1([0, 1]) \subset D_{tw,a,a}^0([0, 1])$, where $0 < a < a_c$, with a_c defined in (61) for Hamiltonian (1), it is a densely-defined closed operator and the use of weighted spaces makes 0 outside the essential spectra of \mathcal{L} and \mathcal{L}^* . As a result, \mathcal{L} has closed range and $e_0 \in (\ker(\mathcal{L}^*))^\perp = \text{rng}(\mathcal{L})$. Hence there exists e_1 such that $\mathcal{L}(e_1) = e_0$. Since the energy of the system is conserved, we have that

$$H(s) = \int_0^1 H|_{R_{tw}(\tau;s)} d\tau.$$

We will use this to show that $H'(s) = 0$ if and only if $\langle \mathcal{J}_{-a,-a}^{-1} e_0, e_1 \rangle = 0$. Indeed,

$$\begin{aligned} 0 &= \langle e_1, \mathcal{J}_{-a,-a}^{-1} e_0 \rangle = \left\langle \frac{c(s)}{c'(s)} \partial_s R_{tw}, \mathcal{J}_{a,a}^{-1} \partial_\tau R_{tw} \right\rangle = \left\langle c(s) \partial_s R_{tw}, \frac{1}{c(s)} \frac{\partial H}{\partial R} \Big|_{R=R_{tw}} \right\rangle \frac{1}{c'(s)} \\ &= \frac{1}{c'(s)} \int_0^1 \partial_s R_{tw} \left(\frac{\partial H}{\partial R} \right) \Big|_{R=R_{tw}} d\tau = \frac{1}{c'(s)} \int_0^1 H'(s)|_{R=R_{tw}(\tau;s)} d\tau = \frac{H'(s)}{c'(s)} \end{aligned} \quad (68)$$

Thus, whenever $H'(s) = 0$, we have that $e_1 \in \text{rng}(\mathcal{L})$, and hence there exists e_2 satisfying $\mathcal{L}(e_2) = e_1$, implying that the algebraic multiplicity of $\nu = 0$ is at least three. Moreover, $\mathcal{L}^*(-\mathcal{J}_{-a,-a}^{-1} e_1) = \mathcal{J}_{-a,-a}^{-1} \mathcal{L} \mathcal{J}_{-a,-a}^{-1} e_1 = \mathcal{J}_{-a,-a}^{-1} e_0$ implies that

$$\langle \mathcal{J}_{-a,-a}^{-1} e_0, e_2 \rangle = \langle -\mathcal{L}^* \mathcal{J}_{-a,-a}^{-1} e_1, e_2 \rangle = \langle \mathcal{J}_{-a,-a}^{-1} e_1, \mathcal{L} e_2 \rangle = \langle \mathcal{J}_{-a,-a}^{-1} e_1, e_1 \rangle. \quad (69)$$

Since in general

$$\begin{pmatrix} \sum_{k=-\infty}^{\infty} e^{k\partial} & 0 \\ 0 & \sum_{k=-\infty}^{\infty} e^{k\partial} \end{pmatrix} e_1 \neq 0,$$

we have $\langle \mathcal{J}_{-a,-a}^{-1} e_1, e_1 \rangle \neq 0$, and hence the multiplicity of the eigenvalue $\nu = 0$ is at most three.

The change of multiplicity of $\nu = 0$ from two to three suggests that $s = s_0$ such that $H'(s_0) = 0$ corresponds to a stability threshold. The fact that the multiplicity at the threshold becomes three and not four, as suggested by our numerical computations that show collision of eigenvalue pairs typical for Hamiltonian systems [129], is the consequence of the use of the weighted spaces in the strain formulation that destroys the Hamiltonian structure of the problem. In contrast, in [32], where the Hamiltonian structure was preserved, the eigenvalue zero splits as $\nu \sim \sqrt{c - c_0}$ near the critical speed c_0 in when $H''(c_0) \neq 0$ and $\nu = 0$ has multiplicity four at $c = c_0$. Due to the similarity between \mathcal{J} in our problem and ∂_x in [130], a possible scenario for stability change in the present setting is a resonance pole (a pole of the analytic continuation of the resolvent) moving across the imaginary

axis as s crosses s_0 from the upper sheet of the Riemann surface for the resolvent to the lower sheet and emerging as a real positive eigenvalue during the transition from stability to instability [130]. This implies that although the zero eigenvalue has an odd multiplicity at $s = s_0$ in current space, the multiplicity could be even in a larger space. In fact, our numerical computation of the eigenvalues near s_0 shows that the eigenvalue splitting is in the form $\nu \sim \sqrt{s - s_0}$ (see Fig. 10). That is to say, the Hamiltonian symmetry can be retained under certain circumstances, and we will provide an explanation for that below.

A.3 Numerical implementations and Hamiltonian symmetry

It should be noted that the results of the numerical eigenvalue problem very much depend on the choices in its implementation. For instance, if we consider a finite chain in the numerical calculation and discretize the variables in time, then the operators such as \mathcal{J} , $\frac{d}{d\tau}$ and \mathcal{L} are represented by matrices $[\mathcal{J}]$, $[\frac{d}{d\tau}]$ and $[\mathcal{L}]$, respectively. In particular, if the matrices for \mathcal{J} and $\frac{d}{d\tau}$ are invertible and skew-symmetric, say,

$$\left[\frac{d}{d\tau}\right] = \begin{pmatrix} D & \\ & D \end{pmatrix}, \quad D = \frac{1}{2\Delta\tau} \begin{pmatrix} 0 & 1 & & & \\ -1 & 0 & 1 & & \\ & \cdots & \cdots & \cdots & \\ & & -1 & 0 & 1 \\ & & & -1 & 0 \end{pmatrix},$$

$$[\mathcal{J}] = \begin{pmatrix} 0 & J_1 \\ -J_1^T & 0 \end{pmatrix}, \quad J_1 = \begin{pmatrix} -1 & 0 & \cdots & 0 & 1 \\ & -1 & 0 & \cdots & 0 & 1 \\ & & \cdots & \cdots & \cdots & \cdots \\ & & & \cdots & \cdots & \cdots & \cdots \\ & & & & -1 & 0 & \cdots & 0 & 1 \\ & & & & & -1 & 0 & \cdots & 0 \\ & & & & & & -1 & 0 & \cdots \\ & & & & & & & \cdots & \cdots \\ & & & & & & & & -1 \end{pmatrix}$$

and

$$[\mathcal{J}^{-1}] = [\mathcal{J}]^{-1} = \begin{pmatrix} 0 & -(J_1^T)^{-1} \\ (J_1)^{-1} & 0 \end{pmatrix},$$

then naturally $[\mathcal{J}^{-1}]$ is also skew-symmetric and the multiplicity of zero eigenvalue for $[\mathcal{L}]$ will be even.

As another example, suppose we consider a finite cyclic chain and choose $[\mathcal{J}]$, $[\frac{d}{d\tau}]$ and $[\mathcal{L}]$ so that their kernels contain $\begin{pmatrix} c_1 \mathbf{1} \\ c_2 \mathbf{1} \end{pmatrix}$. Since this is a finite chain, if $[\mathcal{L}]e_0 = 0$ and $[\mathcal{L}]e_1 = e_0$, we can choose c_1 and c_2 such that $\tilde{e}_1 = \begin{pmatrix} \tilde{e}_1^{(1)} \\ \tilde{e}_1^{(2)} \end{pmatrix} = e_1 - \begin{pmatrix} c_1 \mathbf{1} \\ c_2 \mathbf{1} \end{pmatrix}$ satisfies $\sum_{k=-\infty}^{\infty} \tilde{e}_{1,k}^{(1)} = \sum_{k=-\infty}^{\infty} \tilde{e}_{1,k}^{(2)} = 0$. Observe that violation of this condition causes the zero eigenvalue to have odd multiplicity in the above discussion. In this setting, we consider the equivalence classes $\{\tilde{e}\}$ modulo $\begin{pmatrix} c_1 \mathbf{1} \\ c_2 \mathbf{1} \end{pmatrix}$ with representatives $\tilde{e} = \begin{pmatrix} \tilde{e}^{(1)} \\ \tilde{e}^{(2)} \end{pmatrix}$ satisfying $\sum_{k=-\infty}^{\infty} \tilde{e}_k^{(1)} = \sum_{k=-\infty}^{\infty} \tilde{e}_k^{(2)} = 0$. This way we can make $[\mathcal{J}^{-1}]$ skew-symmetric, and hence the zero eigenvalue of $[\mathcal{L}]$ should have even multiplicity.

These two examples illustrate how Hamiltonian symmetry can be retained in a finite-dimensional implementation. A full characterization of the eigenvalues near zero in different spaces is beyond the scope of this work and is left for future investigations.

Appendix B

B.1 Additional traveling breather solutions

Investigations of the resonances suggest that a second set of solutions coexists along with the solutions discussed in Chapter 2. These additional solutions can be found by employing a method similar to the one described in Sec. 3.2 for obtaining moving breathers from stationary breathers. By scaling the momentum vector of the moving breather solution and using this scaled momentum along with the unscaled displacement vector as an initial guess, Newton's method can be employed to obtain these secondary solution branches. The primary and secondary solutions typically differ in how the Floquet multipliers at the origin evolve after a resonance. In what follows, these dual solution sets are examined for the middle branch near the resonance at $\omega = 2.352$ when $N = 60$ and $V_1 = 1/3$.

An example of this systematic comparison can be seen in Fig. 39. Panels (a), (d) and (g) of Fig. 39 show the energy-frequency dependence along the two different solution branches (blue and red) near the resonance frequency. As the amplitude of the wings increases, the gap between the two solutions increases as well. Panels (b), (e) and (h) compare the displacements of the two solutions with the same energy (shown by horizontal line in panels (a), (d) and (g), respectively) and slightly different frequency. Note that the wings appear to be essentially in phase with each other. We emphasize that the two solutions are not simply different time snapshots of the same breather. This can be seen by observing the difference in the Floquet multipliers near unity. The multipliers are depicted in panels (c), (f) and (i) for the pairs of solutions shown in panels (b), (e) and (h), respectively. Note that for the blue branch we see the emergence of two real Floquet multipliers that separate from the ones at $\mu = 1$. However, for the red branch, the Floquet multipliers that leave $\mu = 1$ move along the unit circle (rather than the real axis). Thus, one solution branch develops an exponential instability associated with a small real multiplier, while the other does not. This is reminiscent of the commensurability effect discussed in Chapter 4 of [74] (see, for example, Fig. 4.11 therein).

In Fig. 40, the dependence of the energy H and maximum real Floquet multipliers μ on the breather frequency is shown near the turning point connecting the middle and bottom branches. The colors in each figure correspond to those used in Fig. 39. As can be seen, while the real Floquet multipliers along the red branch, in which the Floquet multipliers emerge along the unit circle, are

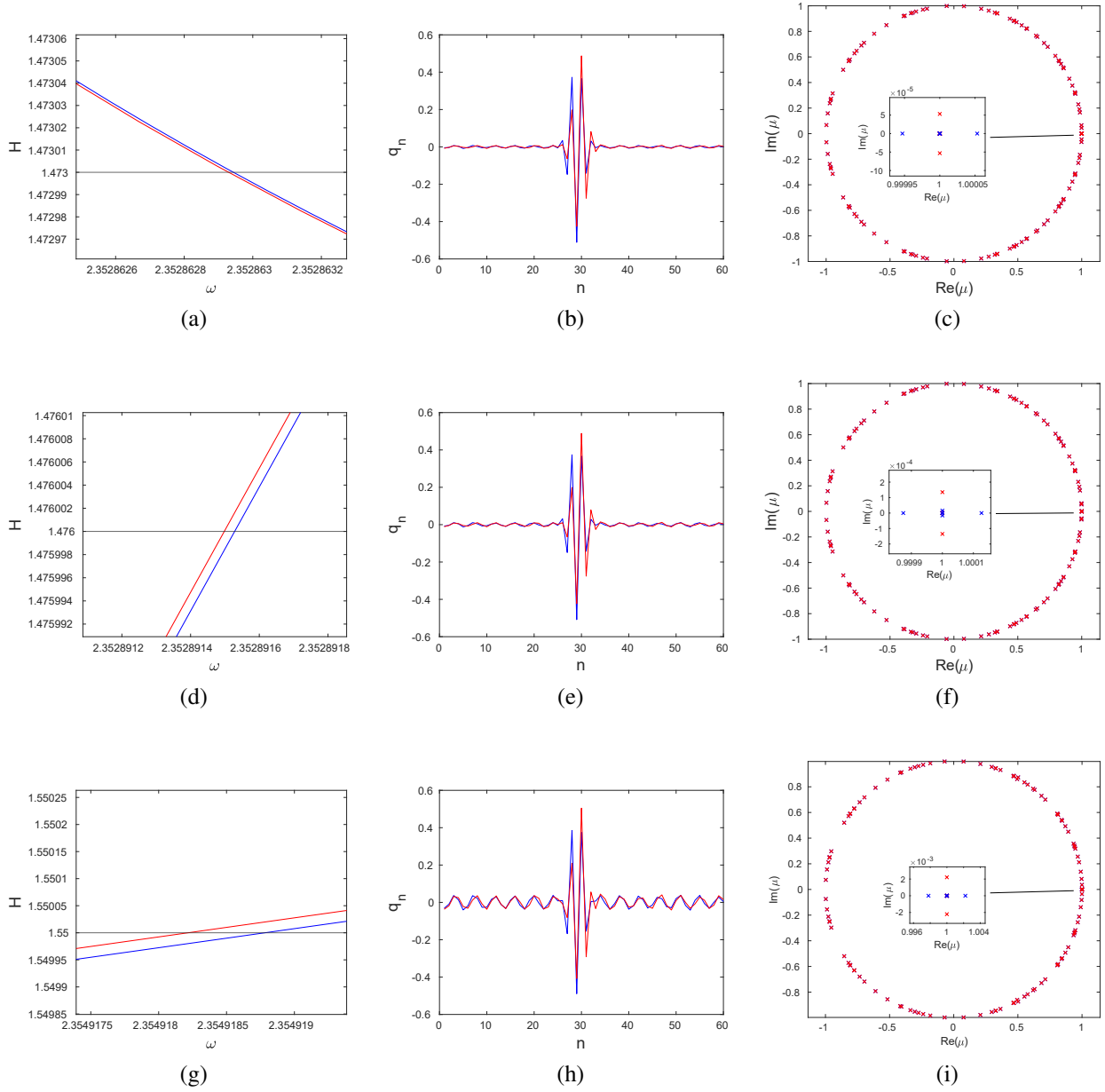


Figure 39: Coexisting solutions. Panels (a), (d) and (g) show the energy H versus frequency ω along two coexisting solution branches, red and blue, near the resonance at $\omega = 2.352$. The horizontal black line marks the energy of the two solutions whose displacements q_n are compared in panels (b), (e) and (h), respectively. Panels (c), (f) and (i) show the corresponding Floquet multipliers, with insets zooming in on the multipliers near $\mu = 1$. In each case, a pair of Floquet multipliers is separating from $\mu = 1$. Here $V_1 = 1/3$ and $N = 60$.

staying close to $\mu = 1$, the largest real Floquet multiplier along the blue branch increases steadily as the energy increases. It should be explicitly mentioned here that the energy of the two branches

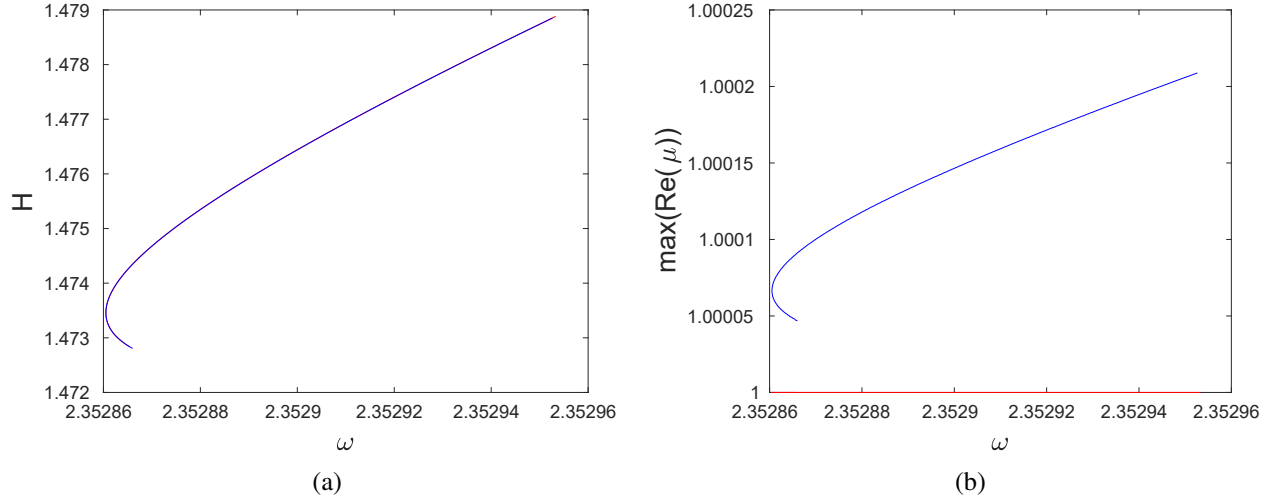


Figure 40: (a) Energy H versus frequency ω and (b) the maximum real Floquet multipliers μ along the two solutions near the resonance at $\omega = 2.352$. The colors correspond to those used in Fig. 39. Here $V_1 = 1/3$ and $N = 60$. In the left panel the blue and red branches cannot be distinguished over the scale of the figure (see also the magnified pictures in the left panels of Fig. 39).

cannot be distinguished over the scale of the left panel.

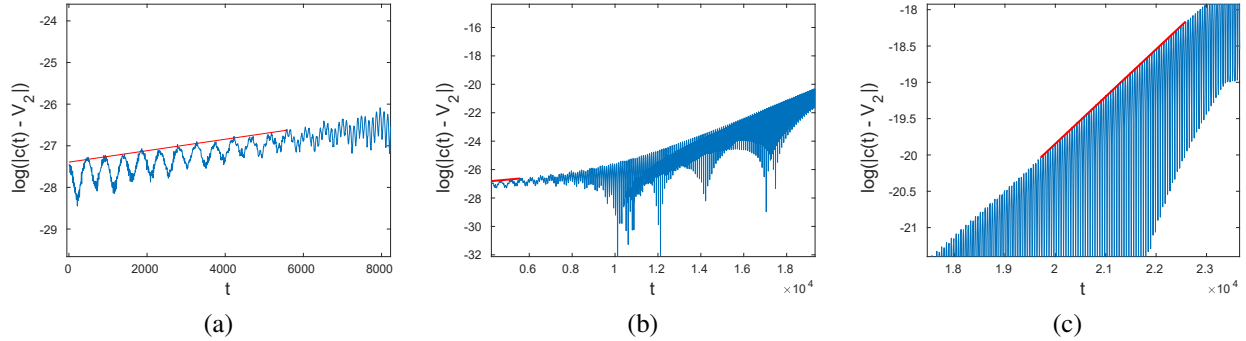


Figure 41: Time evolution of the absolute difference between the computed speed c and the initial translational velocity $V_2 = 1/(3T)$ for the moving breather with the largest real Floquet multiplier $\mu = 1.0023$ perturbed along the corresponding unstable eigenmode. Panels (a) and (c) show the early and late stages of the evolution, while panel(b) depicts over the entire time span. The maximum modulus of the Floquet multipliers is $|\mu| = 1.0104$. In panels (a) and (c), the red lines correspond to the best linear fit measuring the growth rate of the wave. The line in panel (a) measures the initial growth due to the exponential instability, and the second line measures the growth due to the oscillatory instability. In panel (b), the darker region corresponds to the emergence of the oscillatory instability as the main factor in the growth of the perturbed moving breather. Here $N = 60$, $\omega = 2.355$, $V_1 = 1/3$, and the strength of the perturbation is $\epsilon = 10^{-7}$.

A key question is whether the exponential instability seen along the blue branch is a true insta-

bility given its relatively small size. To examine this, we perturbed a selected moving breather along its real unstable eigenmode with a perturbation strength $\epsilon = 10^{-7}$, as explained in Sec. 3.4. Here, $\mu = 1.0023$ is the largest real multiplier, $V_1 = 1/3$ and $\omega = 2.355$. In Fig. 41, we show a semilogarithmic plot of the time evolution of the absolute difference of the computed velocity c and the initial translational velocity $V_2 = 1/(3T)$. As can be seen, the growth of the perturbed moving breather has two regimes. The first, shown in Fig. 41(a), is dominated by the exponential instability associated with an eigenmode along which the dynamics was initially perturbed. The second, depicted in Fig. 41(c), is determined by the maximal-modulus Floquet multipliers $\mu = 0.5034 \pm 0.8761i$ with $|\mu| = 1.0104$. The middle panel of Fig. 41(b) captures the transition from the former to the latter. We note that this is different from the example shown in Sec. 3.4, where the real Floquet multiplier corresponding to the eigenmode along which the moving breather was perturbed also had the largest modulus among the Floquet multipliers. The red lines in panels (a) and (c) measure the growth rate and have the slope $\ln(|\mu|)/(6T)$, where μ is the corresponding multiplier and we have used the fact that $V_1 = 1/3$ for the unperturbed breather. Comparing the lines of growth rate for maximum real multiplier and the complex multiplier with maximum modulus to the early and late stages, respectively, of the evolution in the simulation results yields an absolute difference of size $O(10^{-5})$ in both cases, indicating that the two regimes are indeed dominated by the two distinct types of instability. At later times, the velocity evolution is similar to that for the examples discussed in Sec. 3.4. In short, this detailed examination of the associated dynamical evolution reveals that the instability growth rates captured by our Floquet analysis, even when very small, accurately reflect the instability features of the associated solutions and hence appear to be real features of the wave dynamics.

B.2 Effect of the lattice size

In this Appendix we discuss the effect of the lattice size N on the structure of the moving breathers constructed in Chapter 3. Profiles of displacements q_n and energy density e_n at $N = 60$ and $N = 180$ are compared in panels (a) and (b), respectively, of Fig. 42-44, which show the results for $V_1 = 1/2$ and three different frequencies, $\omega = 2.19$, $\omega = 2.37$, and $\omega = 2.49$, from across the spectrum typically considered in the simulations we have performed. One can see that the lattice size mainly affects the wing amplitude, which is consistent with the number of resonances increasing with N . Meanwhile,

the core structure of the breather barely changes as N is increased. The maximum relative difference between the energy densities of the central 60 sites is approximately 0.0121 at $\omega = 2.37$, the case in which the difference in the wing amplitude of the two solutions is most pronounced (see Fig. 43), $5.7057 \cdot 10^{-5}$ at $\omega = 2.19$ (Fig. 42) and 0.0045 at $\omega = 2.49$ (Fig. 44).

The total energy at $\omega = 2.37$ is $H = 1.4729$ for $N = 60$ and $H = 1.476$ for $N = 180$ respectively. We attribute this slight increase in energy for $N = 180$ to the fact that the wings have larger amplitude and are more extended in this case. The wing energy is 0.0193% of the total energy for $N = 60$ and 0.2064% for $N = 180$. However, the amounts of energy retained in the core differ only slightly for $N = 60$ and $N = 180$. More precisely, the core energy is 1.4726 for $N = 60$ and 1.473 for $N = 180$. This corresponds to a relative difference of 0.0227% between the core energies for the two lattice sizes. When the wing amplitude is smaller, as in the other two cases we examined, the difference is even smaller.

Finally, we remark that perturbing one of the unstable moving breathers for the case $N = 180$ and simulating its dynamics over a long period of time, we observe a similar evolution as that seen in the $N = 60$ case, wherein the velocity decreases to 0 before oscillating around that point. The time scale over which this slowing down takes place is longer than in the $N = 60$ case. This is to be expected, given that the expelled waves must travel a longer distance before interacting with the core in the $N = 180$ case.

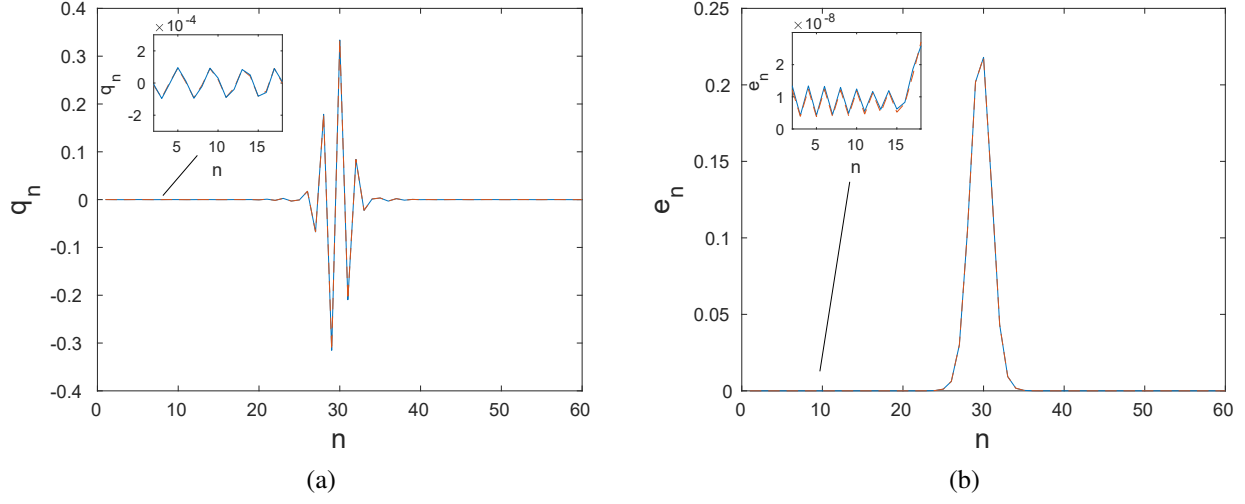


Figure 42: Profiles of (a) displacement q_n and (b) energy density e_n of a moving breather with $N = 60$ (solid blue) and $N = 180$ (dash-dotted red) of the central 60 sites. Here $\omega = 2.19$ and $V_1 = 1/2$. The inset in each panel shows a segment of the wings of the two solutions.

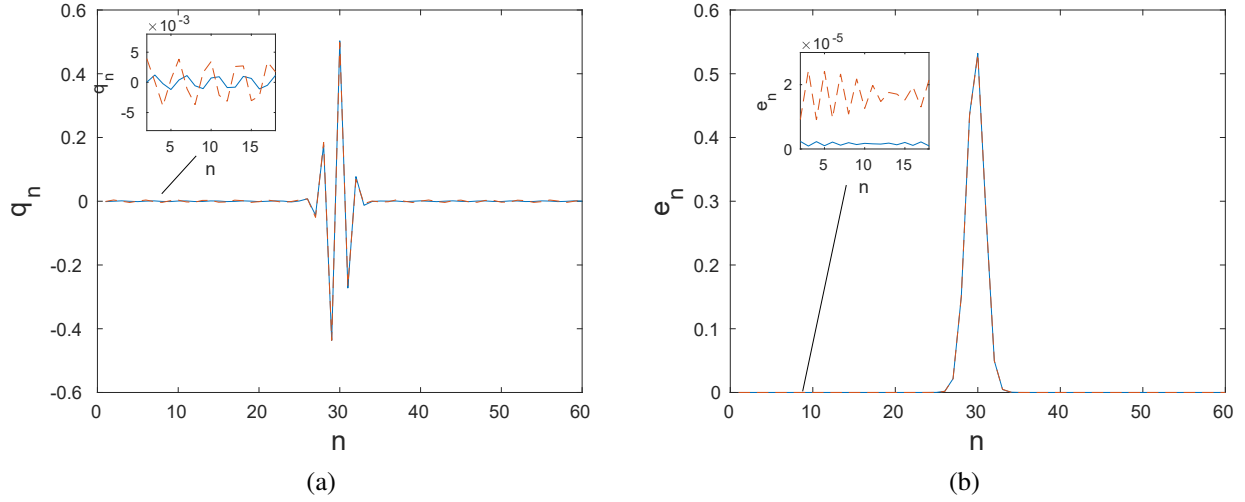


Figure 43: Profiles of (a) displacement q_n and (b) energy density e_n of a moving breather with lattice size $N = 60$ (solid blue) and $N = 180$ (dash-dotted red) of the central 60 sites. Here $\omega = 2.37$ and $V_1 = 1/2$. The inset in each panel shows a segment of the wings of the two solutions.

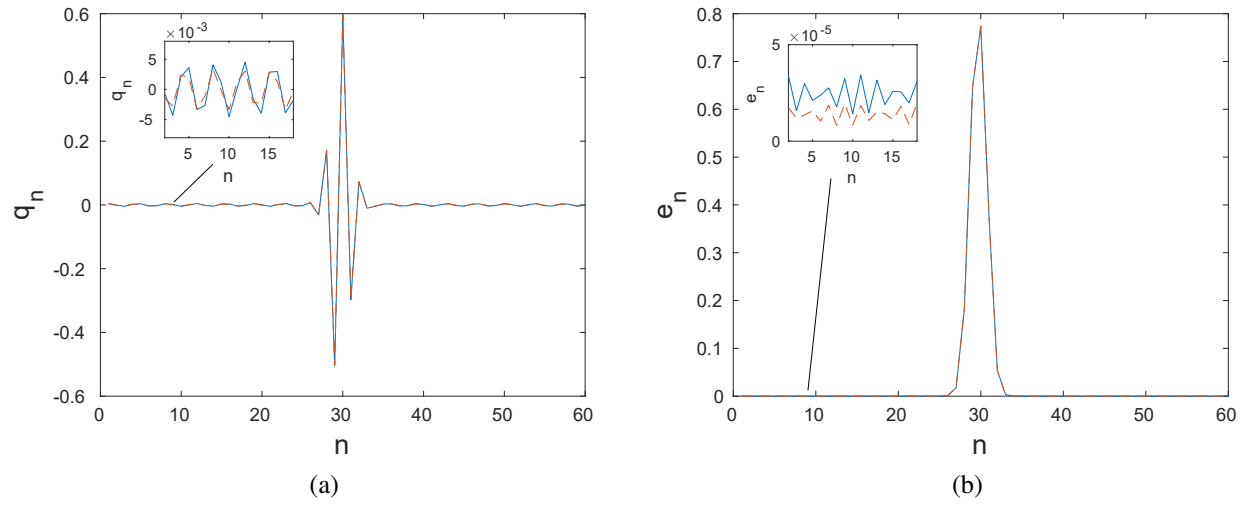


Figure 44: Profiles of (a) displacement q_n and (b) energy density e_n of a moving breather with $N = 60$ (solid blue) and $N = 180$ (dash-dotted red) of the central 60 sites. Here $\omega = 2.49$ and $V_1 = 1/2$. The inset in each panel shows a zoomed in view of the wings of the two solutions.

Bibliography

- [1] E. Fermi, J. Pasta, and S. Ulam. Studies of nonlinear problems. Technical Report LA-1940, Los Alamos Scientific Laboratory, 1955.
- [2] N. J. Zabusky and M. D. Kruskal. Interaction of solitons in a collisionless plasma and the recurrence of initial states. *Phys. Rev. Lett.*, 15(6):240–243, 1965.
- [3] A. A. Pankov. *Travelling waves and periodic oscillations in Fermi-Pasta-Ulam lattices*. Imperial College Press, 2005.
- [4] S. Sen, J. Hong, J. Bang, E. Avalos, and R. Doney. Solitary waves in the granular chain. *Phys. Rep.*, 462(2):21–66, 2008.
- [5] P. G. Kevrekidis. Non-linear waves in lattices: past, present, future. *IMA J. Appl. Math.*, 76(3):1–35, 2011.
- [6] C. Chong, M. A. Porter, P. G. Kevrekidis, and C. Daraio. Nonlinear coherent structures in granular crystals. *J. Phys.*, 29(41):413003, 2017.
- [7] A. Vainchtein. Solitary waves in FPU-type lattices. *Physica D*, page 133252, 2022.
- [8] R. Hirota and K. Suzuki. Theoretical and experimental studies of lattice solitons in nonlinear lumped networks. *Proc. IEEE*, 61(10):1483–1491, 1973.
- [9] T. Kofane, B. Michaux, and M. Remoissenet. Theoretical and experimental studies of diatomic lattice solitons using an electrical transmission line. *J. Phys. C*, 21(8):1395, 1988.
- [10] C. Coste, E. Falcon, and S. Fauve. Solitary waves in a chain of beads under Hertz contact. *Phys. Rev. E*, 56:6104–6117, 1997.
- [11] V. Nesterenko. *Dynamics of heterogeneous materials*. Springer, 2001.
- [12] E. Kim, R. Chaunsali, H. Xu, J. Jaworski, J. Yang, P. G. Kevrekidis, and A. F. Vakakis. Non-linear low-to-high-frequency energy cascades in diatomic granular crystals. *Phys. Rev. E*, 92(6):062201, 2015.

- [13] H. Yasuda, Y. Miyazawa, E. G. Charalampidis, C. Chong, P. G. Kevrekidis, and J. Yang. Origami-based impact mitigation via rarefaction solitary wave creation. *Sci. Adv.*, 5(5):eaau2835, 2019.
- [14] M. Toda. *Theory of nonlinear lattices*. Springer, Berlin, 1981.
- [15] G. Friesecke and J. A. D. Wattis. Existence theorem for solitary waves on lattices. *Commun. Math. Phys.*, 161(2):391–418, 1994.
- [16] D. Smets and M. Willem. Solitary waves with prescribed speed on infinite lattices. *J. Funct. Anal.*, 149(1):266, 1997.
- [17] A. Pankov and V. M. Rothos. Traveling waves in Fermi-Pasta-Ulam lattices with saturable nonlinearities. *Discr. Cont. Dyn. Syst. A*, 30(3):835–849, 2011.
- [18] A. Stefanov and P. Kevrekidis. On the existence of solitary traveling waves for generalized hertzian chains. *J. of Non. Sci.*, 22(3):327–349, 2012.
- [19] G. Friesecke and R. L. Pego. Solitary waves on Fermi-Pasta-Ulam lattices: I. Qualitative properties, renormalization and continuum limit. *Nonlinearity*, 12:1601–1626, 1999.
- [20] G. Friesecke and R. L. Pego. Solitary waves on Fermi-Pasta-Ulam lattices: II. Linear implies nonlinear stability. *Nonlinearity*, 15(4):1343–1359, 2002.
- [21] G. Friesecke and R. L. Pego. Solitary waves on Fermi-Pasta-Ulam lattices: III. Howland-type Floquet theory. *Nonlinearity*, 17:202–207, 2004.
- [22] G. Friesecke and R. L. Pego. Solitary waves on Fermi-Pasta-Ulam lattices: IV. Proof of stability at low energy. *Nonlinearity*, 17(1):229–251, 2004.
- [23] G. Iooss. Travelling waves in the Fermi-Pasta-Ulam lattice. *Nonlinearity*, 13(3):849, 2000.
- [24] E. McMillan. Multiscale correction to solitary wave solutions on FPU lattices. *Nonlinearity*, 15(5):1685–1697, 2002.
- [25] A. Hoffman and C. Wayne. A simple proof of the stability of solitary waves in the Fermi-Pasta-Ulam model near the KdV limit. In *Infinite dimensional dynamical systems*, pages 185–192. Springer, 2013.

- [26] G. Friesecke and K. Matthies. Atomic-scale localization of high-energy solitary waves on lattices. *Physica D*, 171:211–220, 2002.
- [27] M. Herrmann and K. Matthies. Asymptotic formulas for solitary waves in the high-energy limit of FPU-type chains. *Nonlinearity*, 28(8):2767, 2015.
- [28] M. Herrmann and K. Matthies. Stability of high-energy solitary waves in Fermi-Pasta-Ulam-Tsingou chains. *Trans. Amer. Math. Soc.*, 372(5):3425–3486, 2019.
- [29] T. Mizumachi and R. L. Pego. Asymptotic stability of Toda lattice solitons. *Nonlinearity*, 21(9):2099, 2008.
- [30] G. N. Benes, A. Hoffman, and C. E. Wayne. Asymptotic stability of the Toda m-soliton. *J. Math. Anal. Appl.*, 386(1):445–460, 2012.
- [31] J. Cuevas-Maraver, P. Kevrekidis, A. Vainchtein, and H. Xu. Unifying perspective: Hamiltonian lattice traveling waves as discrete breathers and energy criteria for their stability. *Phys. Rev. E*, 96:032214, 2017.
- [32] H. Xu, J. Cuevas-Maraver, P. G. Kevrekidis, and A. Vainchtein. An energy-based stability criterion for solitary travelling waves in Hamiltonian lattices. *Phil. Trans. R. Soc. A*, 376(2117):20170192, 2018.
- [33] P. G. Kevrekidis, J. Cuevas-Maraver, and D. E. Pelinovsky. Energy criterion for the spectral stability of discrete breathers. *Phys. Rev. Lett.*, 117:094101, Aug 2016.
- [34] L. Truskinovsky and A. Vainchtein. Solitary waves in a nonintegrable Fermi-Pasta-Ulam chain. *Phys. Rev. E*, 90(4):042903, 2014.
- [35] L. Truskinovsky and A. Vainchtein. Strictly supersonic solitary waves in lattices with second-neighbor interactions. *Phys. D*, 389:24–50, 2019.
- [36] S. Katz and S. Givli. Solitary waves in a bistable lattice. *Extr. Mech. Lett.*, 22:106–111, 2018.
- [37] S. Katz and S. Givli. Solitary waves in a nonintegrable chain with double-well potentials. *Phys. Rev. E*, 100(3):032209, 2019.
- [38] A. Neuper, Y. Gaididei, N. Flytzanis, and F. Mertens. Solitons in atomic chains with long-range interactions. *Phys. Lett. A*, 190(2):165–171, 1994.

- [39] Y. Gaididei, N. Flytzanis, A. Neuper, and F. G. Mertens. Effect of nonlocal interactions on soliton dynamics in anharmonic lattices. *Phys. Rev. Lett.*, 75(11):2240–2243, 1995.
- [40] Y. Gaididei, N. Flytzanis, A. Neuper, and F. G. Mertens. Effect of non-local interactions on soliton dynamics in anharmonic chains: Scale competition. *Physica D*, 107(1):83–111, 1997.
- [41] S. F. Mingaleev, Y. B. Gaididei, and F. G. Mertens. Solitons in anharmonic chains with ultra-long-range interatomic interactions. *Phys. Rev. E*, 61(2):R1044–1047, 2000.
- [42] G. A. Baker Jr. One-dimensional order-disorder model which approaches a second-order phase transition. *Phys. Rev.*, 122(5):1477–1484, 1961.
- [43] M. Kac and E. Helfand. Study of several lattice systems with long-range forces. *J. Math. Phys.*, 4(8):1078–1088, 1961.
- [44] K. S. Viswanathan and D. H. Mayer. Statistical mechanics of one-dimensional Ising and Potts models with exponential interactions. *Phys. A*, 89(1):97–112, 1977.
- [45] S. K. Sarker and J. A. Krumhansl. Effect of solitons on the thermodynamic properties of a system with long-range interactions. *Phys. Rev. B*, 23(5):2374, 1981.
- [46] H. Duran, H. Xu, P. G. Kevrekidis, and A. Vainchtein. Unstable dynamics of solitary traveling waves in a lattice with long-range interactions. *Wave Motion*, 108:102836, 2022.
- [47] H. B. Keller. *Lectures on Numerical Methods in Bifurcation Problems*. Springer-Verlag, New York, 1986.
- [48] S. Aubry. Breathers in nonlinear lattices: Existence, linear stability and quantization. *Physica D*, 103(1-4):201–250, 1997.
- [49] S. Aubry. Discrete breathers: localization and transfer of energy in discrete Hamiltonian nonlinear systems. *Physica D*, 216(1):1–30, 2006.
- [50] S. Flach and A. V. Gorbach. Discrete breathers – advances in theory and applications. *Phys. Rep.*, 467(1-3):1–116, 2008.
- [51] A. J. Sievers and S. Takeno. Intrinsic localized modes in anharmonic crystals. *Phys. Rev. Lett.*, 61(8):970–973, 1988.

- [52] J. B. Page. Asymptotic solutions for localized vibrational modes in strongly anharmonic periodic systems. *Phys. Rev. B*, 41(11):7835–7387, 1990.
- [53] K. W. Sandusky, J. B. Page, and K. E. Schmidt. Stability and motion of intrinsic localized modes in nonlinear periodic lattices. *Phys. Rev. B*, 46(10):6161–6168, 1992.
- [54] P. Binder, D. Abraimov, A. V. Ustinov, S. Flach, and Y. Zolotaryuk. Observation of breathers in Josephson ladders. *Phys. Rev. Lett.*, 84(4):745, 2000.
- [55] E. Trías, J. J. Mazo, and T. P. Orlando. Discrete breathers in nonlinear lattices: Experimental detection in a Josephson array. *Phys. Rev. Lett.*, 84(4):741, 2000.
- [56] J. Cuevas, L. Q. English, P. G. Kevrekidis, and M. Anderson. Discrete breathers in a forced-damped array of coupled pendula: modeling, computation, and experiment. *Phys. Rev. Lett.*, 102(22):224101, 2009.
- [57] F. Palmero, L. Q. English, J. Cuevas, R. Carretero-González, and P. G. Kevrekidis. Discrete breathers in a nonlinear electric line: Modeling, computation, and experiment. *Phys. Rev. E*, 84(2):026605, 2011.
- [58] L. Q. English, F. Palmero, J. F. Stormes, J. Cuevas, R. Carretero-González, and P. G. Kevrekidis. Nonlinear localized modes in two-dimensional electrical lattices. *Phys. Rev. E*, 88(2):022912, 2013.
- [59] M. Remoissenet. *Waves Called Solitons*. Springer-Verlag, Berlin, 1999.
- [60] M. Sato, B. E. Hubbard, A. J. Sievers, B. Ilic, D. A. Czaplewski, and H. G. Craighead. Observation of locked intrinsic localized vibrational modes in a micromechanical oscillator array. *Phys. Rev. Lett.*, 90(4):044102, 2003.
- [61] M. Sato, B. E. Hubbard, A. J. Sievers, B. Ilic, and H. G. Craighead. Optical manipulation of intrinsic localized vibrational energy in cantilever arrays. *EPL*, 66(3):318, 2004.
- [62] M. Sato, B. E. Hubbard, and A. J. Sievers. Colloquium: Nonlinear energy localization and its manipulation in micromechanical oscillator arrays. *Rev. Mod. Phys.*, 78:137–157, Jan 2006.
- [63] M. Peyrard. Nonlinear dynamics and statistical physics of DNA. *Nonlinearity*, 17:R1, 2004.

- [64] N. Boechler, G. Theocharis, S. Job, P. G. Kevrekidis, M. A. Porter, and C. Daraio. Discrete breathers in one-dimensional diatomic granular crystals. *Phys. Rev. Lett.*, 104(24):244302, 2010.
- [65] C. Chong, F. Li, J. Yang, M. O. Williams, I. G. Kevrekidis, P. G. Kevrekidis, and C. Daraio. Damped-driven granular chains: An ideal playground for dark breathers and multibreathers. *Phys. Rev. E*, 89(3):032924, 2014.
- [66] Y. Zhang, D. M. McFarland, and A. F. Vakakis. Propagating discrete breathers in forced one-dimensional granular networks: theory and experiment. *Granul. Matter*, 19(3):1–22, 2017.
- [67] C. Chong and P. G. Kevrekidis. *Coherent Structures in Granular Crystals: From Experiment and Modelling to Computation and Mathematical Analysis*. Springer, New York, 2018.
- [68] A. A. Ovchinnikov. Localized long-lived vibrational states in molecular crystals. *Sov. Phys. JETP*, 30(1):147–150, 1970.
- [69] P. G. Kevrekidis, J. Cuevas-Maraver, and D. E. Pelinovsky. Energy criterion for the spectral stability of discrete breathers. *Phys. Rev. Lett.*, 117:094101, 2016.
- [70] J. Cuevas-Maraver, P. G. Kevrekidis, and D. E. Pelinovsky. Nonlinear instabilities of multi-site breathers in Klein-Gordon lattices. *Stud. Appl. Math.*, 137(2):214–237, 2016.
- [71] V. M. Burlakov, S. A. Kiselev, and V. N. Pyrkov. Computer simulation of intrinsic localized modes in one-dimensional and two-dimensional anharmonic lattices. *Phys. Rev. B*, 42(8):4921, 1990.
- [72] K. Hori and S. Takeno. Moving self-localized modes for the displacement field in a one-dimensional lattice system with quartic anharmonicity. *J. Phys. Soc. Japan*, 61(7):2186–2189, 1992.
- [73] D. Chen, S. Aubry, and G. P. Tsironis. Breather mobility in discrete ϕ^4 nonlinear lattices. *Phys. Rev. Lett.*, 77:4776–4779, 1996.
- [74] T. Cretegny. *Collective dynamics and localization of energy in nonlinear networks*. PhD thesis, ENS Lyon, Lyon, France, 1998.
- [75] G. Kopidakis, S. Aubry, and G. P. Tsironis. Targeted energy transfer through discrete breathers in nonlinear systems. *Phys. Rev. Lett.*, 87:165501, Sep 2001.

- [76] S. Aubry and T. Cretegny. Mobility and reactivity of discrete breathers. *Physica D*, 119(1-2):34–46, 1998.
- [77] J. F. R Archilla, Y. Doi, and M. Kimura. Pterobreathers in a model for a layered crystal with realistic potential: Exact moving breathers in a moving frame. *Phys. Rev. E*, 100:022206, 2019.
- [78] K. Yoshimura and Y. Doi. Moving discrete breathers in a nonlinear lattice: Resonance and stability. *Wave Motion*, 45:83–99, 2007.
- [79] Y. Doi and K. Yoshimura. Symmetric potential lattice and smooth propagation of tail-free discrete breathers. *Phys. Rev. Lett.*, 117(1):014101, 2016.
- [80] Y. Doi and K. Yoshimura. Construction of nonlinear lattice with potential symmetry for smooth propagation of discrete breather. *Nonlinearity*, 33(10):5142, 2020.
- [81] H. Duran, J. Cuevas-Maraver, P. G. Kevrekidis, and A. Vainchtein. Moving discrete breathers in a β -FPU lattice revisited. *Commun. Nonlin. Sci. Numer. Simul.*, 111:106435, 2022.
- [82] M. P. Calvo and J. M. Sanz-Serna. The development of variable-step symplectic integrators, with application to the two-body problem. *Siam J. on Sci. Comp.*, 14(4):936–952, 1993.
- [83] K. Bertoldi, V. Vitelli, J. Christensen, and M. Van Hecke. Flexible mechanical metamaterials. *Nature Rev. Mater.*, 2(11):1–11, 2017.
- [84] Z. Chen, B. Guo, Y. Yang, and C. Cheng. Metamaterials-based enhanced energy harvesting: A review. *Physica B*, 438:1–8, 2014.
- [85] J. Christensen, M. Kadic, O. Kraft, and M. Wegener. Vibrant times for mechanical metamaterials. *MRS Commun.*, 5(3):453–462, 2015.
- [86] L. Wu, Y. Wang, K. Chuang, F. Wu, Q. Wang, W. Lin, and H. Jiang. A brief review of dynamic mechanical metamaterials for mechanical energy manipulation. *Mater. Today*, 44:168–193, 2021.
- [87] S. Dalela, P. S. Balaji, and D. P. Jena. A review on application of mechanical metamaterials for vibration control. *Mech. Adv. Mater. Struct.*, 28:1–26, 2021.
- [88] A. A. Zadpoor. Mechanical meta-materials. *Mater. Horiz.*, 3:371–381, 2016.

- [89] A. Clausen, F. Wang, J. S. Jensen, O. Sigmund, and J. A. Lewis. Topology optimized architectures with programmable Poisson’s ratio over large deformations. *Adv. Mater.*, 27(37):5523–5527, 2015.
- [90] M. I. Hussein, M. J. Leamy, and M. Ruzzene. Dynamics of phononic materials and structures: Historical origins, recent progress, and future outlook. *Appl. Mech. Rev.*, 66(4), 2014.
- [91] D. M. Kochmann and K. Bertoldi. Exploiting microstructural instabilities in solids and structures: from metamaterials to structural transitions. *Appl. Mech. Rev.*, 69(5), 2017.
- [92] M. Pishvar and R. L. Harne. Foundations for soft, smart matter by active mechanical metamaterials. *Adv. Science*, 7(18):2001384, 2020.
- [93] X. Xia, A. Afshar, H. Yang, C. M. Portela, D. M. Kochmann, C. V. Di Leo, and J. R. Greer. Electrochemically reconfigurable architected materials. *Nature*, 573(7773):205–213, 2019.
- [94] B. Deng, J. R. Raney, K. Bertoldi, and V. Tournat. Nonlinear waves in flexible mechanical metamaterials. *J. Appl. Phys.*, 130(4):040901, 2021.
- [95] B. Deng, J. R. Raney, V. Tournat, and K. Bertoldi. Elastic vector solitons in soft architected materials. *Phys. Rev. Lett.*, 118(20):204102, 2017.
- [96] B. Deng, P. Wang, Q. He, V. Tournat, and K. Bertoldi. Metamaterials with amplitude gaps for elastic solitons. *Nature Communications*, 9(3410), 2018.
- [97] L. Jin, R. Khajehtourian, J. Mueller, A. Rafsanjani, V. Tournat, K. Bertoldi, and D. M. Kochmann. Guided transition waves in multistable mechanical metamaterials. *Proc. Nat. Acad. Sci.*, 117(5):2319–2325, 2020.
- [98] N. Vasios, B. Deng, B. Gorissen, and K. Bertoldi. Universally bistable shells with nonzero Gaussian curvature for two-way transition waves. *Nature Commun.*, 12(1):1–9, 2021.
- [99] J. R. Raney, N. Nadkarni, C. Daraio, D. M. Kochmann, J. A. Lewis, and K. Bertoldi. Stable propagation of mechanical signals in soft media using stored elastic energy. *Proc. Nat. Acad. Sci.*, 113(35):9722–9727, 2016.
- [100] H. Yasuda, C. Chong, E. G. Charalampidis, P. G. Kevrekidis, and J. Yang. Formation of rarefaction waves in origami-based metamaterials. *Phys. Rev. E*, 93(4):043004, 2016.

- [101] A. Zareei, B. Deng, and K. Bertoldi. Harnessing transition waves to realize deployable structures. *PNAS*, 117(8):4015–4020, 2020.
- [102] T. Chen, O. R. Bilal, K. Shea, and C. Daraio. Harnessing bistability for directional propulsion of soft, untethered robots. *PNAS*, 115(22):5698–5702, 2018.
- [103] B. Deng, L. Chen, D. Wei, V. Tournat, and K. Bertoldi. Pulse-driven robot: Motion via solitary waves. *Sci. Adv.*, 6(18):eaaz1166, 2020.
- [104] H. Fang, K. W. Wang, and S. Li. Asymmetric energy barrier and mechanical diode effect from folding multi-stable stacked-origami. *Extreme Mech. Lett.*, 17:7–15, 2017.
- [105] L. S. Novelino, Q. Ze, S. Wu, G. H. Paulino, and R. Zhao. Untethered control of functional origami microrobots with distributed actuation. *PNAS*, 117(39):24096–24101, 2020.
- [106] D. J. Preston, H. J. Jiang, V. Sanchez, P. Rothmund, J. Rawson, M. P. Nemitz, W.-K. Lee, Z. Suo, C. J. Walsh, and G. M. Whitesides. A soft ring oscillator. *Sci. Robot.*, 4(31), 2019.
- [107] A. Rafsanjani, Y. Zhang, B. Liu, S. M. Rubinstein, and K. Bertoldi. Kirigami skins make a simple soft actuator crawl. *Sci. Robot.*, 3(15), 2018.
- [108] F. Li, P. Anzel, J. Yang, P.G. Kevrekidis, and C. Daraio. Granular acoustic switches and logic elements. *Nature Communications*, 5:5311, 2014.
- [109] A. Rafsanjani, L. Jin, B. Deng, and K. Bertoldi. Propagation of pop ups in kirigami shells. *PNAS*, 116(17):8200–8205, 2019.
- [110] H. Yasuda, L. M. Korpas, and J. R. Raney. Transition waves and formation of domain walls in multistable mechanical metamaterials. *Phys. Rev. Appl.*, 13(5):054067, 2020.
- [111] H. Duran, J. Cuevas-Maraver, P. G. Kevrekidis, and A. Vainchtein. Discrete breathers in a mechanical metamaterial, 2022. In preparation.
- [112] B. Deng, V. Tournat, P. Wang, and K. Bertoldi. Anomalous collisions of elastic vector solitons in mechanical metamaterials. *Phys. Rev. Lett.*, 122(4):044101, 2019.
- [113] P. G. Kevrekidis, J. Cuevas-Maraver, and D. E. Pelinovsky. Energy criterion for the spectral stability of discrete breathers. *Phys. Rev. Lett.*, 117:094101, 2016.

- [114] M. Beck, J. Knobloch, D. J. B. Lloyd, B. Sandstede, and T. Wagenknecht. Snakes, ladders, and isolas of localized patterns. *SIAM J. Math. Anal.*, 41(3):936–972, 2009.
- [115] C. Chong, R. Carretero-González, B. A. Malomed, and P. G. Kevrekidis. Multistable solitons in higher-dimensional cubic-quintic nonlinear Schrödinger lattices. *Physica D*, 238:126–136, 2009.
- [116] C. Taylor and J. H. P. Dawes. Snaking and isolas of localised states in bistable discrete lattices. *Phys. Lett. A*, 375(1):14–22, 2010.
- [117] J. L. Marín and S. Aubry. Breathers in nonlinear lattices: numerical calculation from the anticontinuous limit. *Nonlinearity*, 9(6):1501, 1996.
- [118] P. Poggi and S. Ruffo. Exact solutions in the FPU oscillator chain. *Physica D*, 103(1):251–272, 1997.
- [119] Yu. A. Kosevich. Nonlinear envelope-function equation and strongly localized vibrational modes in anharmonic lattices. *Phys. Rev. B*, 47(6):3138, 1993.
- [120] R. S. MacKay and S. Aubry. Proof of existence of breathers for time-reversible or Hamiltonian networks of weakly coupled oscillators. *Nonlinearity*, 7(6):1623, 1994.
- [121] R. Chaunsali, H. Xu, J. Yang, P. G. Kevrekidis, and G. Theocharis. Stability of topological edge states under strong nonlinear effects. *Phys. Rev. B*, 103:024106, 2021.
- [122] A.M. Morgante, M. Johansson, S. Aubry, and G.A. Kopidakis. Breather-phonon resonances in finite-size lattices: phantom breathers. *J. Phys. A*, 35:4999–5021, 2002.
- [123] J. P. Boyd. A numerical calculation of a weakly non-local solitary wave: the ϕ^4 breather. *Nonlinearity*, 3(1):177, 1990.
- [124] H. Segur and M.D. Kruskal. Nonexistence of small-amplitude breather solutions in ϕ^4 theory. *Phys. Rev. Lett.*, 58:747–750, 1987.
- [125] X. Guo. *Nonlinear architected metasurfaces for acoustic wave scattering manipulation*. PhD thesis, Le Mans, 2018.
- [126] B. Sánchez-Rey, G. James, J. Cuevas, and J. F. R. Archilla. Bright and dark breathers in Fermi-Pasta-Ulam lattices. *Phys. Rev. B*, 70(1):014301, 2004.

- [127] R. A. Vicencio and M. Johansson. Discrete soliton mobility in two-dimensional waveguide arrays with saturable nonlinearity. *Phys. Rev. E*, 73:046602, Apr 2006.
- [128] A. Demiquel, G. Theocharis, V. Achilleos, and V. Tournat. Nonlinear Schrödinger equations in Lego metamaterial, 2022. In preparation.
- [129] V. I. Arnold. *Mathematical methods of classical mechanics*. Springer-Verlag, New York, 1978.
- [130] R. L. Pego and M. I. Weinstein. Eigenvalues, and instabilities of solitary waves. *Phil. Trans. Royal Soc. London A*, 340(1656):47–94, 1992.